Phonon Scattering and Confinement in Crystalline Films

Submitted in partial fulfillment of the requirements for the degree of

Doctor of Philosophy

in

Mechanical Engineering.

Kevin D. Parrish

B.S., Chemical and Biomolecular Engineering, Johns Hopkins University, MD, USA

M.S., Mechanical Engineering, Carnegie Mellon University, PA, USA

Carnegie Institute of Technology

Carnegie Mellon University

Pittsburgh, PA 15213

August 2017

Abstract

Phonon Scattering and Confinement in Crystalline Films
by
Kevin D. Parrish

Co-Chairs: Professor Alan J. H. McGaughey, Associate Professor Jonathan A. Malen

The operating temperature of energy conversion and electronic devices affects their efficiency and efficacy. In many devices, however, the reference values of the thermal properties of the materials used are no longer applicable due to processing techniques performed. This leads to challenges in thermal management and thermal engineering that demand accurate predictive tools and high fidelity measurements. The thermal conductivity of strained, nanostructured, and ultra-thin dielectrics are predicted computationally using solutions to the Boltzmann transport equation. Experimental measurements of thermal diffusivity are performed using transient grating spectroscopy.

The thermal conductivities of argon, modeled using the Lennard-Jones potential, and silicon, modeled using density functional theory, are predicted under compressive and tensile strain from lattice dynamics calculations. The thermal conductivity of silicon is found to be invariant with compression, a result that is in disagreement with previous computational efforts. This difference is attributed to the more accurate force constants calculated from density functional theory. The invariance is found to be a result of competing effects of increased phonon group velocities and decreased phonon lifetimes, demonstrating how the anharmonic contribution of the atomic potential can scale differently than the harmonic contribution.

Using three Monte Carlo techniques, the phonon-boundary scattering and the subsequent thermal conductivity reduction are predicted for nanoporous silicon thin films. The Monte Carlo techniques used are free path sampling, isotropic ray-tracing, and a new technique, modal ray-tracing. The thermal conductivity predictions from all three techniques

are observed to be comparable to previous experimental measurements on nanoporous silicon films. The phonon mean free paths predicted from isotropic ray-tracing, however, are unphysical as compared to those predicted by free path sampling. Removing the isotropic assumption, leading to the formulation of modal ray-tracing, corrects the mean free path distribution. The effect of phonon line-of-sight is investigated in nanoporous silicon films using free path sampling. When the line-of-sight is cut off there is a distinct change in thermal conductivity versus porosity. By analyzing the free paths of an obstructed phonon mode, it is concluded that the trend change is due to a hard upper limit on the free paths that can exist due to the nanopore geometry in the material.

The transient grating technique is an optical contact-less laser based experiment for measuring the in-plane thermal diffusivity of thin films and membranes. The theory of operation and physical setup of a transient grating experiment is detailed. The procedure for extracting the thermal diffusivity from the raw experimental signal is improved upon by removing arbitrary user choice in the fitting parameters used and constructing a parameterless error minimizing procedure.

The thermal conductivity of ultra-thin argon films modeled with the Lennard-Jones potential is calculated from both the Monte Carlo free path sampling technique and from explicit reduced dimensionality lattice dynamics calculations. In these ultra-thin films, the phonon properties are altered in more than a perturbative manner, referred to as the confinement regime. The free path sampling technique, which is a perturbative method, is compared to a reduced dimensionality lattice dynamics calculation where the entire film thickness is taken as the unit cell. Divergence in thermal conductivity magnitude and trend is found at few unit cell thick argon films. Although the phonon group velocities and lifetimes are affected, it is found that alterations to the phonon density of states are the primary cause of the deviation in thermal conductivity in the confinement regime.

Acknowledgements

"Labor Omnia Vincit" - Virgil

I would like to thank the committee members, Prof. Alan McGaughey (Co-chair), Prof. Jonathan Malen (Co-chair), Prof. Gian Piazza, and Prof. Sangyeop Lee for agreeing to serve on my committee and for their time and advice. Specifically, I would like to thank my advisors, Alan and Jon. Without their guidance and support I would not have the opportunity nor skills to pursue science.

I give thanks to my funding sources for their financial aid. I thank my family for their enduring love and my friends for their trust and care. I want to thank the scientists who have come before me for their sacrifice in the pursuit of truth. Finally, I thank my wife, Michelle, for her everlasting love and her patience during my doctoral pursuit.

This work was supported by the CMU Graduate Student Association conference travel fund, the Milton Shaw travel award, the CIT Bertucci fellowship 2016, the CIT Bushnell fellowship 2017, the AFOSR award FA9550101009, and NSF awards DMR-1507325 and ENG-1403447.

Contents

List of Figures

List of Tables

Nomenclature

Abbreviations

ESPRESSO opEn-Source Package for Research in Electronic Structure, Simulation, and Optimization.

Ag NPs Silver nanoparticles.

ALD Anharmonic lattice dynamics.

CQD Colloidal quantum dot.

DNTT dinaphtho[2,3-b:2′,3′-f]thieno[3,2-b]thiophene.

EOM Electro-optic modulator.

GK Green-Kubo.

HLD Harmonic lattice dynamics.

ISBS Impulsive Stimulated Brillouin Scattering.

ISTS Impulsive Strained Thermal Scattering.

LAMMPS Large-scale Atomic/Molecular Massively Parallel Simulator.

LD Lattice dynamics.

LJ Lennard-Jones.

MD Molecular dynamics.

MK Monkhorst-Pack.

MSE Mean squared error.

PEDOT poly(3,4-ethylenedioxythiophene).

PSS poly(styrenesulphonate).

TG Transient grating spectroscopy.

ZT Thermoelectric figure of merit.

Subscripts

α, β, γ Cartesian direction index.

j Basis atom index.

l Unit cell index.

Superscripts

$*$ Complex conjugate.

Variables

α Thermal diffusivity.

$\bar{\Lambda}_{\mathrm{bdy}}$ Averaged boundary mean free path.

δ Dirac delta function.

ϵ_{LJ} Lennard-Jones energy scale.

η Inverse penetration depth.

exp Exponential function.

$\hbar$ Reduced Planck constant.

Λ Phonon mean free path.

λ_{air} Wavelength in air.

Λ_{bdy} Boundary mean free path.

Λ_{pp} Phonon-phonon mean free path.

χ Third-order force constant matrix.

$\mathbf{\Phi}$ Second-order force constant matrix.

$\mathbf{\Pi}$ First-order force constant vector.

$\mathbf{\Psi}$ Third-order coupling strength.

$\widetilde{\mathbf{e}}$ Spatial-phase factored eigenvector.

$\mathbf{D}$ Dynamical matrix.

$\mathbf{e}$ Eigenvector.

$\mathbf{F}$ Force vector.

$\mathbf{G}$ Reciprocal lattice vector.

$\mathbf{q}$ Wavevector.

$\mathbf{r}$ Atomic position.

$\mathbf{U}$ Displacement vector.

$\mathbf{u}$ Atomic displacement vector.

$\mathbf{v}_{\text{g}}$ Phonon group velocity vector.

$\mathcal{K}$ Imaginary refractive index.

$\mathcal{N}$ Real refractive index.

$\mathcal{T}$ Transmission ratio.

ν Polarization.

ω Frequency.

ϕ_{p} Phase of probe beam.

ϕ_{r} Phase of reference beam.

π Mathematical constant pi.

σ Stress.

σ_{LJ} Lennard-Jones length scale.

τ Phonon relaxation time or phonon lifetime.

θ Zenith angle.

θ_{air} Angle in air.

$\underline{\mathcal{N}}$ Complex refractive index.

ε Strain.

A Amplitude.

a Lattice constant.

$a_{\circ}$ Zero-pressure lattice constant.

B Reciprocal volume.

c_{ph} Phonon heat capacity.

$E_{\mathrm{p+1}}$ First-order diffracted probe beam electric field.

$E_{\mathrm{r+0}}$ Zeroth-order reference beam electric field.

$E_{0\mathrm{p}}$ Base amplitude of first-order diffracted probe beam electric field.

$E_{0\mathrm{r}}$ Base amplitude of zeroth-order reference beam electric field.

f Occupation.

f' Deviation from equilibrium occupation.

f_{eq} Equilibrium occupation.

G Thermal conductance.

H Number of unit cells in the cross-plane direction.

I Intensity.

k_{GK} Thermal conductivity from Green-Kubo calculations.

k_{LD} Thermal conductivity from lattice dynamics calculations.

k_{p} Wavenumber of probe and reference beams.

L Length.

l Integer or diffraction grating spacing.

m Mass.

N Number of unit cells.

n Number of atoms in a basis.

N_{MK} Number of Monkhorst-Pack grid points in one dimension.

q_{D} Transient grating wavenumber.

S Substitution variable.

T Temperature.

t Time or thickness.

t_{r} Attenuation factor of reference beam.

V Crystal energy.

$V_{\circ}$ Base crystal energy.

x, y, z Cartesian directions.

Introduction

1.1 Motivation

As the characteristic length scales of electronic devices approach those of the fundamental carriers, the transport properties of the constituent materials are no longer intrinsic. Instead, the geometry of the device dictates the transport properties. In the case of the ubiquitous semiconductor silicon, when the characteristic length scales approach $\sim 1\,\mu$m the thermal conductivity reduces. This is due to quantized lattice vibrations, or phonons, undergoing boundary-scattering. Furthermore under extreme reduction in characteristic length scales (e.g., silicon $<$ 50 nm), such as that seen in modern semiconductor manufacturing, the lattice vibrations become fundamentally modified and cannot be treated as bulk phonons with perturbed scattering. In these devices, the thermal transport properties and the resulting operating temperature affect the lifetime, efficiency, and efficacy, motivating the characterization and prediction of thermal transport.

In such devices, the thermal properties cannot be obtained from reference values. This creates design challenges as the changes in thermal properties from the geometry will have consequences to the performance of the device. Advances in computational power have allowed us to solve the fundamental equations governing phonon transport. We can predict phonon transport properties for bulk systems using lattice dynamics calculations. Various Monte Carlo techniques allow for prediction of phonon-boundary scattering in nanostructured materials. Moreover, when it is computationally feasible, explicit calculations of the dynamics of few nanometer sized materials can be calculated. With advanced optical laser-based techniques, we can experimentally measure the thermal properties of thin films

of novel materials and nanostructured systems in both cross-plane and in-plane directions.

1.2 Objectives

1.2.1 Overview

Thermal conductivity, k, is the property of a material that describes the thermal energy flux due to a temperature gradient. It is defined as the proportionality constant in Fourier's law, $Q = -k\Delta T$, where Q is the heat flux and ΔT is the one-dimensional temperature gradient[1, 2]. In most macroscopic conditions, the thermal conductivity is an intrinsic property and can be easily obtained from references[3]. This thermal conductivity can subsequently be used in the heat diffusion equation to model specific geometries. When the fundamental carriers of heat are modified, however, the reference thermal conductivity value can be incorrect and the heat diffusion equation is invalidated. In crystalline insulators and semiconductors, these carriers are lattice vibrations that are quantized into "phonons." When the phonon transport properties are changed, the thermal conductivity can be considered an extrinsic property and it depends on the specific material conditions and form.

The objective of this thesis is to predict and quantify the thermal conductivity when external loading or geometry modify the underlying phonon thermal carriers. We calculated phonon properties with lattice dynamics techniques to predict the thermal conductivity of strained dielectrics. Moreover, we compare Monte Carlo techniques in their ability to calculate the thermal conductivity of nanostructured films. To experimentally measure the thermal conductivity of semi-transparent materials, we build and describe transient grating spectroscopy. Further, we theoretically examine the breakdown of the boundary-scattering techniques to describe thermal transport of ultra-thin films by using reduced

dimensionality lattice dynamics calculations.

1.2.2 Effects of Strain on Phonons

To simplify modeling efforts, the assumption that a material or device is at zero strain is often made. Under realistic conditions in many systems, however, zero strain is not the case. For example, the extreme pressures in the Earth's core ($\sim$ 300 GPa) can increase the thermal conductivity of the constituent materials (e.g., iron) by a factor of three[4]. Strain can also be induced by epitaxial interfaces[5, 6, 7], mechanical loading, and the thermal expansion that results from an imposed temperature gradient or Joule heating. Strain can be used to engineer the transport properties of electrons and phonons[8], to tune the thermal conductance of interfaces[9, 10], and can modify thermal conductivity in nanostructures such as nanowires and one- and two-dimensional materials[11, 12, 13, 14, 15]. We quantify the thermal conductivity change in argon modeled with Lennard-Jones and silicon modeled with density functional theory when strained in compression and tension. The effects of strain on the phonon transport properties and their impact on thermal conductivity are investigated.

1.2.3 Phonon-Boundary Scattering

The classical effect of porosity on thermal conductivity is well described. Using the heat diffusion equation, the reduction ratio can be solved for computationally. When the feature sizes of the porous material are on the order of the fundamental energy carriers' mean free paths, boundary scattering of these carriers results in a reduction of the intrinsic thermal conductivity in addition to the continuum effect. A porous material that exhibits both thermal conductivity reduction mechanisms is a silicon film tens to hundreds of nanometers thick that has a periodic two-dimensional array of pores tens to hundreds of nanometers

in radii that span the film thickness[16, 17, 18, 19, 20, 21, 22, 23, 24, 25, 26, 27, 28, 29, 29, 30, 31, 32, 33]. These nanoporous films scatter the thermally relevant phonons, reducing the thermal conductivity past the continuum effect. The suppression of the phonon thermal conductivity makes nanoporous silicon films attractive as a possible thermoelectric material[17, 34]. We calculate the suppression of the phonon mean free path due to phonon-boundary scattering from three Monte Carlo methods and compare to previous experiments.

1.2.4 Transient Grating

When materials are delicate or very small contactless optical-laser based techniques can be used to measure the thermal properties. These work by using a "pump" laser to heat the sample and a "probe" laser to measure the temperature response. Two popular concentric beam techniques, frequency domain thermoreflectance and time domain thermoreflectance, can be used to measure the cross-plane thermal conductivity of a layered material system. They are insensitive to the in-plane thermal transport, however, and require a metallic transducer layer than can change the dynamics of thin materials. Transient grating spectroscopy operates by interfering two laser beams to heat the sample with a one-dimensional periodic temperature gradient. The decay of the temperature gradient can be recorded without the use of a transducer by measuring the diffraction of the probe beam off the heated pattern, resulting in the signal that is sensitive to the in-plane transport. We describe the transient grating setup and introduce a parameterless data extraction method that eliminates previous guess-based approaches.

1.2.5 Confinement

When the geometrical feature sizes approach that of the thermally relevant phonons the transport properties cannot be corrected in a perturbative manner. At these length scales, termed the confinement regime, the phonon modes' eigenvectors, frequencies, and density of states are modified in addition to the transport properties. This invalidates such Monte Carlo techniques considered in Sec. 1.2.3. The exact manner by which the phonon mode properties change has not been previously described. To examine this crossover between a ballistic boundary-scattering regime and the confinement regime we consider the simplest case of a membrane. We use reduced dimensionality lattice dynamics where we redefine our unit cell to be entire thickness of the thin film, eliminating the third-dimension of wavevector and reducing our Brillouin zone to two-dimensions. This allows us to examine the transport properties predicted from the Monte Carlo free path sampling technique to the exact solution of reduced dimensionality lattice dynamics.

1.3 Methods

Computationally, we begin with harmonic and anharmonic lattice dynamics. Harmonic lattice dynamics allows us to consider the dynamics of plane-waves in a infinite crystal by treating it as a mass-spring system. From this we can solve for the base properties of the waves and this defines our set of phonons. Using these base properties we obtain the transport phonon properties of heat capacity and group velocity that are relevant to thermal conductivity. To determine our final transport property necessary for thermal conductivity calculations, the phonon lifetime, we perform anharmonic lattice dynamics. By use of perturbation theory, anharmonic lattice dynamics predicts the phonon-phonon scattering rate from three-phonon scattering events. Both of these lattice dynamics tech-

niques require that we obtain force constants of atomic displacements in our crystal. We can describe the atomic interaction in crystals from empirical potentials or by *ab initio* techniques such as density functional theory. Empirical potentials have the advantage of simplicity and speed of computation. The *ab initio* calculations have the advantage of accuracy that allows predictive capability. Both types of atomistic modeling are used in this work.

To account for phonon-boundary scattering, we employ a variety of Monte Carlo techniques. These modify or supplement the bulk phonon lifetimes to account for the additional scattering center. We consider three techniques: free path sampling, isotropic ray-tracing, and modal ray-tracing. All three function by treating phonons as point particles that randomly sample the geometry to quantify the reduction in lifetime due to boundary scattering. They differ, however, in what assumptions they make in their calculations and also in computational implementation. These differences have important implications in the physics they can capture as well as the computational complexity and cost.

1.4 Overview

The methodology and theory are described in Chapter 2. The basic formulation of a phonon through harmonic lattice dynamics is discussed, and the associated phonon transport properties that can be calculated from them. The anharmonic lattice dynamics formulation is described as well as the properties that influence its solution. The equation of thermal conductivity derived from the Boltzmann transport equation under the relaxation time approximation is detailed. The implementation of the Monte Carlo methods, free path sampling, isotropic ray-tracing, and modal ray-tracing, are all discussed. Their approximations and computational details are considered.

In Chapter 3, the thermal conductivity of strained Lennard-Jones argon and density

functional theory modeled silicon is predicted. The phonon transport properties and atomic potential well are all examined to understand from a fundamental level the changes in thermal conductivity.

In Chapter 4, thermal transport in nanoporous silicon is modeled using Monte Carlo techniques. The techniques are compared in terms of computational efficiency and accuracy as compared to previous experiments. A structure in which line-of-sight is controlled is investigated using free path sampling.

In Chapter 5, the theory of operation and experimental build are detailed. The experiment is benchmarked on a water solution and a parameterless fitting procedure is introduced.

In Chapter 6, thermal conductivity predictions are made on ultra-thin Lennard-Jones argon membranes. The predictions from free path sampling and dimensionally reduced lattice dynamics are compared based on thermal conductivity and phonon properties.

In Chapter 7, the thermal conductivity of organic and inorganic colloidal quantum dots for lasing applications and organic semiconductor with interdispersed silver nanoparticles are measured using frequency domain thermoreflectance.

The work of this thesis is summarized in Chapter 8 and future directions for investigation are prescribed.

Theory and Methods

2.1 Introduction

We describe and derive the theory and methods employed in this thesis. First, we will describe harmonic lattice dynamics (HLD) and anharmonic lattice dynamics (ALD), the basis for calculating the bulk phonon properties used in the computational work. Then, the formulation of phonon transport through kinetic theory is examined. Finally, we outline the three Monte Carlo techniques used to calculate the phonon boundary-scattering effects in nanostructured geometries.

2.2 Lattice Dynamics Calculations

2.2.1 Harmonic Lattice Dynamics Formulation

The HLD technique mathematically defines the most basic concept of a "phonon." To formulate this technique some assumptions about our system must be taken. First, the structure of the solid is considered. Only a solid that is a crystal and is infinite in extent is examined, where a crystal is a fixed set of atoms that are located relative to a point on a Bravais lattice. Also, it is assumed that this crystal is stable, i.e., the atoms' equilibrium positions do not evolve over time, or at the very least are meta-stable over the relevant time scale of the phonon carriers. Next, some approximations as to the motion of the atoms are made. The atoms can be approximated as point masses and also their motion can be decoupled from that of the electrons through the Born-Oppenheimer approximation. The ansatz that the atoms vibrate sinusoidally in space and time is then taken. This is

a consequence of considering the interatomic forces as being strictly linear with atomic displacement, as discussed later.

The crystal energy, V, is defined as

$$\begin{aligned} V =& V_\circ + \sum_{\alpha}^{3}\sum_{j,l}^{n,N} \Pi_\alpha \begin{pmatrix} j \\ l \end{pmatrix} u_\alpha(j,l) + \sum_{\alpha,\beta}^{3,3}\sum_{j,l}^{n,N}\sum_{j',l'}^{n,N} \frac{1}{2!}\Phi_{\alpha,\beta} \begin{pmatrix} jj' \\ ll' \end{pmatrix} u_\alpha(j,l)u_\beta(j',l') \\ &+ \sum_{\alpha,\beta,\gamma}^{3,3,3}\sum_{j,l}^{n,N}\sum_{j',l'}^{n,N}\sum_{j'',l''}^{n,N} \frac{1}{3!}\chi_{\alpha,\beta,\gamma} \begin{pmatrix} jj'j'' \\ ll'l'' \end{pmatrix} u_\alpha(j,l)u_\beta(j',l')u_\gamma(j''l'') + \ldots, \end{aligned} \tag{2.1}$$

where, α, β, γ are the Cartesian directions, n is the number of atoms in a unit cell and j is the corresponding basis atom index, N is the number of unit cells and l is the corresponding unit cell index, $\mathbf{u}$ is the atomic displacement vector from equilibrium, $V_\circ$ is the base crystal potential energy, Π is the first-order force constant associated with the displacement of one atom, $\mathbf{\Phi}$ is the second-order (i.e., harmonic) force constant associated with the displacements of two atoms, and χ is the third-order force constant associated with the displacements of three atoms. Here only the force constants up to third-order are listed for brevity, although there is an infinite set of force constants with increasing order. Newton's second law is[35]

$$m\mathbf{a} = \mathbf{F}, \tag{2.2}$$

where m is the mass of an object, $\mathbf{a}$ is the acceleration vector of an object and $\mathbf{F}$ is the force vector acting upon it. The equation of motion for a specific atom from Newton's second law in our crystal is

$$m_j \frac{d^2\mathbf{u}(j,l,t)}{dt^2} = \mathbf{F}(j,l,t), \tag{2.3}$$

where t is time and $\mathbf{F}(j,l,t)$ is the instantaneous force on a specific atom at an instant in

time t. This force from Eq. (2.1) is

$$\begin{aligned}\mathbf{F}(j,l,t) &= -\frac{\partial V}{\partial u_\alpha(j,l,t)} \\ &= \sum_{\alpha}^{3}\sum_{j,l}^{n,N}\Pi_\alpha\begin{pmatrix} j \\ l\end{pmatrix} + \sum_{\alpha,\beta}^{3,3}\sum_{j,l}^{n,N}\sum_{j',l'}^{n,N}\frac{1}{2!}\Phi_{\alpha,\beta}\begin{pmatrix} jj' \\ ll'\end{pmatrix} u_\beta(j',l') \\ &+ \sum_{\alpha,\beta,\gamma}^{3,3,3}\sum_{j,l}^{n,N}\sum_{j',l'}^{n,N}\sum_{j'',l''}^{n,N}\frac{1}{3!}\chi_{\alpha,\beta,\gamma}\begin{pmatrix} jj'j'' \\ ll'l''\end{pmatrix} u_\beta(j',l')u_\gamma(j''l'') + \dots .\end{aligned} \tag{2.4}$$

Note that the base crystal energy has no bearing on the force and subsequently the dynamics of the atoms in the crystal. Also, if our first-order force constant is finite, a force will be applied to all atoms in the system. This is represented physically by a translation of the crystal. As such, the first-order force constant must be zero.

For HLD any force constant terms higher than second-order are discarded. The force generated by a displacement of an atom in our crystal is linear with a proportionality constant defined by the second-order force constant term. The ansatz is taken that the atoms displace in the form of a traveling wave and therefore are temporally and spatially sinusoidal. The result is the displacement of any atom in our crystal is represented by a superposition of plane-waves,

$$\mathbf{u}(j,l,t) = \sum_{\mathbf{q},\nu}\mathbf{U}(j,\mathbf{q},\nu)\exp\left(i\mathbf{q}\cdot\mathbf{r}(j,l)\right)\exp\left(-i\omega(\mathbf{q},\nu)t\right), \tag{2.5}$$

where, $\mathbf{U}$ is the complex amplitude or displacement vector of the wave, $\mathbf{r}$ is either the mean position of the atom or the origin of the unit cell the atom belongs to (the resulting phase difference in absorbed into $\mathbf{U}$), $\mathbf{q}$ is the wavevector, ν is the polarization, and ω is the frequency.

Eq. (2.5) is substituted into Eq. (2.4),

$$m_j\omega^2\left(\mathbf{q},\nu\right)\mathbf{U}(j,\mathbf{q},\nu)=\sum_{j',l'}^{n,N}\Phi\left(\begin{smallmatrix}jj'\\0l'\end{smallmatrix}\right)\mathbf{U}(j',\mathbf{q},\nu)\exp\left(i\mathbf{q}\cdot[\mathbf{r}(j',l')-\mathbf{r}(j,0)]\right). \tag{2.6}$$

To solve this, n equations representing n displacement vectors are considered. However, the relationship between ω and $\mathbf{q}$ is unknown leaving more unknowns than equations. Adding the constraint that the displacement vector must be normalized satisfies this disparity.

The set of equations formed by Eq. (2.6) can now be rewritten in a vector form,

$$\omega^2\left(\mathbf{q},\nu\right)\mathbf{e}\left(\mathbf{q},\nu\right)=\mathbf{D}(\mathbf{q})\mathbf{e}\left(\mathbf{q},\nu\right), \tag{2.7}$$

forming an eigenvalue problem. Here, $\mathbf{e}$ is the eigenvector and is defined as

$$e\left(\begin{smallmatrix}\mathbf{q}j\\\nu\alpha\end{smallmatrix}\right)=\sqrt{m_j}U_\alpha(j,\mathbf{q},\nu), \tag{2.8}$$

ω^2 is the eigenvalue, and

$$\mathbf{D}_{\alpha,\beta}(j,j',\mathbf{q})=\frac{1}{\sqrt{m_jm_{j'}}}\sum_{l'}^{N}\Phi\left(\begin{smallmatrix}jj'\\0l'\end{smallmatrix}\right)\exp\left(i\mathbf{q}\cdot[\mathbf{r}(j',l')-\mathbf{r}(j,0)]\right) \tag{2.9}$$

is the dynamical matrix for a given $\mathbf{q}$.

The solution of Eq. (2.7) allows us to choose a wavevector, $\mathbf{q}$, and determine the associated frequencies and eigenvectors, thereby defining the basic wave properties of phonons. Finally, it is worth noting a couple of consequences of the nature of the eigensolution. Due to the symmetry of the force constants, the dynamical matrix is Hermitian, which results in the properties that the eigenvalues are real and the eigenvectors are orthogonal. Since the eigenvalues are real, the frequencies must be either real, in the case of a positive eigenvalue, or imaginary, in the case of a negative eigenvalue. It can be seen from Eq. (2.5)

that if the frequency is imaginary, then the exponential associated with the time evolution will become real. This indicates that the position of the atom will displace exponentially away from its equilibrium position at the moment in time that the force constants are calculated. Thus, imaginary frequencies are a sign that the atomic positions are unstable and the calculated dynamics are not valid for periods of time after the force constant evaluation. Also of note is that the orthogonality of the eigensolution results in the eigenvectors also acting as normal modes, i.e., sinusoidal atomic displacements with the same frequency that superimpose without interaction.

From the HLD calculation, phonon transport properties can be calculated. The heat capacity of a phonon mode, c_{ph}, is

$$c_{\mathrm{ph}}\left(\mathbf{q},\nu\right)=\hbar\omega\left(\mathbf{q},\nu\right)\frac{\partial f_{\mathrm{eq}}(\mathbf{q},\omega,T)}{\partial T}B, \tag{2.10}$$

where f_{eq} is the equilibrium phonon occupation, $\hbar$ is the reduced Planck constant, and B is the reciprocal volume in the first Brillouin zone that the phonon mode represents. In a classical system $c_{\mathrm{ph}}=k_{\mathrm{B}}B$, where k_{B} is the Boltzmann constant. If the phonons are treated as quantum particles, however, then the population is governed by Bose-Einstein statistics:

$$f_{\mathrm{eq}}=\frac{1}{\exp\left(\hbar\omega/k_{\mathrm{B}}T\right)-1}, \tag{2.11}$$

where T is the equilibrium temperature of the crystal. It is seen that ω is needed to calculate the occupation of phonons using quantum statistics. The group velocity vector, $\mathbf{v}_{\mathrm{g}}$, for a phonon mode is another transport property that can be calculated using the properties gained by HLD. It is defined as the gradient of the frequency with respect to the wavevector,

$$\mathbf{v}_{\mathrm{g}}=\nabla_{\mathbf{q}}\omega. \tag{2.12}$$

It will be shown that both heat capacity and group velocity are important quantities for thermal transport in Sec. 2.3.

2.2.2 Anharmonic Lattice Dynamics Formulation

In Sec. 2.2.1, it is assumed that the vibrations were the form of plane-waves and subsequently discarded higher-order force constants. In a real crystal this is unphysical. If the crystal only had harmonic force constants then in the limit that two atoms were overlapping, the energy would be finite when in reality the energy should diverge to infinity due to the Pauli exclusion principle. In the limit two atoms were separated by an infinite distance, the energy would diverge to infinity when in reality the energy should be finite.[1] Higher-order terms are needed to correct this discrepancy.

When higher-order terms are introduced the possibility of perfect plane-waves are eliminated. This occurs because the formation of plane-waves is only possible with a purely linear force response with displacement, i.e., strictly harmonic force constants. The superposition of the waves breaks down, so that if a vibration is excited it will inevitably decompose into multiple vibrations, even if no other vibrations exist within the system. This results in coupling of phonon modes. When the phonon modes interact, they scatter against each other. A lifetime, τ, in now introduced to describe the average time a specific vibration will persist until it is destroyed.

In terms of thermal transport, this scattering imposes a finite thermal conductivity on a crystal infinite in extent.[2] With the introduction of scattering, along with the degeneracy of the Brillouin zones, this allows for Umklapp scattering. That is, the ability for a phonon mode to convert to phonon modes that propagate in the opposite direction of the heat

[1] Typically the energy between two atoms that are far apart, i.e., non-interacting, is defined to be zero. This choice, however, has no effect on the dynamics of the system as only the derivative of the energy matters.

[2] Crystals finite in extent will always have a finite thermal conductivity. This results from the boundary scattering of carriers which limits the transport lifetime.

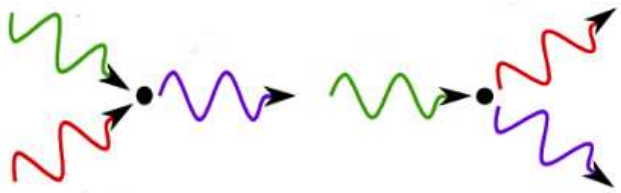

Figure 2.1: Feynman diagrams of annihilation (left) and creation (right) three-phonon processes.

flux, which induces a resistance on the heat flux.

A crystal whose potential has both second-order and third-order force constants results in three-phonon interactions. Fig. 2.1 shows examples of the scattering of three phonons where each color represents a different phonon mode. In Fig. 2.1 an example of the creation of a phonon mode and the annihilation of a phonon mode are shown, but all permutations of the different phonon modes (colors) are possible three-phonon interactions. The lifetime associated from these three-phonon interactions can be calculated with anharmonic lattice dynamics.

Using Fermi's golden rule and the anharmonic Hamiltonian[36, 37, 38], the scattering rate, Γ, due to three-phonon interactions can be written as,

$$\begin{aligned}\Gamma\left(\begin{smallmatrix}\mathbf{q}\\ \nu\end{smallmatrix}\right) = \frac{\pi\hbar}{16N}\sum_{\mathbf{q}',\nu'}^{N,3n}\sum_{\mathbf{q}'',\nu''}^{N,3n}\left|\Psi\left(\begin{smallmatrix}\mathbf{q} & \mathbf{q}' & \mathbf{q}''\\ \nu & \nu' & \nu''\end{smallmatrix}\right)\right|^2 \\ \times\left[f\left(\begin{smallmatrix}\mathbf{q}'\\ \nu'\end{smallmatrix}\right)+f\left(\begin{smallmatrix}\mathbf{q}''\\ \nu''\end{smallmatrix}\right)+1\right]\delta\left(\omega\left(\begin{smallmatrix}\mathbf{q}\\ \nu\end{smallmatrix}\right)-\omega\left(\begin{smallmatrix}\mathbf{q}'\\ \nu'\end{smallmatrix}\right)-\omega\left(\begin{smallmatrix}\mathbf{q}''\\ \nu''\end{smallmatrix}\right)\right) \\ +\left[f\left(\begin{smallmatrix}\mathbf{q}'\\ \nu'\end{smallmatrix}\right)-f\left(\begin{smallmatrix}\mathbf{q}''\\ \nu''\end{smallmatrix}\right)\right]\delta\left(\omega\left(\begin{smallmatrix}\mathbf{q}\\ \nu\end{smallmatrix}\right)+\omega\left(\begin{smallmatrix}\mathbf{q}'\\ \nu'\end{smallmatrix}\right)-\omega\left(\begin{smallmatrix}\mathbf{q}''\\ \nu''\end{smallmatrix}\right)\right) \\ +\left[f\left(\begin{smallmatrix}\mathbf{q}''\\ \nu''\end{smallmatrix}\right)-f\left(\begin{smallmatrix}\mathbf{q}'\\ \nu'\end{smallmatrix}\right)\right]\delta\left(\omega\left(\begin{smallmatrix}\mathbf{q}\\ \nu\end{smallmatrix}\right)-\omega\left(\begin{smallmatrix}\mathbf{q}'\\ \nu'\end{smallmatrix}\right)+\omega\left(\begin{smallmatrix}\mathbf{q}''\\ \nu''\end{smallmatrix}\right)\right)\end{aligned} \tag{2.13}$$

where δ is the Dirac delta function and the third-order coupling strength, Ψ, can be

calculated by

$$\Psi\left(\begin{smallmatrix}\mathbf{q} & \mathbf{q}' & \mathbf{q}''\\ \nu & \nu' & \nu''\end{smallmatrix}\right) = \sum_{\alpha,j}^{3,n}\sum_{\beta,j',l'}^{3,n,N}\sum_{\gamma,j'',l''}^{3,n,N}\delta\left(\mathbf{q}+\mathbf{q}'+\mathbf{q}''\pm\mathbf{G}\right)\times\chi_{\alpha,\beta,\gamma}\left(\begin{smallmatrix}jj'j''\\ ll'l''\end{smallmatrix}\right) \times\frac{\widetilde{e}\left(\begin{smallmatrix}\mathbf{q} & j\\ \nu & \alpha\end{smallmatrix}\right)\widetilde{e}\left(\begin{smallmatrix}\mathbf{q}' & j'\\ \nu' & \beta\end{smallmatrix}\right)\widetilde{e}\left(\begin{smallmatrix}\mathbf{q}'' & j''\\ \nu'' & \gamma\end{smallmatrix}\right)}{\sqrt{m_j\omega\left(\begin{smallmatrix}\mathbf{q}\\ \nu\end{smallmatrix}\right)m_{j'}\omega\left(\begin{smallmatrix}\mathbf{q}'\\ \nu'\end{smallmatrix}\right)m_{j''}\omega\left(\begin{smallmatrix}\mathbf{q}''\\ \nu''\end{smallmatrix}\right)}} \times\exp\left[i\mathbf{q}'\cdot\mathbf{r}\left(\begin{smallmatrix}l'\\ 0\end{smallmatrix}\right)\right]\exp\left[i\mathbf{q}''\cdot\mathbf{r}\left(\begin{smallmatrix}l''\\ 0\end{smallmatrix}\right)\right], \tag{2.14}$$

where $\mathbf{G}$ is the reciprocal lattice vector and the spatial-phase factored eigenvector, $\widetilde{\mathbf{e}}$, is

$$\widetilde{e}\left(\begin{smallmatrix}\mathbf{q} & j\\ \nu & \alpha\end{smallmatrix}\right) = e\left(\begin{smallmatrix}\mathbf{q} & j\\ \nu & \alpha\end{smallmatrix}\right)\exp\left[i\mathbf{q}\cdot\mathbf{r}\left(\begin{smallmatrix}0\\ j\end{smallmatrix}\right)\right]. \tag{2.15}$$

First, in Eq. (2.13) it is noted that frequency is conserved between the inputs and outputs of the scattering event. This occurs because the energy of a phonon mode is $\hbar\omega$ and energy is conserved. Also the population f is considered in the creation and annihilation events. This is because the propensity for a phonon to be annihilated is directly proportional to how many phonons are available. Also the propensity for a phonon to be generated is increased when the phonon population is lower. The scattering rate is directly proportional to the square of the third-order coupling strength, Ψ, which describes how strongly three phonons couple together.

In Eq. (2.14), the phonon wavevector $\mathbf{q}$ is conserved up to a reciprocal lattice vector factor of $\mathbf{G}$. The conservation of the wavevector is sometimes called the conservation of "quasi-momentum" or "crystal-momentum." Physically, the conservation of momentum ensures the crystal remains translationally invariant. It is conserved up to a factor of $\mathbf{G}$ due to the degeneracy of the Brillouin zones, which physically is the aliasing of the vibrations as a result of the discrete positions of the atoms[39, 40]. Next the third-order force constant χ is considered, which is defined as the third-derivative of the crystal energy with respect

to atomic position

$$\chi_{\alpha,\beta,\gamma}\left(\begin{smallmatrix} jj'j'' \\ ll'l'' \end{smallmatrix}\right) = \frac{\partial^3 V}{\partial u_\alpha\left(\begin{smallmatrix} 0 \\ j \end{smallmatrix}\right)\partial u_\beta\left(\begin{smallmatrix} l' \\ j' \end{smallmatrix}\right)\partial u_\gamma\left(\begin{smallmatrix} l'' \\ j'' \end{smallmatrix}\right)}. \tag{2.16}$$

In a purely harmonic oscillator system, this term is zero, but it is finite in a real crystal. Eq. (2.14) also accounts for the eigenvector overlap. This occurs for two reasons: first, eigenvectors cannot interact if they are vibrating in orthogonal directions and second, the eigenvectors interact when they try to displace the same atom. The masses of the atoms involved in the vibration and the phonon frequencies are considered from an inertial standpoint. Finally, the spatial-phase factor overlap is considered.

The scattering rate can be related to the phonon lifetime by

$$\tau = \frac{1}{2\Gamma}. \tag{2.17}$$

This allows us to calculate the lifetime of the phonon vibrations due to phonon-phonon scattering, and it is dependent on the harmonic properties as well as the anharmonic properties. Because the equations are coupled, the computational cost of ALD is much greater than that of HLD. The number of force constants and three-phonon processes to be considered must be reduced through crystal symmetries to make the calculation practical[38].

2.3 Phonon Transport

The propensity for a solid to conduct heat is described by the Fourier law[1],

$$\mathbf{Q} = -\mathbf{k}\nabla T. \tag{2.18}$$

The Fourier law specifies that the heat flux vector, $\mathbf{Q}$, is proportional to the spatial temperature gradient, ∇T, through a proportionality tensor $\mathbf{k}$. This proportionality tensor is called the thermal conductivity. Although the Fourier law is phenomenological in nature, the thermal conductivity tensor can be defined by the fundamental thermal carriers of our material. Here, the contribution of phonons to the thermal conductivity is considered.

The kinetics of phonons can be statistically described through the Boltzmann transport equation (BTE). It is important to note that by using the BTE it is assumed that the phonons are strictly particles and discard any wave-like transport effects (i.e., interference, coherence, etc.). The BTE for a phonon mode of $\mathbf{q}$ and ν is[39, 41, 42]

$$\frac{\partial f(\mathbf{x},\mathbf{q},\nu)}{\partial t} + \mathbf{v}_{\mathrm{g}}(\mathbf{q},\nu)\cdot\nabla T(\mathbf{x})\frac{\partial f(\mathbf{x},\mathbf{q},\nu)}{\partial T(\mathbf{x})} = \left(\frac{\partial f(\mathbf{x},\mathbf{q},\nu)}{\partial t}\right)_{\mathrm{scatter}}, \tag{2.19}$$

where the first term on the left is change in population of a phonon at a point in space $\mathbf{x}$, the second term is the diffusion of phonons due to a spatial temperature gradient, and the term on the right is the change in phonon population due to scattering events. Note that f is the instantaneous population of a phonon mode in space and is not necessarily the equilibrium population. If the crystal is considered to be infinite, free of defects, and other energy carriers, then the scattering events only come from other phonons. By restricting the scattering events to these phonon-phonon interactions, the relaxation-time approximation can be employed,

$$\left(\frac{\partial f}{\partial t}\right)_{\mathrm{p-p}} = \frac{-f'}{\tau}, \tag{2.20}$$

where the term on the left is the change in population due to phonon-phonon scattering events and

$$f = f_{\mathrm{eq}} + f'. \tag{2.21}$$

Here f' is a deviation from the population specified by the Bose-Einstein equilibrium distribution and τ is the phonon relaxation time (i.e., phonon lifetime). Assuming our system to be at steady state and substituting Eq. (2.21) into Eq. (2.19),

$$\mathbf{v}_{\mathrm{g}}(\mathbf{q},\nu)\cdot\nabla T(\mathbf{x})\frac{\partial f(\mathbf{x},\mathbf{q},\nu)}{\partial T(\mathbf{x})}=\frac{-f'}{\tau}. \tag{2.22}$$

The heat flux from phonons, $\mathbf{Q}$, in the system is

$$\mathbf{Q}=\sum_{\nu}\sum_{\mathbf{q}}\hbar\omega(\mathbf{q},\nu)\,\mathbf{v}_{\mathrm{g}}(\mathbf{q},\nu)\,f'(\mathbf{q},\nu)\,B. \tag{2.23}$$

Combining Eq. (2.18) with Eq. (2.23) the Fourier law in terms of phonons becomes

$$\sum_{\nu}\sum_{\mathbf{q}}\hbar\omega(\mathbf{q},\nu)\,\mathbf{v}_{\mathrm{g}}(\mathbf{q},\nu)\,f'(\mathbf{q},\nu)\,B=-\mathbf{k}\nabla T. \tag{2.24}$$

Combining Eq. (2.22) and Eq. (2.24),

$$\sum_{\nu}\sum_{\mathbf{q}}\hbar\omega(\mathbf{q},\nu)\,\mathbf{v}_{\mathrm{g}}(\mathbf{q},\nu)\,\tau\mathbf{v}_{\mathrm{g}}(\mathbf{q},\nu)\cdot\nabla T(\mathbf{x})\frac{\partial f(\mathbf{x},\mathbf{q},\nu)}{\partial T(\mathbf{x})}B=-\mathbf{k}\nabla T. \tag{2.25}$$

Dividing out $\nabla T(\mathbf{x})$ and substituting in our phonon heat capacity, c_{ph},

$$\mathbf{k}=\sum_{\mathbf{q}}\sum_{\nu}c_{\mathrm{ph}}(\mathbf{q},\nu)\,\mathbf{v}_{\mathrm{g}}(\mathbf{q},\nu)\,\mathbf{v}_{\mathrm{g}}(\mathbf{q},\nu)\,\tau(\mathbf{q},\nu), \tag{2.26}$$

our phonon thermal conductivity equation. A phonon transport length scale called a mean free path, Λ, can also be defined as

$$\Lambda(\mathbf{q},\nu)=\tau(\mathbf{q},\nu)\,|\mathbf{v}_{\mathrm{g}}(\mathbf{q},\nu)|. \tag{2.27}$$

Substituting Eq. (2.27) into Eq. (2.26) the phonon thermal conductivity equation in terms of mean free path is

$$\mathbf{k} = \sum_{\mathbf{q}} \sum_{\nu} c_{\mathrm{ph}}\left(\mathbf{q},\nu\right) \mathbf{v}_{\mathrm{g}}\left(\mathbf{q},\nu\right) \mathbf{v}_{\mathrm{g}}\left(\mathbf{q},\nu\right) \frac{\Lambda\left(\mathbf{q},\nu\right)}{\left|\mathbf{v}_{\mathrm{g}}\left(\mathbf{q},\nu\right)\right|}. \tag{2.28}$$

Solving Eq. (2.26) and Eq. (2.28) is the primary computational objective of this thesis. It is these equations that drive the necessity of HLD (Sec. 2.2.1), ALD (Sec. 2.2.2), and phonon-boundary scattering techniques (Sec. 2.4).

2.4 Monte Carlo Calculations

2.4.1 Free Path Sampling

Under a kinetic theory treatment, the phonons are treated as particles that travel inside a material at a velocity and direction based off the group velocity vector and with a length defined from the mean free path. Doing so allows for a direct solution of the Boltzmann transport equation in real space and time[43, 44, 45, 46, 47, 48, 49, 50]. If a system is at a uniform equilibrium temperature and therefore a uniform population, the phonon-phonon scattering events can be decoupled and the time evolution ignored. This allows us to sample the volume uniformly and consider the scattering of each phonon mode without consideration of other phonon modes. In a bulk material the operation is trivial, but in a geometrically confined space the phonons will also scatter against the boundaries. By recording the length of the paths traveled by the phonons the additional scattering from boundaries can be captured. This forms the basis for the free path sampling technique[51].

First, a set of bulk phonon group velocity vectors and mean free paths must be pre-calculated. This can be done through the lattice dynamics techniques discussed in Sec. 2.2

with either empirical or first-principles based force constants. For each phonon mode with intrinsic mean free path $\Lambda_{\text{pp}}(\mathbf{q}, \nu)$, a number of free paths are sampled from a Poisson distribution. Each phonon is started from a random position inside the structure. The phonon is then traced from its origin in the direction of its group velocity vector until it either reaches the end of its free path or it encounters a boundary. If the phonon encounters a boundary, its free path is truncated as the distance from the origin to the boundary, otherwise the free path remains the same. After all the free paths are found, they are averaged to provide the effective mean free path $\Lambda(\mathbf{q}, \nu)$, which contains information from both the intrinsic scattering and the geometry-specific boundary scattering. The thermal conductivity is then calculated from Eq. (2.28) using the new mean free paths.

2.4.2 Isotropic Ray-Tracing

In a material in which the phonons scatter with each other and with the boundary at comparable rates the transport is considered a mix of diffusive and ballistic. When considering ballistic carriers between two reservoirs (i.e., bulk like thermal baths) the Landauer formalism is commonly employed[42]. From this formalism, the ballistic contribution to the conductance of the system can be quantified. The contribution of ballistic phonons can be combined with diffusive phonons through the isotropic ray-tracing technique[52].

The thermal conductance contribution, G, of a ballistic phonon mode in an isotropic system of length L is[42]

$$G = \frac{1}{3} \frac{c_{\text{ph}}}{L} |\mathbf{v}_{\text{g}}| \, \bar{\Lambda}_{\text{bdy}}. \tag{2.29}$$

The thermal conductance of this mode can also be defined from an isotropic Landauer formalism as[42]

$$G = \frac{1}{2} c_{\text{ph}} |\mathbf{v}_{\text{g}}| \int_0^{\pi/2} \mathcal{T}(\theta) \cos\theta \sin\theta d\theta, \tag{2.30}$$

where θ is the zenith angle off the normal of the plane at the beginning of the nanostructure and $\mathcal{T}(\theta)$ is the transmission probability through the nanostructure. From Eqs. (2.29) and (2.30),

$$\bar{\Lambda}_{\text{bdy}} = \frac{3}{2} L \int_0^{\pi/2} \mathcal{T}(\theta) \cos\theta \sin\theta d\theta. \tag{2.31}$$

The initial position of the ray-trace is sampled uniformly across the beginning plane of the nanostructure (i.e., the xy-plane when energy transmission is in the z-direction. The initial azimuthal angle is uniformly sampled from $[0, 2\pi)$ while the zenith angle is integrated from $[0, \pi/2]$ in 90 increments. When the ray-trace encounters a boundary it scatters diffusely in accordance with the Lambert cosine law. The ray-tracing terminates when the phonon either encounters the end of the structure (a transmission event) or when it returns to the beginning of the structure (a reflection event). The ratio of rays encountering the end of the structure to the total number of rays is the transmission ratio, $\mathcal{T}(\theta)$. The transmission ratio is calculated by randomly sampling the initial x-position, y-position, and azimuthal angle. To model an infinite structure, the structure length is increased until $\bar{\Lambda}_{\text{bdy}}$ is converged. Isotropic ray-tracing is equivalent to the Casimir limit[52]. No knowledge of the intrinsic phonon properties is required; it only depends on geometry.

The Matthiessen rule is then used to determine the mean free path of each phonon mode in the nanostructure as[53, 54][3]

$$\frac{1}{\Lambda(\mathbf{q}, \nu)} = \frac{1}{\Lambda_{\text{pp}}(\mathbf{q}, \nu)} + \frac{1}{\bar{\Lambda}_{\text{bdy}}}. \tag{2.32}$$

The Matthiessen rule assumes scattering mechanisms to be independent.

[3]Hori et al.[52] describe in their supplemental information a variation of the isotropic ray-tracing technique by which the mean free path is used to probabilistically scatter the ray-trace and avoid using the Matthiessen rule. There is no justification, however, for including phonon-phonon scattering in the Landauer formalism for ballistic conductance.

2.4.3 Modal Ray-Tracing

It is possible to derive the boundary scattering mean free path per phonon mode by eliminating the isotropic approximation invoked in the Landauer formalism in isotropic ray-tracing. This results in a mode-specific boundary scattering mean free path, Λ_{bdy}, instead of an average over all modes.

The ray-tracing is started by initializing the angle off the initial plane from the group velocity vector of a specific phonon mode. The calculation then traces the ray as it diffusely scatters with boundaries according to the Lambert cosine distribution as with isotropic ray-tracing. A mode-specific transmission ratio, $\mathcal{T}(\mathbf{q}, \nu)$, is then calculated.

As derived in Appendix A, the mode-specific boundary mean free path is

$$\Lambda_{\text{bdy}}(\mathbf{q}, \nu) = \frac{L|\mathbf{v}_g(\mathbf{q}, \nu)|}{v_z(\mathbf{q}, \nu)} \mathcal{T}(\mathbf{q}, \nu). \tag{2.33}$$

The effective mean free path is then found by the Matthiessen rule from

$$\frac{1}{\Lambda(\mathbf{q}, \nu)} = \frac{1}{\Lambda_{\text{pp}}(\mathbf{q}, \nu)} + \frac{1}{\Lambda_{\text{bdy}}(\mathbf{q}, \nu)}. \tag{2.34}$$

To save computational time, only phonon modes that have $v_z > 0$ need to be considered for systems that are symmetrical about the z-direction. Phonon modes with $v_z < 0$ have the same $\Lambda_{\text{bdy}}(\mathbf{q}, \nu)$ as their positive counterpart in the evaluation of Eq. (2.34). The number of modes that must be ray-traced can be further reduced by taking advantage of other symmetries. Phonon modes with $v_z = 0$ make no contribution to the flux in that direction and have a boundary mean free path of zero.

Effects of Strain on Thermal Conductivity of Dielectrics

3.1 Introduction

The values for the thermal conductivity of strained materials are not widely available. Limited measurements and studies of the scaling of thermal conductivity, however, have been performed, but only from either a macroscopic standpoint or a rough analytical analysis. The fundamental changes in how the phonon transport properties are altered under strain has not been investigated in a rigorous manner. Moreover, since the development of first-principles based thermal conductivity predictions, there have not been any studies investigating the strain scaling using accurate quantum chemistry calculations.

Ross et al. presented a comprehensive review of experimental measurements of the thermal conductivity of strained materials, including covalent and semiconducting structures[55]. They concluded that compression increases the thermal conductivity of this class of materials. Picu et al. studied strain effects on a model Lennard-Jones (LJ) crystal using molecular dynamics (MD) simulations for isotropic strains ranging from -0.03 to 0.03, where a negative strain indicates compression[56]. Using the Green-Kubo (GK) MD-based method, they found that the thermal conductivity increased under compression and decreased under tension. They attributed this behavior to changes in "stiffness." Tretiakov and Scandolo explored thermal transport in crystalline argon at high temperatures and pressures using MD simulations, the GK method, and the exponential-6 potential[57]. As the compressive stress increased from 2 to 50 GPa, they found a power-law increase of

thermal conductivity. Bhowmick and Shenoy studied strained, crystalline LJ argon using MD simulations and the GK method, also finding a power-law scaling of thermal conductivity with increasing compressive strain[58]. They predicted the same power-law scaling from Fermi's golden rule (exponent within 5%) based on analytical scalings of the phonon lifetime and sound speed. Goncharov et al. experimentally investigated thermal transport in high-temperature, compressed argon using a transient heating technique[59]. Using a diamond anvil cell, argon was compressed in the stress range of 10 to 50 GPa. They found a power-law dependence of thermal conductivity with increasing compression at a temperature of 300 K. Chernatynskiy and Phillpot explored high-temperature (400 to 1200 K) argon using harmonic and anharmonic lattice dynamics calculations with force constants obtained from density functional theory (DFT) calculations over a compressive stress range of 10 to 50 GPa[60]. Their thermal conductivity predictions fit the power-law functional form proposed by Tretiakov and Scandolo[57]. Li et al. studied thermal transport in strained crystalline Tersoff silicon and diamond using MD simulations and the GK method[11]. They found thermal conductivity to monotonically decrease from compression to tension over a strain range of -0.09 to 0.12 and justified this trend using changes in the phonon group velocities. While these previous studies focused on quantifying how thermal conductivity is altered by strain, modifications to the properties of individual phonon modes due to strain have yet to be explored.

In this work, we apply atomistic calculations to investigate how isotropic strain affects phonon mode properties in bulk systems where electrons make a negligible contribution to thermal conductivity. We first consider an LJ argon crystal as a representative soft system. Thermal transport in LJ argon is well-studied,[56, 58, 61, 62, 63, 64, 65] primarily because it uses a computationally-inexpensive two-body potential. As typical of a soft material, LJ argon has a low zero-strain thermal conductivity [$\mathcal{O}(1)$ W/m-K] that results from con-

ε	-0.06	-0.04	-0.02	-0.01	0.00	0.01	0.02	0.04	0.06
a (Å)	4.996	5.102	5.209	5.262	5.315	5.368	5.421	5.528	5.634
σ(GPa)	-0.97	-0.49	-0.18	-0.08	0.00	0.06	0.11	0.17	0.19
$k_{\mathrm{LD}}(\mathrm{W/m-K})$	6.5	3.8	2.2	1.6	1.2	0.88	0.66	0.33	0.14
$k_{\mathrm{GK}}(\mathrm{W/m-K})$	8.0	4.8	2.5	1.7	1.2	0.88	0.68	0.35	0.19

Table 3.1: Properties of LJ argon under different strains (ε). The lattice constants (a), isotropic stresses (σ), MD-based thermal conductivity (k_{GK}), and LD-based thermal conductivity (k_{LD}) are provided.

tributions from the full spectrum of phonon modes[66]. Molecular dynamics simulations and the GK method are first used to predict thermal conductivity for benchmarking purposes. Phonon properties are then predicted from HLD[54, 67] and ALD[36, 37, 38, 63] calculations, detailed in Secs. 2.2.1 and 2.2.2, and are used to evaluate Eq. (2.26) (Sec. 2.3).

We then consider silicon as a representative stiff material. Stiff materials typically exhibit a high thermal conductivity that is dominated by low-frequency acoustic phonon modes[66, 68]. The phonon properties required to evaluate Eq. (2.26) are predicted from HLD and ALD calculations with force constants obtained from DFT and density functional perturbation theory (DFPT) calculations.

The rest of the paper is organized as follows. In Sec. 3.2, we describe the computational methods and details. The thermal conductivities and phonon mode properties are then presented and discussed for LJ argon (Sec. 3.3.1) and silicon (Sec. 3.3.2). To explain differences in the phonon lifetime trends for these two materials, the potential energy wells experienced by the atoms in each are compared in Sec. 3.3.3. We conclude by summarizing our results in Sec. 3.4.

3.2 Computational Details

3.2.1 Lennard-Jones Argon

Argon is an insulating face-centered cubic crystal that can be modeled by the two-body LJ interatomic potential [40]

$$\phi(r_{ij}) = 4\epsilon_{\mathrm{LJ}} \left[\left(\frac{\sigma_{\mathrm{LJ}}}{r_{ij}} \right)^{12} - \left(\frac{\sigma_{\mathrm{LJ}}}{r_{ij}} \right)^{6} \right], \tag{3.1}$$

where i and j denote a pair of atoms, r_{ij} is the distance between the two atoms, ϵ_{LJ} is the energy scale (1.67×10^{-21} J), and σ_{LJ} is the length scale (3.40×10^{-10} m). Argon has an atomic mass m, of 6.63×10^{-26} kg. All calculations are made at a temperature of 20 K, where the zero pressure lattice constant, $a_{\circ}$, is 5.315 Å[64]. We use a cutoff of $2.5\sigma_{\mathrm{LJ}}$ with a shifted potential well for the MD simulations and the lattice dynamics (LD) calculations. Isotropic strains, ε, of -0.06 to 0.06 are considered, such that the lattice constant, a, is $a_{\circ}(1+\varepsilon)$. The strains, lattice constants, and resulting stresses are provided in Table 3.1.

The primitive one-atom basis is used to perform the HLD and ALD calculations with in-house codes. The phonon wavevector grid is sampled using a Monkhorst-Pack grid of $N_{\mathrm{MK}} \times N_{\mathrm{MK}} \times N_{\mathrm{MK}}$ points. Ten values of N_{MK} are considered ranging from 32 to 50 in increments of two. The phonon frequencies ω are obtained from HLD calculations, which require the second-order force constants[54]. Using the frequencies, we calculate the group velocities using finite differencing of the dynamical matrix. The second-order force constants are calculated up to the potential cutoff of $2.5\sigma_{\mathrm{LJ}}$. Since harmonic plane waves do not interact, HLD calculations do not provide any information about the phonon scattering and lifetimes. The phonon lifetimes are predicted using ALD calculations, which

use the third-order force constants to account for three-phonon interactions[63].[1] The third-order force constants are calculated up to first-nearest-neighbor. The force constants are calculated by displacing selected atoms by $10^{-4}a$ from their equilibrium position in a supercell and finite differencing of the resulting forces.

Using the group velocities and lifetimes, we evaluate thermal conductivity from Eq. (2.26). Because the MD simulations to be used for benchmarking are classical, we use classical occupation statistics in the ALD calculations and the classical harmonic value of heat capacity. The inverse of thermal conductivity is plotted verses $1/N_{\mathrm{MK}}$ and a line is fit to the data, whose extrapolated value at $1/N_{\mathrm{MK}} = 0$ gives the infinite system-size (i.e., bulk) value[63].

Turney et al. observed a difference between GK and ALD predictions of thermal conductivity for LJ argon at zero-strain for temperatures above 40 K, where increasing anharmonicity cannot be captured with ALD. Because strain affects the anharmonicity, we also use the MD-based GK method as a self-consistent check of the thermal conductivities calculated from ALD.

The MD simulations are performed using the open-source LAMMPS package[69]. The time step is 4.28 fs and the cubic simulation cell contains 256 atoms. We did not observe changes in thermal conductivity due to size effects over all strains. At each strain, a temperature rescale is performed for 250,000 timesteps to bring the system temperature to 20 K. The system is then evolved in an *NVE* ensemble (a constant number of atoms, volume, and energy) for 250,000 timesteps. A further 1,000,000 timesteps are run where the heat current vector is recorded every five timesteps. Each strain case is run with ten seeds (randomized initial velocities) and the heat current autocorrelation functions are averaged. The heat current autocorrelation function is the input to the GK method,

[1] Turney et al.[63] also included anharmonic frequency shifts based on third- and fourth-order force constants. At a temperature of 20 K, they found the frequency-normalized root mean-square of the frequency shifts to be less than 3%. As such, we do not consider them here.

which is an equilibrium technique for extracting the thermal conductivity k_{GK} based on the fluctuation-dissipation theorem[70]. There is inevitably noise in the heat current autocorrelation function due to a limited sampling of the phase space from the finite sampling time. To find the converged value of the integral of the heat current autocorrelation function, we applied the first-avalanche method[71]. We found k_{GK} to be converged to within 4% with 10 seeds. This error was estimated by removing one seed and calculating the difference in the predicted thermal conductivity when all ten seeds are used.

3.2.2 Silicon

We consider isotopically pure silicon at a temperature of 300 K. At this temperature, silicon undergoes a phase change from the diamond lattice structure to the β-Sn lattice structure at compressive stresses greater than 12 GPa[72]. To avoid this phase transition, we explored strains between -0.03 and 0.03, as provided in Table 3.2. HLD and ALD calculations using in-house codes are performed to obtain phonon frequencies and lifetimes with force constants obtained from DFPT and DFT calculations[38]. A norm-conserving pseudo-potential in the local density approximation is employed in the plane-wave package QUANTUM ESPRESSO[73]. The total energy is converged to within 1.6 meV for a Monkhorst-Pack electronic wavevector-grid of $6 \times 6 \times 6$ and a plane-wave energy cutoff of 80 Ryd. The harmonic force constants are obtained using DFPT calculations with a Monkhorst-Pack phonon wavevector-grid of $8 \times 8 \times 8$ using the primitive (i.e., two-atom) unit cell. The third-order force constants are obtained using finite differences of DFT forces on a 64-atom supercell with a cutoff of third-nearest-neighbor. The forces are obtained by applying displacements of $0.006a$ to selected atoms. The translational invariance constraint (i.e., the acoustic sum rule) for the second- and third-order force constants is enforced using the Lagrangian approach discussed by Lindsay et al.[74]. For the HLD and ALD calcula-

ε	-0.03	-0.025	-0.02	-0.015	-0.01	-0.005	0.0	0.005	0.01	0.015	0.02	0.025	0.03
a (Å)	5.241	5.268	5.295	5.322	5.349	5.376	5.403	5.430	5.457	5.484	5.511	5.538	5.565
σ(GPa)	-10	-8.4	-6.5	-4.7	-3.0	-1.5	0.0	1.4	2.7	3.8	5.0	6.0	7.0
k_{LD}(W/m $-$ K)	147	148	154	149	152	150	151	150	151	150	145	140	137

Table 3.2: Properties of first-principles silicon under different strains (ε). The lattice constants (a), isotropic stresses (σ), and LD-based thermal conductivity (k_{LD}) are provided.

tions, the primitive basis and a $20 \times 20 \times 20$ sampling of the phonon wavevector-grid are used.

We are studying silicon at a temperature of 300 K, which is less than half of its Debye temperature of 625 K[40]. Quantum effects on the heat capacity are important and are included using Bose-Einstein statistics. The thermal conductivity of unstrained silicon calculated using lifetimes from an iterative solution to the Boltzmann transport equation[37] is 151 W/m-K and is converged to within 2% for the above choice of parameters. The experimental value for isotopically enriched silicon is 153 ± 5 W/m-K[75]. This 2% difference is a large improvement over empirical potential-based predictions of thermal conductivity, which can differ from the experimental value by as much as a factor of six at a temperature of 300 K[76]. For the analysis to follow in Section 3.3.2, the lifetimes obtained from the relaxation time approximation will be used because the iterative lifetimes have larger noise that makes direct comparison across strains unfeasible. The relaxation time approximation lifetimes lead to a thermal conductivity prediction of 147 W/m-K, such that we do not believe that this choice will affect our conclusions.

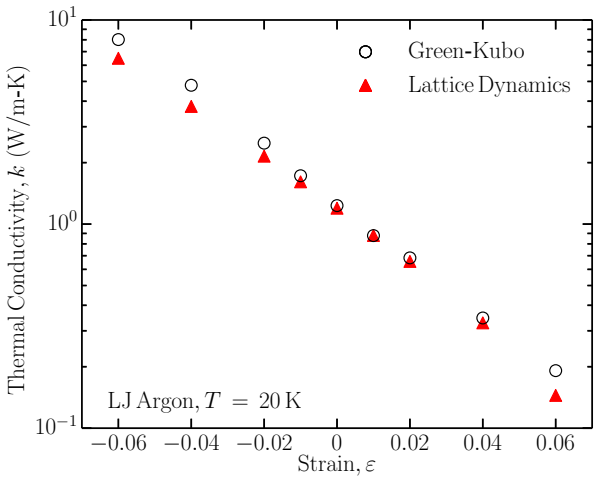

Figure 3.1: Comparison of LJ argon thermal conductivities predicted from MD and LD.

3.3 Results

3.3.1 Lennard-Jones Argon

3.3.1.1 Thermal Conductivity

The strain-dependence of thermal conductivity for LJ argon predicted from MD simulations and LD calculations is presented in Table 3.1 and is plotted in Fig. 3.1. The thermal conductivities span two orders of magnitude. Because the MD-based GK method includes all anharmonic effects (compared to ALD, where we only include up to third-order phonon scattering effects), k_{GK} is taken as the benchmark. The two sets of thermal conductivity data follow the same trend: an exponential decrease when moving from compression to tension (as evidenced by a straight line on the semilog plot). This trend for LJ argon at 20 K was also observed by Bhowmick and Shenoy using the GK method and by Fermi's golden rule-based analytical scalings[58]. The difference between k_{LD} and k_{GK} is less than 25% for all strains considered.

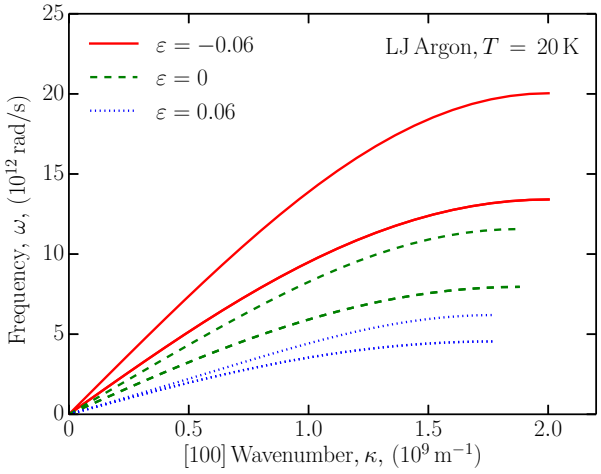

Figure 3.2: [100] strain-dependent phonon dispersion for LJ argon.

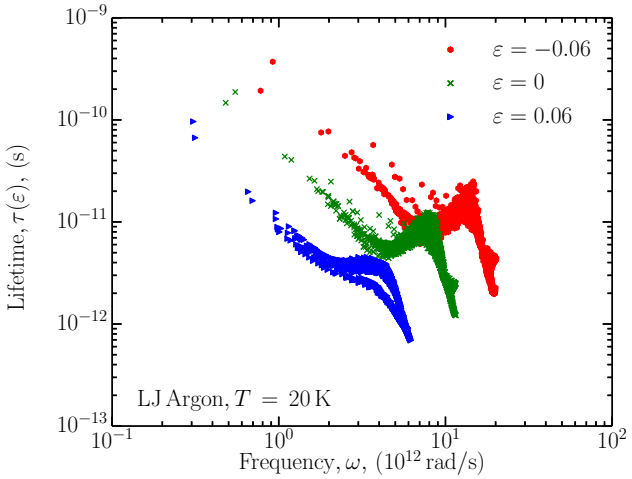

Figure 3.3: Strain-dependent phonon lifetimes for LJ argon.

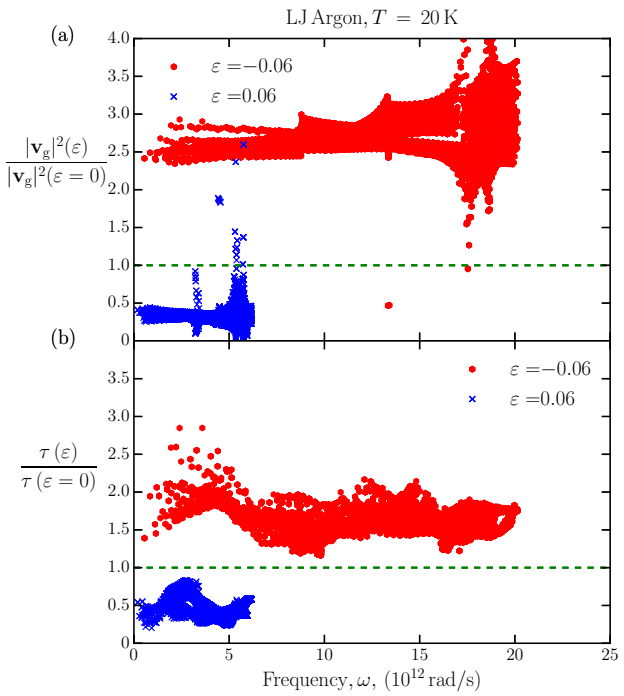

Figure 3.4: LJ argon phonon mode properties normalized by zero strain values for $N_{\mathrm{MK}} = 50$: (a) squared group velocity and (b) lifetime.

3.3.1.2 Group Velocities and Lifetimes

We now seek to understand the thermal conductivity trend in Fig. 3.1 by considering the phonon mode properties. The changes in group velocity can be visualized by considering the [100] phonon dispersion plotted in Fig. 3.2 for strains of −0.06, 0, and 0.06. The maximum phonon frequency decreases as the system moves from compression to tension, causing the group velocities to decrease. Since the dispersion is calculated using harmonic force constants, it only captures the harmonic effect of strain. The phonon lifetimes are plotted in Fig. 3.3. As with the group velocities, the lifetimes decrease as the system moves from compression to tension.

We quantify the mode-level changes by dividing the strain- and mode-dependent squared group velocities ($|\mathbf{v}_g|^2$) and lifetimes by their zero-strain counterparts. The results for

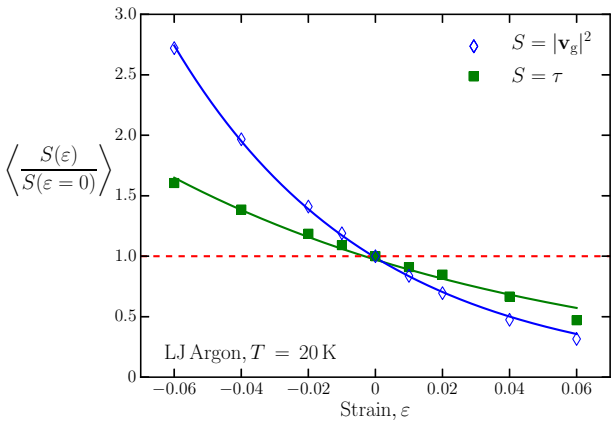

Figure 3.5: Normalized mean lifetimes and mean squared group velocities for LJ argon for $N_{\mathrm{MK}} = 50$. Each data set is fit to an exponential function (solid lines).

strains of -0.06 and 0.06 are plotted in Figs. 3.4(a) and 3.4(b). The individual mode scalings of squared group velocity [Fig. 3.4(a)] and lifetime [Fig. 3.4(b)] are relatively flat, with effectively no spectral dependence. The relative change in the squared group velocity with strain is larger than that of the lifetime.

To get a system-level measure of the mode scalings, we average the normalized properties at each strain. The results are plotted in Fig. 3.5. The normalized squared group velocities and lifetimes both scale exponentially and the least-squares fits are plotted in Fig. 3.5.[2] The exponential constant is -17 for the squared group velocity and -9 for the lifetime. Therefore, the group velocity scaling is $\exp(-8\,\varepsilon)$ stronger than that of the lifetime, making it the dominant factor in thermal conductivity changes with strain.

3.3.2 Silicon

3.3.2.1 Thermal Conductivity

The strain-dependence of the thermal conductivity of silicon predicted from first-principles is plotted in Fig. 3.6. Thermal conductivity is relatively constant under compression and

[2]It is also possible to fit the data to a power-law scaling. The final conclusion is unchanged.

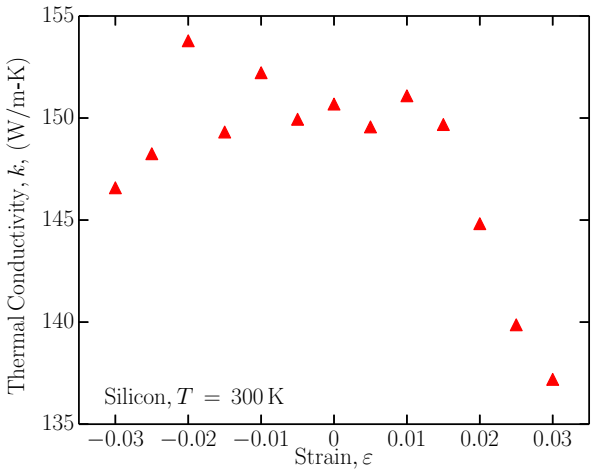

Figure 3.6: Strain dependence of silicon thermal conductivity predicted from first-principles.

then decreases with increasing tension. This trend is in contrast to that for LJ argon, where the thermal conductivity monotonically decreased in moving from compression into tension (Fig. 3.1). The overall change in thermal conductivity is smaller in silicon ($\sim 15\%$) as compared to LJ argon (two orders of magnitude).

3.3.2.2 Heat Capacity, Group Velocities, and Lifetimes

In interpreting the silicon data at the phonon mode-level, we consider changes in heat capacity, squared group velocity, and lifetime. In Fig., 3.7 we plot the silicon dispersion. The maximum frequency decreases as the system moves from compression into tension, but the difference is less than that observed in LJ argon (Fig. 3.2). The stretching of the dispersion results in a decrease in group velocity under tension with the exception of the transverse acoustic branch, which reduces in frequency near the Brillouin zone edge. The silicon lifetimes plotted in Fig. 3.8 display an increase of the lifetimes in tension, opposite to the trend for LJ argon (Fig. 3.3).

The mode-dependent property normalizations to the zero strain values are plotted in

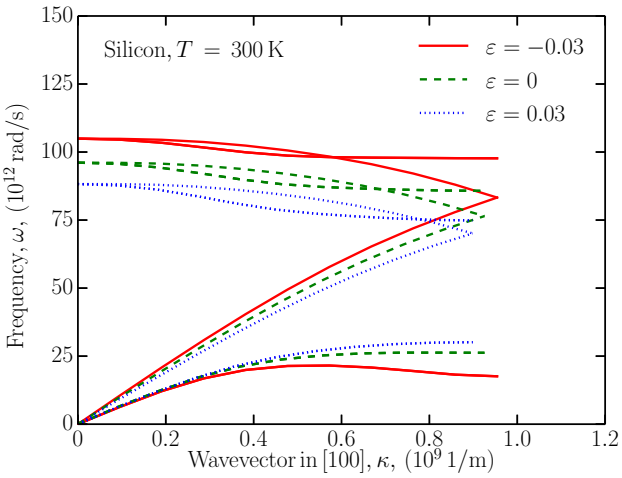

Figure 3.7: [100] strain-dependent phonon dispersion for silicon.

Figs. 3.9(a), 3.9(b), and 3.9(c). Because the thermal conductivity of silicon is dominated by low-frequency acoustic phonons,[38, 66] we do not include modes with frequencies past the point where 90% of the thermal conductivity is realized. This choice eliminates modes that do not meaningfully contribute to the thermal conductivity, but can show large scatter in the normalizations. The changes in mode properties with strain are smaller than the changes observed in LJ argon, which is consistent with the smaller changes in thermal conductivity. The heat capacity follows a predictable scaling from Bose-Einstein statistics. As the phonon mode's frequency (i.e., energy) decreases in moving from compression to tension, its heat capacity decreases. No trend in the normalized squared group velocities is indiscernible from Fig. 3.9(b). There is an overall reduction of lifetimes with compressive strain and an overall increase in lifetimes with tensile strain, The squared group velocities and lifetimes show more spectral dependence than in LJ argon.

In Fig. 3.10, we plot the mean values of the normalized properties versus strain, as plotted in Fig. 3.5 for LJ argon. Before performing the average, we exclude any group velocity normalizations that are greater than a value of five. In doing so, we eliminate non-physical values due to the effects of the Van Hove singularities (i.e., where the group

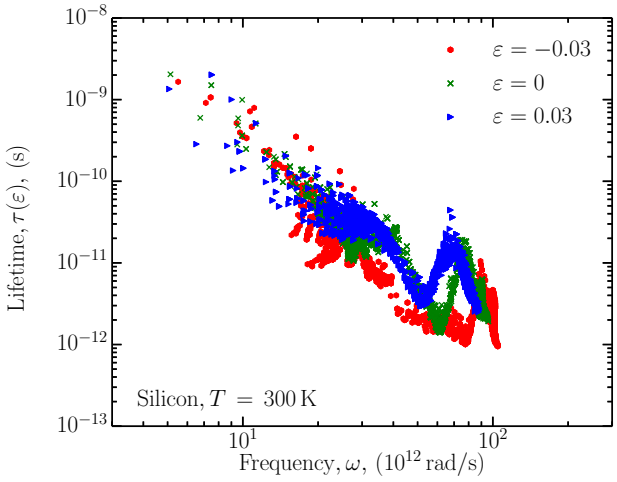

Figure 3.8: Strain-dependent phonon lifetimes for silicon.

velocity approaches zero). The phonon frequencies decrease as the system moves from compression to tension, and thereby the heat capacity and squared group velocity also decrease. These changes are related to harmonic effects. There is an increase in the lifetimes when moving from compression to tension over the entire strain range explored, opposite to what is observed in LJ argon. These competing effects balance in compression, leading to a constant thermal conductivity. In tension, the heat capacity and squared group velocity effects dominate, leading to a decrease in thermal conductivity. Using MD simulations, Li et al. found a monotonic decrease in the thermal conductivity of Tersoff silicon in moving from compression to tension. They attribute this behavior to a reduction in the group velocities and heat capacities[11]. We note that they explored a larger strain range (-0.09 to 0.12) and used an empirical potential with the classical statistics inherent to MD simulation.

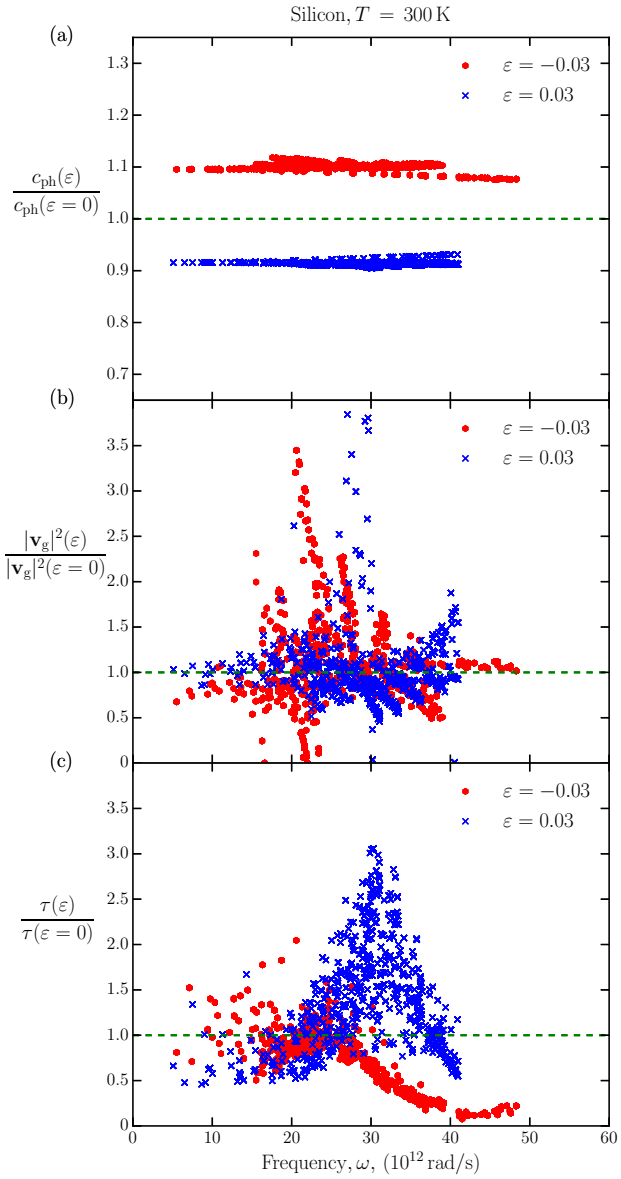

Figure 3.9: Silicon phonon mode properties normalized by zero strain values for $N_{\mathrm{MK}} = 20$: (a) heat capacity, (b) squared group velocity, and (c) lifetime.

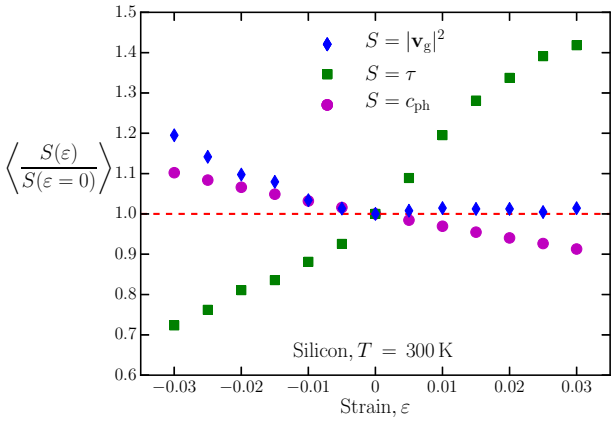

Figure 3.10: Normalized mean lifetimes, mean squared group velocities, and heat capacities for silicon for $N_{\text{MK}} = 20$.

3.3.3 Potential Well

3.3.3.1 Root Mean Squared Displacement

The strain-dependence of the phonon lifetimes is dissimilar in LJ argon and silicon. In LJ argon, the lifetimes decrease as the system moves from compression to tension (Figs. 3.3 and 3.5), while in silicon they increase (Figs. 3.8 and 3.10). To explore these opposite trends, we analyze the local potential well felt by atoms in the two systems. First, the root mean-square (RMS) displacement is calculated to quantify how much of the unit cell is explored by an atom. Second, the local potential energy well is mapped to decompose the potential energy into harmonic and anharmonic components.

The RMS displacement $\langle |\mathbf{u}|^2 \rangle^{1/2}$ can be calculated through MD simulations by time-averaging the positions or from the harmonic phonon properties using the analytical expression [77]

$$\langle |\mathbf{u}|^2 \rangle^{1/2} = \left[\frac{\hbar}{n N_{\text{MK}}^3} \sum_{\alpha,j}^{3,n} \sum_{\mathbf{q},\nu}^{N_{\text{MK}}^3,3n} f(\mathbf{q},\nu) \frac{e(\mathbf{q}\ {}^{j}_{\nu}\ {}_{\alpha}) \, e^*(\mathbf{q}\ {}^{j}_{\nu}\ {}_{\alpha})}{m \, \omega(\mathbf{q},\nu)} \right]^{1/2}. \tag{3.2}$$

For the LJ argon crystal, the RMS displacement is calculated directly using the MD

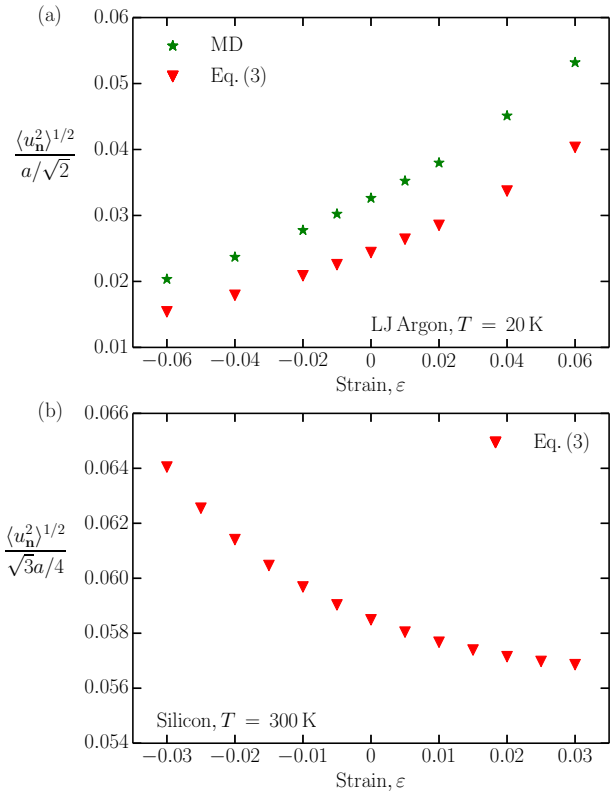

Figure 3.11: Strain-dependent RMS displacements normalized by the nearest-neighbor distance: (a) LJ argon using time-averaging of the atomic positions in MD simulation and Eq. (3.2), and (b) silicon using Eq. (3.2).

simulations and using Eq. (3.2). We use classical phonon population for $f(\mathbf{q},\nu)$ so as to make the prediction comparable to the MD result. The value is normalized by the nearest-neighbor distance, $a/\sqrt{2}$, for each strain and the results are plotted in Fig. 3.11(a). The RMS displacement for LJ argon from MD is greater than that calculated from Eq. (3.2), which we attribute to the inclusion of the full anharmonicity in the MD simulations. We note that Turney et al.[63] erroneously included the zero-point energy in the phonon occupation in Eq. (3.2) yielding accidental agreement with MD simulation results. As it is computationally prohibitive to run DFT-driven MD simulations, the RMS displacement for silicon is calculated only using Eq. (3.2). The results, normalized by the nearest-neighbor distance, $\sqrt{3}a/4$, are plotted in Fig. 3.11(b). We use the Bose-Einstein distribution for the distribution function to be consistent with the thermal conductivity prediction.

The normalized RMS displacement for LJ argon more than doubles from compression to tension. The percentage of the unit cell that is accessible by the atom is reduced in compression and increased in tension. In silicon, the opposite trend is observed: the normalized RMS displacement decreases from compression to tension. Since the atom is only allowed to displace from equilibrium through the natural energy of the thermal fluctuations, $k_{\mathrm{B}}T$, the further the atom deviates from the equilibrium position, the more phonon-phonon scattering occurs (i.e., the system is more anharmonic). The RMS data for LJ argon and silicon are therefore consistent with the lifetime data in Figs. 3.3, 3.5, 3.8, and 3.10.

3.3.3.2 Potential Energy Surface Mapping

To further understand the difference in the lifetime trends, we next performed molecular statics (i.e., single-point energy) calculations for LJ argon and silicon to map the potential energy surface experienced by an atom. A single atom is displaced in small increments along the [100] direction and the total potential energy of the system is calculated. This

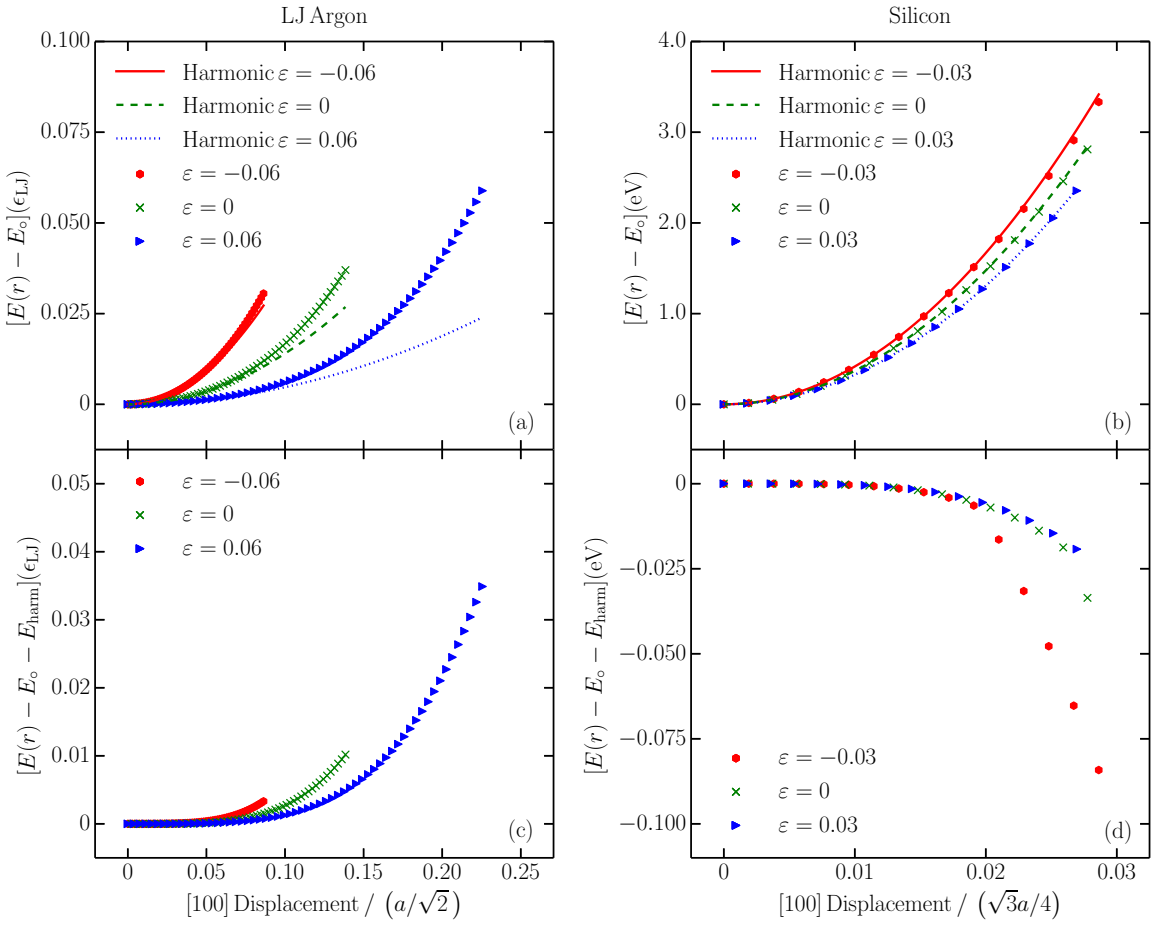

Figure 3.12: Potential energy changes for displacement in the [100] direction for multiple strains. (a) LJ argon displacement energy and harmonic fit. (b) Silicon displacement energy and harmonic fit. (c) LJ argon anharmonic energy. (d) Silicon anharmonic energy.

analysis is performed up to the RMS displacement.

In Figs. 3.12(a) and 3.12(b), the displacement energy (i.e., the energy minus the zero-displacement energy) is plotted for LJ argon and silicon. To capture the harmonic part of the curve, a parabola is fit to the first four displacements and is plotted over the full range. The curvature of the harmonic potential decreases in both argon and silicon as the strain is increased. For both systems, the harmonic curve deviates from the full potential well as the atom is displaced further from its equilibrium position, an indication of increasing anharmonicity. The deviation from the harmonic curve is smaller in silicon as compared to argon, which is expected because silicon is stiffer.

We next subtract the harmonic fits from the potential wells and the results are plotted in Figs. 3.12(c) and 3.12(d). For LJ argon [Fig. 3.12(c)], the anharmonic contribution is positive for all strains. The anharmonicity at the RMS displacement increases as the strain is increased, thereby increasing phonon-phonon scattering and reducing the lifetimes (Fig. 3.5). In silicon [Fig. 3.12(d)], the anharmonic contribution is negative for all strains and the greatest amount of anharmonicity (i.e., deviation from the harmonic potential) is felt under compression. This decreasing anharmonicity from compression to tension increases the lifetimes (Fig. 3.10).

In silicon, we observe competing effects between harmonic (i.e., heat capacity and group velocity) and anharmonic (i.e., lifetime) effects. These two effects are thus decoupled and need not scale together under strain, as seen in LJ argon. Compression does not just increase the "stiffness,"[56] but can induce positive or negative changes in the anharmonic contribution to the energy potential. The opposite behavior of the LJ argon and silicon systems demonstrates the need to separately inspect harmonic and anharmonic effects when interpreting strain-dependent properties.

3.4 Summary

We applied atomistic calculations to predict the strain-dependent phonon properties and thermal conductivity of LJ argon and silicon. LJ argon undergoes an exponential decrease in thermal conductivity with increasing strain (Fig. 3.1). For silicon, as shown in Fig. 3.6, the thermal conductivity remains constant under compressive strain and decreases with increasing tensile strain.

For LJ argon, the mode-averaged lifetimes and squared group velocities both decrease exponentially as the system moves from compression to tension, with the squared group velocity effect dominating the thermal conductivity (Fig. 3.5). For silicon, the squared group velocities decrease from compression to tension, while the lifetimes increase anomalously, as shown in Fig. 3.10.

To explain this behavior, we examined the local potential well. The normalized RMS displacement, plotted in Fig. 3.11(a) and 3.11(b), describes how much anharmonicity is experienced. In LJ argon, the normalized RMS displacement increases as strain is increased while for silicon it decreases as strain is increased. These trends are consistent with the lifetime trends, which is physically justified as larger displacements will lead to more anharmonicity and reduced lifetimes.

We performed molecular statics to map the local potential well in the [100] direction. As shown in Figs. 3.12(a) and 3.12(b), for LJ argon, the anharmonic contribution increases with increasing strain, similar to how the harmonic contribution increases. For silicon, however, the anharmonic contribution decreases with increasing strain, opposite to the argon trend [Figs. 3.12(c) and 3.12(d)]. Strain can thus affect the anharmonic contribution to the potential differently than it affects the harmonic contribution, qualitatively changing the scaling of the phonon lifetimes.

Phonon-Boundary Scattering in Nanoporous Silicon Films

4.1 Introduction

As the porosity of a solid increases, its effective thermal conductivity decreases. The decreased cross-sectional area and the increased tortuosity that the heat flux must follow can be accounted for by solving the heat diffusion equation using the bulk (i.e., intrinsic) thermal conductivity. We will refer to the ratio between the solved effective thermal conductivity and the intrinsic thermal conductivity as the continuum correction factor. If the dimensions are reduced until they are on the order of the phonon mean free paths, there is an additional reduction due to phonon-boundary scattering. This additional scattering can be quantified computationally by accounting for the geometry's effect and modifying the phonon mean free paths (the group velocity and heat capacity are unchanged). The thermal conductivities of silicon thin films with periodic pore arrays (i.e., nanoporous films) and square silicon nanowires are predicted at a temperature of 300 K. Phonon-boundary scattering is included by applying three Monte Carlo-based techniques that treat phonons as particles. The bulk phonon properties are obtained from lattice dynamics calculations driven by first-principles calculations.

Thin films of crystalline silicon with periodic through holes have been previously studied[16, 17, 18, 19, 20, 21, 22, 23, 24, 25, 26, 27, 28, 29, 29, 30, 31, 32, 33]. We will refer to such structures as nanoporous films. Due to silicon amorphization at the pore edges during fabrication and the formation of an amorphous native oxide layer when exposed to air,

nanoporous films are not truly periodic from an atomistic standpoint[26]. The thin film boundaries and pore walls both scatter phonons, which are the dominant thermal energy carriers in silicon. The thermally-relevant bulk phonon mean free paths span five orders of magnitude at room temperature, from 1 nm to 100 μm, and the wavelengths of the thermally-relevant phonons are 1 to 5 nm[38]. The nanostructuring reduces the in-plane thermal conductivity to 1-70% of the bulk value at room temperature[16, 19, 43]. The suppression of the phonon thermal conductivity makes nanoporous silicon films attractive as a possible thermoelectric material[17, 34]. These structures provide a large parameter space to explore in terms of the pore lattice design, pore size, and pore spacing.

To further understand and ultimately predict the experimentally-measured reduction in thermal conductivity, nanoporous silicon films have also been modeled computationally. When the structure is small enough [i.e., feature sizes $\mathcal{O}(1\text{ nm})$], the dynamics can be modeled atomisitically and the thermal conductivity can be predicted from molecular dynamics simulations[34, 78, 79]. For thicker films and when the pore feature sizes are on the order of tens of nanometers or larger, solving the atomistic dynamics explicitly is not possible due to computational limitations. Mesoscale approaches that modify the bulk phonon properties based on the nanostructure geometery are required[43, 44, 45, 46, 47, 48, 49, 50, 80, 81, 82, 83]. The effect of the boundary scattering on phonon transport and thermal conductivity can be determined by (i) spatially and temporally solving the Boltzmann transport equation in the geometry of interest[43, 44, 45, 46, 47, 48, 49, 50] or (ii) directly modifying the phonon mean free paths, as we explore herein.

Controversy exists as to whether or not wave-like (also referred to as coherent) phonon effects contribute to thermal transport in nanoporous silicon films at room temperature (i.e., are phonon modes related to the secondary periodicity introduced by the pores relevant). Such effects have been observed at cryogenic temperatures, where the dominant

phonon wavelengths are similar to the feature sizes[21, 84, 85, 86, 87]. Jain et al.[80] modeled nanoporous silicon films with feature sizes greater than 100 nm using the free path sampling technique and compared their in-plane thermal conductivity predictions to the experimental measurements of El-Kady et al.[19] at a temperature of 300 K. They reproduced the fine structure of the experimental values without the inclusion of coherent effects. Alaie et al. experimentally measured the in-plane thermal conductivity of nanoporous silicon films with a minimum feature size of 250 nm at room temperature[26]. Through comparison to analytical models, they concluded that the thermal conductivity had a contribution from coherent phonon modes. Lee et al. measured the in-plane thermal conductivity of nanoporous silicon films with periodic and aperiodic pores[33]. Their thermal conductivity predictions from ray-tracing calculations agree with the measurements on both the periodic and aperiodic structures within the experimental uncertainty. They concluded that coherent effects are not important at room temperature in nanoporous silicon films with feature sizes of 100 nm or larger.

The importance of pathways for ballistic phonons transport, i.e., line-of-sight, in silicon nanoporous films has also been investigated. Using a Boltzmann transport equation-based approach, Tang et al. found that staggering square pores in a film reduces the thermal conductivity compared to aligned pores[43]. Experimentally, Anufriev et al. measured a difference in the thermal conductivity of silicon structures of the same porosity with simple cubic and staggered pores[87]. They attribute a lower thermal conductivity in the staggered geometry to the boundary scattering of ballistic phonons.

The objective of this study is to compare thermal conductivity predictions for square silicon nanowires and nanoporous silicon films inspired by the structures of Alaie et al. from three Monte Carlo-based techniques for modeling phonon-boundary scattering: (i) the free path sampling technique of McGaughey and Jain,[51] (ii) the isotropic ray-tracing

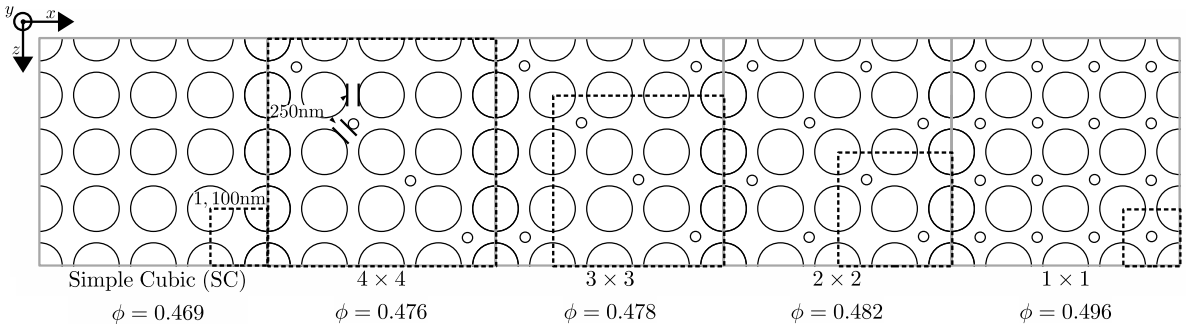

Figure 4.1: Schematic diagrams of the top views of the five nanoporous films. The minimum repeating cell is outlined using a dashed line. The structures are periodic in the $x-$ and $z-$directions.

technique of Hori et al.,[52] and (iii) a modal ray-tracing technique that we introduce. The nanoporous structures are described in Sec. 4.2.1 and the bulk phonon calculations are detailed in Sec. 4.2.2. The Monte Carlo techniques are presented in Secs. 4.2.3-4.2.6 and compared in terms of their underlying assumptions and computational requirements. The predictions are presented and analyzed in Sec. 4.3, where we find no evidence for the existence of coherent phonon effects in the structures of Alaei et al. For the nanoporous films, we investigate how limiting the line-of-sight of phonons influences thermal conductivity.

4.2 Methodology

4.2.1 Nanoporous Structures

The five nanoporous silicon films to be studied are based on the fabricated samples of Alaie et al.[26] and are shown in Fig. 4.1. The film thickness is 366 nm and the pores completely penetrate the film. The large pores are present in all five structures. They have a radius of 425 nm and a periodicity of 1,100 nm such that the edge-to-edge distance between them is 250 nm. Interpenetrating small pores are introduced with varying periodicity leading to

the 1×1, 2×2, 3×3, and 4×4 structures. The structure without any interpenetrating small pores will be referred to as the simple cubic (SC) structure. The small pore radius of 102.8 nm is chosen so that the distance from its edge to the nearest large pore edge is 250 nm (i.e., the minimum feature size is the same in all five structures). The resulting porosities range from 0.469 to 0.496.

4.2.2 Bulk Phonon Calculation

To predict the thermal conductivity of the silicon nanostructures, we use the bulk phonon properties with the mean free paths modified with a boundary scattering model (Secs. 4.2.3-4.2.6). In making this choice, we are assuming that: (i) there are no confinement effects (i.e., there are no bulk wavelengths that cannot exist in the nanostructure), as the wavelengths of thermally-relevant phonons in silicon at room temperature (1-5 nm)[38] are much smaller than the minimum feature size, and (ii) phonon modes that exist based on the second periodicity of the nanoporous film (i.e., coherent modes) do not contribute to thermal transport. Subsequently, our calculations follow a particle-based transport description where Eq. (2.28) (Sec. 2.3) is valid.

The phonon frequencies, which provide the volumetric heat capacity (from Bose-Einstein statistics) and the group velocity vector, and bulk mean free paths are obtained using HLD and ALD (Secs. 2.2.1 and 2.2.2) for bulk silicon at a temperature of 300 K[36, 37, 38, 54, 67]. The required force constants were calculated using the density functional theory package QUANTUM ESPRESSO[73], with an electronic Monkhorst-Pack wavevector grid of $8 \times 8 \times 8$ and an energy cutoff of 60 Ry on the primitive (i.e., two-atom) unit cell. We used the local density approximation exchange-correlation with the norm-conserving pseudopotential Si.pz-vbc.UPF. The harmonic force constants were obtained through density functional perturbation theory calculations using a Monkhorst-Pack phonon wavevector

grid of $8 \times 8 \times 8$, which was interpolated to a $24 \times 24 \times 24$ wavevector grid resulting in 82,944 phonon modes. The cubic force constants were calculated from finite displacements of a 216-atom supercell. The predicted bulk silicon thermal conductivity is 152 W/m-K,[1] which is converged to within 2% for the chosen parameter set[88]. This value agrees with the experimentally measured thermal conductivity for isotopically pure silicon of 153 $\pm$5 W/m-K[75]. As discussed by Jain and McGaughey, we note that the choice of exchange-correlation and pseudopotential can change the final thermal conductivity value by up to 21 W/m-K for the same convergence parameters[88]. We ignore phonon-isotope scattering as it can obscure the boundary scattering effects. Isotopically pure silicon has a 10% higher thermal conductivity than natural silicon[75]. The continuum correction factor for each geometry is calculated using COMSOL Multiphysics® to solve the heat diffusion equation using the finite element method.

4.2.3 Free Path Sampling

The free path sampling technique takes pre-calculated bulk phonon properties, specifically the group velocity vector and the intrinsic mean free path, and calculates the effective mean free path based on the geometry of the structure[51]. For each phonon mode, a set of phonons with random free paths (sample from a Poisson distribution based off of the mean free path) travel until they reach their free path distance of they encounter a boundary. Then the free path is redefined off of this distance. A new mean free path, that includes the intrinsic scattering and the boundary scattering is now defined for that mode. Eq. (2.26) is then evaluated using the new mean free paths along with the bulk heat capacities and group velocities. In the periodic structures modeled here, the initial position is taken in

[1]Our predicted bulk thermal conductivity value of 152 W/m-K is higher than that of 144 W/m-K reported by Jain et al.[88] for the same exchange-correlation and pseudopotential. The difference is a result of the harmonic force constants, calculated here from ph.x 6.0, while Jain et al. used ph.x 5.0.2.

the minimum repeating cell. The method is described in more detail in Sec. 2.4.1. Free path sampling does not use the Matthiessen rule as opposed to the other Monte Carlo techniques investigated here.

4.2.4 Isotropic Ray-Tracing

The isotropic ray-tracing technique developed by Hori et al. calculates a single boundary scattering mean free path for all modes, $\bar{\Lambda}_{\text{bdy}}$, based on ballistic transmission (i.e., in the absence of intrinsic scattering)[52]. From an isotropic Landauer formalism, the ballistic (i.e., boundary-scattering) effect on thermal transport in a geometry can be evaluated. Rays starting from different angles at one end of a structure are traced and scattered diffusely (according to Lambert cosine law) off of boundaries until either end of the structure is reached. From these traces a transmission ratio is calculated. Using the Landauer formalism the average boundary scattering mean free path, $\bar{\Lambda}_{\text{bdy}}$, is calculated. This is combined with the intrinsic mean free path, Λ_{pp}, to create an effective mean free path through use of the Matthiessen rule, Eq. (2.32). For more details on isotropic ray-tracing consult Sec. 2.4.2.

It is worth noting that the applicability of the Matthiessen rule to phonon-boundary and phonon-isotope scattering has recently been investigated. Luisier found that the Matthiessen rule overestimated the thermal conductivity of roughened silicon nanowires due to an additional scattering contribution of localized surface modes coupled to phonon-phonon scattering[89]. Similarly, Feng et al. reported an overestimation of thermal conductivity calculated by the Matthiessen rule in bulk silicon that resulted from a failure to account for coupling between impurity and phonon-phonon scattering[90].

4.2.5 Modal Ray-Tracing

The ray-tracing formulation of Hori et al. assumes that the phonon dispersion is isotropic and ignores modal details. To investigate the difference between free path sampling and isotropic ray-tracing, we introduce a formalism of the ray-tracing technique where the boundary mean free path is obtained on a modal basis. This is accomplished by performing the derivation using the Landauer formalism without invoking the isotropic approximation. This approach allows us to eliminate the isotropic approximation in the ray-tracing calculation, but not the use of the Matthiessen rule.

The implementation of the technique is the same as isotropic ray-tracing except the transmission ratio is calculated per each phonon mode, where the modes are distinguished by their initial angle based on the group velocity vector. This results in a mode-specific transmission ratio, $\mathcal{T}(\mathbf{q}, \nu)$. The Matthiessen rule (Eq. 2.34) is again employed to calculate the effective mean free path and substituted into Eq. 2.28. The modal ray-tracing is detailed in Sec. 2.4.3 and the Landauer derivation without the isotropic assumption is available in Appendix A.

4.2.6 Convergence and Comparison

The square nanowire is finite in the x- and y-directions and is infinite in the z-direction. For free path sampling, it is modeled by applying periodic boundary conditions in the z-direction. The free path sampling calculations were performed with 100,000 samples of each phonon mode. The calculation was run with ten different initial seeds and the 95% confidence interval on the predicted thermal conductivity is less than 0.1 W/m-K. To approximate an infinite structure for the isotropic and modal ray-tracing calculations, the length must be increased until the predicted thermal conductivity is converged to a set tolerance. For all wire side lengths considered, we performed isotropic ray-tracing calcula-

tions with a length of 1 mm in the z-direction with 100,000 samples of each zenith angle and initial position. The calculation was run with ten different initial seeds and the 95% confidence interval is less than 0.5 W/m-K. Increasing the length to 10 mm led to a difference in thermal conductivity of less than 2 W/m-K. Modal ray-tracing calculations with a length of 1 mm in the z-direction were performed with 100,000 samples of each phonon mode. The calculation was run with ten different initial seeds and the 95% confidence interval is less than 0.5 W/m-K. Increasing the length to 10 mm led to a difference in the thermal conductivity of less than 2 W/m-K.

The minimum repeating structures for the each of the nanoporous silicon films are outlined by dashed lines in Fig. 4.1. For the free path sampling calculations, this structure is chosen and periodic boundary conditions are applied in the in-plane (x- and z-) directions. The free path sampling calculations were performed with 100,000 samples of each phonon mode. The calculation was run with ten different initial seeds and the 95% confidence interval on the predicted thermal conductivity is less than 0.1 W/m-K. Isotropic ray-tracing calculations with 50 cell repetitions in the z-direction were performed with 100,000 samples of each zenith angle and initial position. The calculation was run with ten different initial seeds and the 95% confidence interval is less than 0.1 W/m-K. Increasing the number of cells by ten led to a difference in thermal conductivity of less than 0.2 W/m-K. Modal ray-tracing calculations with a length of 50 cell repetitions in the z-direction were performed with 100,000 samples of each phonon mode. The calculation was run with ten different initial seeds and the 95% confidence interval is less than 0.1 W/m-K. Increasing the number of cells by ten led to a difference in the thermal conductivity of less than 0.1 W/m-K.

A comparison of the three techniques is provided in Table 4.1. For the specified phonon grid and convergence parameters, free path sampling is the most computationally efficient for our chosen material and structures. Isotropic ray-tracing and modal ray-tracing require

Table 4.1: Comparison of free path sampling, isotropic ray-tracing, and modal ray-tracing techniques for including phonon-boundary scattering in thermal conductivity prediction.

Technique	Normalized Time	Material Independent?	Mode Dependent?	Matthiessen Rule?
Free Path Sampling	1	No	Yes	No
Isotropic Ray-Tracing	5	Yes	No	Yes
Modal Ray-Tracing	2,750	No	Yes	Yes

5 and 2,750 times more computational effort. It is important to note that the computational cost of free path sampling and modal ray-tracing scale linearly with number of modes, while that for isotropic ray-tracing is constant because it is mode-independent. The computational cost for modal ray-tracing could be reduced by calculating transmission ratios for a grid of azimuthal and zenith angles and then interpolating the transmission ratio for a specific phonon mode based on the direction of its group velocity vector.

Isotropic ray-tracing is independent of material and the $\bar{\Lambda}_{\text{bdy}}$ calculated for a geometry can be used for multiple materials. This single value, however, is applied to all phonon modes. In contrast, free path sampling and modal ray-tracing depend on both geometry and material. Separate calculations must thus be performed for every combination, but they provide a mode-dependent boundary scattering mean free path. The Matthiessen rule, applied in isotropic ray-tracing and modal ray-tracing, potentially limits these techniques by assuming that the phonon-boundary scattering rate is independent of the intrinsic phonon-phonon scattering.

4.3 Results

4.3.1 Square Nanowire

We begin by studying thermal transport in square silicon nanowires with side lengths a

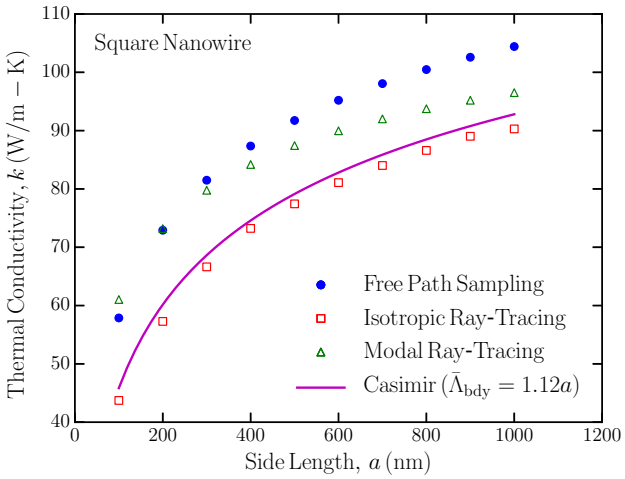

Figure 4.2: Axial thermal conductivity of square silicon nanowires predicted by the three boundary scattering techniques and by the Casimir limit ($\bar{\Lambda}_{\text{bdy}} = 1.12a$). The 95% confidence interval is contained within the size of the markers.

ranging from 100 to 1,000 nm at a temperature of 300 K. The thermal conductivity predictions from free path sampling, isotropic ray-tracing, and modal ray-tracing are plotted in Fig. 4.2. Also plotted is the thermal conductivity calculated from the analytical Casimir limit ($\bar{\Lambda}_{\text{bdy}} = 1.12a$) and the bulk phonon mean free paths by use of Eqs. (2.28) and (2.32). Thermal conductivity increases by a factor of two with increasing side length for all three techniques, exhibiting a more rapid change for the smaller wires. Isotropic ray-tracing closely follows the Casimir limit prediction, as expected, and as previously shown by Hori et al[52]. The free path sampling and modal ray-tracing predictions are 6 to 40% higher than those from isotropic ray-tracing. We note that the Casimir limit is only strictly valid in the limit where other scattering mechanisms have a much longer length scale than the boundary scattering feature sizes. This condition is not met for all phonon modes in silicon at room temperature, where the bulk mean free paths are as short as 1 nm.

The thermal conductivity accumulation functions, k_{accum}, for the three Monte Carlo techniques for side lengths of 100 and 1,000 nm are plotted in Fig. 4.3. These curves

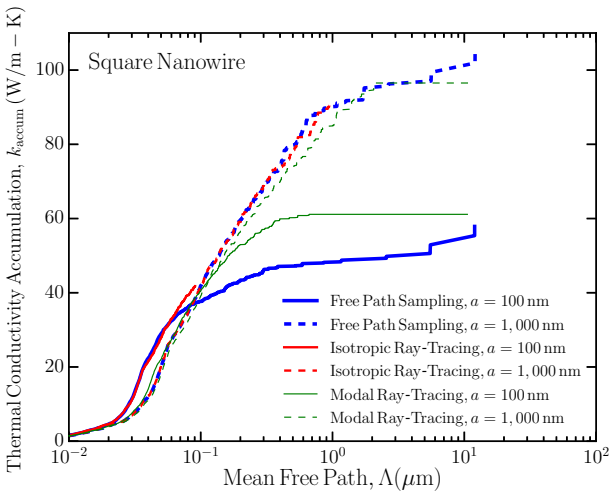

Figure 4.3: Thermal conductivity accumulation of square silicon nanowires with side lengths of 100 and 1,000 nm as predicted by the three boundary scattering techniques.

represent the cumulative contribution of phonon modes with increasing mean free path to thermal conductivity. At a side length of 100 nm, the isotropic ray-tracing accumulation function spans one order of magnitude of mean free paths and terminates at 100 nm. This maximum mean free path is two orders of magnitude smaller than that for free path sampling and modal ray-tracing, where phonons spanning three orders of magnitude contribute to thermal conductivity. Isotropic ray-tracing only calculates one boundary scattering mean free path and applies it to all the phonon modes regardless of their direction [Eq. (2.32)]. With the use of the Matthiessen rule, no phonon mode can have a larger mean free path than $\bar{\Lambda}_{\text{bdy}}$ and thereby all mean free paths must terminate by this value, leading to an unphysically small maximum mean free path. Free path sampling and modal ray-tracing, on the other hand, account for the boundary scattering at the modal level. The directionality captured in these two techniques allows for phonons traveling primarily axially to have little to no boundary scattering compared to modes traveling primarily in the plane of the wire. Because isotropic ray-tracing averages the boundary scattering in all directions, it fails to physically capture these long mean free path modes in the nanowire.

Although free path sampling and modal ray-tracing produce similar thermal conductivities and accumulation functions, the predictions are not identical. The discrepancies could be a consequence of the use of the Matthiessen rule in modal ray-tracing.

When the side length is 1,000 nm, the maximum mean free path for free path sampling and modal ray-tracing is one order of magnitude larger than that for isotropic ray-tracing. As the wire size is increased and the boundary scattering is decreased, the importance of including the directional dependence of boundary scattering is reduced. As the side length of the wire is further increased and the boundary scattering decreases, the predictions of all three techniques will converge to the bulk thermal conductivity and its accumulation function.

4.3.2 Nanoporous Films

4.3.2.1 Thermal Conductivity

We now investigate the nanoporous silicon films of Alaie et al. that were described in Sec. 4.2.1. The in-plane thermal conductivities calculated by the three Monte Carlo techniques are plotted versus porosity in Fig. 4.4(a). These thermal conductivities include both the continuum correction factor and the effect of phonon-boundary scattering. The thermal conductivities are reduced by a factor of five compared to silicon's bulk thermal conductivity and decrease with increasing porosity. The thermal conductivity predictions from free path sampling and isotropic ray-tracing differ by less than 1 W/m-K for each structure, a surprising agreement that was not found for the square nanowire. The modal ray-tracing values are 4-5 W/m-K higher.

The thermal conductivity predictions are compared to the experimental measurements of Alaie et al. in Fig. 4.4(b). Alaie et al. present thermal conductivities normalized by that

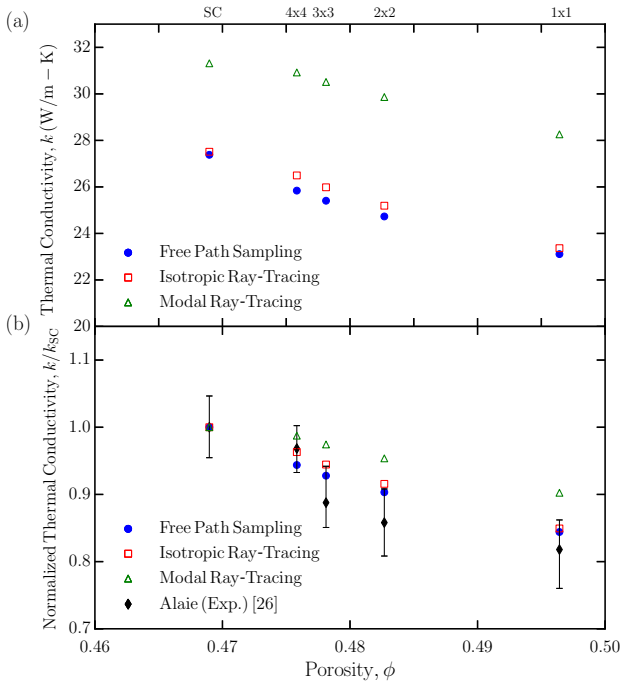

Figure 4.4: (a) In-plane thermal conductivities of nanoporous silicon films from our calculations. (b) In-plane thermal conductivities normalized to the SC structure from the experiments by Alaie et al. and from our calculations. The structures are identified in Fig. 4.1. The 95% confidence interval is contained within the size of the markers.

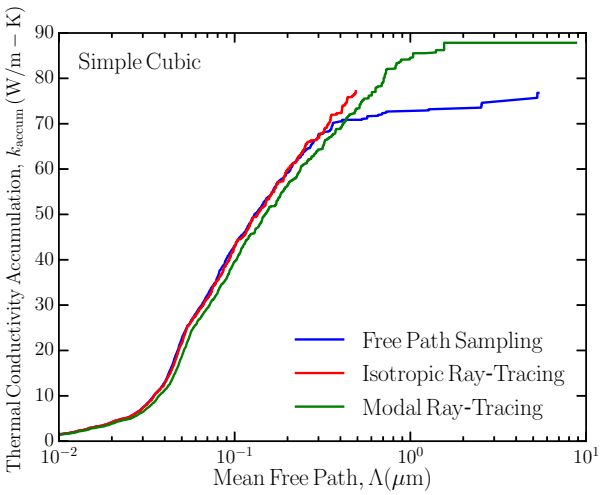

Figure 4.5: Thermal conductivity accumulation of SC nanoporous silicon films in the in-plane direction from free path sampling, isotropic ray-tracing, and modal ray-tracing. The continuum correction factor is not applied.

of a solid thin film of the same thickness, but do not provide the normalizing value. To compare our predictions to their measurements, we normalized the data in Fig. 4.4(a) to the SC structure. The Monte Carlo techniques all inherently treat phonons as particles such that they cannot capture coherent transport effects. All three techniques follow the experimental trend, with free path sampling lying within the experimental error bars for the four structures with interpenetrating small pores. This finding is consistent with the conclusions of Jain et al.[80] and Lee et al.[33], who found that particle-based models can predict the thermal conductivity of periodic silicon nanoporous films with feature sizes greater than 100 nm at room temperature.

4.3.2.2 Accumulation

The mean free path spectra produced by the Monte Carlo techniques are now compared by plotting the three thermal conductivity accumulation functions for the SC film in Fig. 4.5. The continuum correction factor is not included here so as to isolate the phonon-

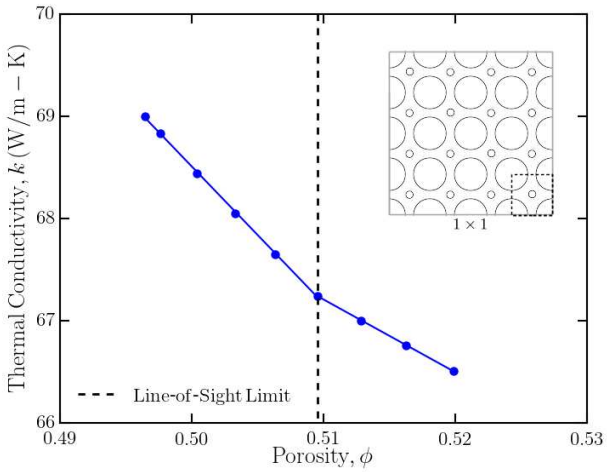

Figure 4.6: Effect of interpenetrating pore radius on thermal conductivity for the 1×1 structure. The solid lines correspond to linear fits to the data on either side of the line-of-sight limit. The continuum correction factor is not applied.

boundary scattering effect. The accumulations up to a mean free path 0.3 μm are similar, with modal ray-tracing 4 W/m-K below the other two techniques. Isotropic ray-tracing predicts a maximum mean free path that is an order of magnitude shorter than that from the other two techniques. As with the square nanowire, the origin of this difference is that phonon modes traveling in-plane encounter less scattering compared to modes traveling normal to the surfaces of the film. This geometrical effect is not captured by a single boundary scattering term. Because of their modal nature, free path sampling and modal ray-tracing realize these long mean free paths.

4.3.2.3 Line-of-Sight

We next examine the effect of line-of-sight, i.e., the distance a phonon can travel without boundary scattering. As noted in Sec. 4.2.6, free path sampling is less computationally expensive than the ray-tracing techniques. It is also more robust, as it does not require convergence with length, and captures directional effects as the scattering is calculated on

a modal basis. We thus use free path sampling exclusively in the subsequent analysis.

The line-of-sight creates a limit on the largest free path in a nanoporous film, which can drastically change with a minimal change in porosity. Using the 1×1 structure from Fig. 4.1, we increase the radius of the interpenetrating small pore from 102.8 nm to 140 nm. At a radius of 102.8 nm, a phonon with a group velocity vector in the z-direction can propagate unimpeded between the large and small pores. At a small pore radius of 125 nm, corresponding to a porosity of $\phi = 0.5095$, the path becomes blocked as there is no line-of-sight from the current cell past the first nearest-neighbor cell. In Fig. 4.6, the intrinsic thermal conductivity of the 1×1 structure is plotted versus porosity. The continuum correction factor is not included here so as to isolate the phonon-boundary scattering effect. Lines fit to each side of the crossover radius of 125 nm show a 2.5% difference in slope that abruptly changes at the line-of-sight limit.

To further examine the line-of-sight effect, the distribution of free paths of the first longitudinal acoustic mode in the z-direction (wavevector of 7.164×10^{-12} m^{-1}) for interpenetrating small pore radii of 120 and 130 nm are plotted in Figs. 4.7(a) and 4.7(b). For both structures, there is a steady decrease in the number of free paths from 200 to 1,100 nm. This feature is from phonons that initialize between the small pores, with the rare limiting case that a phonon modes starts at the edge of one small pore and travels the full 1,100 nm to the neighboring small pore. In the case of the 130 nm structure, this is the maximum distance a phonon can travel and limits the maximum free path. For a small pore size of 120 nm, the free paths extend more than two orders of magnitude past 1,100 nm due to the gap between the large and small pores. It is the contribution of phonon modes that propagate through these gaps that changes the thermal conductivity scaling at a porosity of 0.5095, as shown in Fig. 4.6.

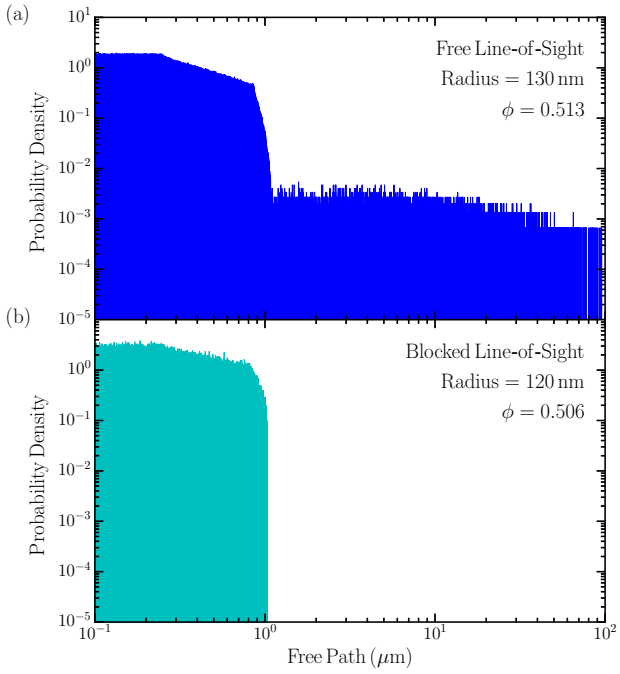

Figure 4.7: Probability density of free paths of the first [001] longitudinal mode calculated from free path sampling for the 1×1 structure with interpenetrating small pores of radius (a) 120 nm and (b) 130 nm.

4.4 Summary

We applied three Monte Carlo-based techniques for including the effects of phonon-boundary scattering in predicting the thermal conductivities of silicon square nanowires (Fig. 4.2) and silicon nanoporous films (Fig. 4.4) at a temperature of 300 K. All three techniques treat the phonons as particles and thus do not include coherent effects.

For the square nanowire, isotropic ray-tracing reproduced the Casimir limit while free path sampling and modal ray-tracing predicted larger thermal conductivities. The corresponding thermal conductivity accumulation functions show a large discrepancy in the range of and maximum mean free paths. Isotropic ray-tracing predicts that only mean free paths up to the wire side length contribute to thermal conductivity, while the other two techniques predict the existence of mean free paths up to the bulk values. This difference is a result of isotropic ray-tracing's failure to account for differences in scattering due to directionality, while the other two techniques calculate the boundary scattering on a modal basis.

The thermal conductivity predictions for the nanoporous films from the three techniques fall within a range of 6 W/m-K. Those from free path sampling agree with the measurements of Alaie et al.[26] within their respective uncertainties. This finding supports the conclusion reached by others[33, 80] that coherent effects do not contribute to thermal transport at room temperature. Using free path sampling, we examined the effect of the line-of-sight by considering the 1×1 structure with an increasing porosity, as shown in Fig. 4.6. There is a distinct change in trend at the transition from a free line-of-sight to a blocked line-of-sight. This finding highlights the importance of line-of-sight in the engineering of thermal transport in nanostructures.

Although the three techniques for including phonon-boundary scattering produced similar thermal conductivity magnitudes and trends, there are distinct differences in the modal

details. Isotropic ray-tracing reproduces the Casimir limit in the nanowire but truncates phonons that should not scatter with boundaries. This result emphasizes the limits of the applicability of the Casimir limit when applied to carriers with a broad spectrum of mean free paths. The formulation of the modal ray-tracing, albeit at a higher computational cost, discriminates the boundary scattering of phonon modes based on their direction of propagation. Free path sampling has the advantages of operating on a modal basis, not invoking the Matthiessen rule, and having the lowest computational cost.

Transient Grating

5.1 Introduction

Transient grating spectroscopy (TG), also known as impulsive stimulated light scattering, is a contactless optical laser based technique that is used to measure acoustic and thermal properties of materials. The generation of spatially periodic stress and temperature variations is achieved by interference of two coherent beams of lasers crossing at the sample, producing a sinusoidal grating of high intensity light. TG was first used to measure the thermal diffusivity of colored methanol, colored glycerin, and ruby by Eichler et al. in 1973[91]. Since then, the technique has been improved to account for both acoustic and thermal effects by Nelson et al. in 1982, and Maznev et al. introduced a heterodyne technique to amplify the signal in 1998[92]. Johnson et al. introduced a phase-control of the heterodyne technique for improving the selection of acoustic and thermal effects in 2012[93, 94]. It is this phase-controlled heterodyned TG setup that we have built and is the focus of this thesis.

Central to the TG experiment are two lasers, a pulsed "pump" laser and a continuous-wave "probe" laser. Two beams of the pump laser and two beams of probe laser are focused onto a single spot. The interference pattern created by the overlapping pump lasers sinusoidally heats the surface of the sample, i.e. the transient grating. As the probe passes though the transient grating created by the pump it is diffracted. The intensity of the diffraction is proportional to the changes created in the complex refraction coefficient due to non-equilibrium strain or temperature. As the material relaxes back to equilibrium, no light is diffracted from the probe beam. The timescale associated with this relaxation can

be related to the thermal diffusivity of the material. This diffraction signal, heterodyned with a "reference" beam, is captured by a photoreceiver and recorded by an oscilloscope. We can then fit this signal decay to extract the associated thermal diffusivity.

5.2 Comparison to Other Thermal Spectroscopy Techniques

5.2.1 Motivation

Traditionally, thermocouples have been used to measure the thermal conductivity of bulk materials. When measuring the thermal conductivity of a set of materials in series (i.e., a stack of films), the highest thermal resistance will dominate the overall resistance of the bulk. If the layer of interest is not the highest thermal resistance then accurately extracting the thermal conductivity using thermocouples of the layer is difficult or impossible. For example, if 300 nm of thermally grown silica is on the surface of a 1 mm single crystal, the silica only accounts for $\sim 1 \times 10^{-6}$ of the total resistance of the stack. The thermal conductivity of this silica layer cannot be measured with conventional methods. Moreover, the thermal boundary conductance between two dissimilar layers is also inaccessible.

As thin films are common in electronics and energy conversion devices, quantifying their thermal properties is important to thermal management and thermal engineering. Also, at the nanoscale, the thermal boundary conductance is a significant source of resistance. Techniques that can measure such small resistances, without introducing a contact to avoid damage or influence of the thermal properties, are required.

5.2.2 Thermoreflectance Techniques

Laser-based techniques that use the property of thermoreflectance, or the change in reflectance of a material due to a temperature change, have become popular in modern thermal spectroscopy. There are two major flavors of thermoreflectance techniques: time-domain thermoreflectance spectroscopy (TDTR)[95, 96, 97] and frequency-domain thermoreflectance spectroscopy (FDTR)[98, 99]. Both techniques use a "pump" laser to heat the sample periodically and a "probe" laser that reflects based on changes of the temperature of the surface. Typically, a thin metal layer called a transducer is deposited on the surface either through sputtering or evaporation. The pump laser frequency is chosen for high absorbance in the metal and the probe laser frequency is chosen for a high thermoreflectance value for the metal. The pump and probe beams are focused concentrically onto the transducer to a spot size of a few to tens of microns.

In TDTR the lasers are pulsed. The pump laser thermally excites the surface and the probe laser reflects off the surface with a time delay. The probe laser's amplitude is recorded and it changes proportionally to the temperature rise in the surface. By sampling different delays a profile of the probe response with changing time delay can be built. Modulation of the pump laser intensity by a sine wave at a lower frequency than the probe sampling rate can be used for lock-in detection to improve signal-to-noise ratio.

FDTR uses continuous wave lasers. The pump laser is intensity modulated by a sine wave and heats the sample periodically. The probe laser is unmodulated but upon reflecting off the surface gains an intensity modulation of the same frequency of the pump modulation as the thermoreflectance of the surface changes sinusoidally. The amplitudes and phases of the two beams are recorded using a lock-in amplifier, and the phase difference (a.k.a. phase-lag) between the two beams is recorded.

In both setups, the thermal penetration depth of the thermal signal is shallow, pro-

ducing a high sensitivity to the thermal characteristics of the surface. The profile of the penetration depth varies between semi-spherical to flat, depending on spot size and modulation frequency. This results in a large dependence on the cross-plane thermal diffusivity and little dependence on the in-plane thermal diffusivity. The relations of probe response with time delay for TDTR and the phase lag with modulation frequency for FDTR, can be fit to an analytical model of the heat diffusion equation for a layered system heating by Gaussian lasers[100]. The thicknesses of all the layers, the thermal diffusivity of the non-target layers, and the volumetric heat capacity of the target layer must all be known to fit.

5.2.3 Comparison

The primary difference between TG and TDTR/FDTR is that TG is sensitive to in-plane thermal transport and TDTR/FDTR is sensitive to cross-plane thermal transport. This is due to the spatial variation of the temperature profiles. In TG, the heat is deposited in a one-dimensional sinusoid across the surface of the sample, leading to a strong driving gradient in the in-plane direction. In TDTR/FDTR, the heat is deposited in a planar profile at the surface, creating a temperature gradient towards the back of the sample in the cross-plane direction. It is the spatial depositions of heat that creates the different sensitivities.

There are other considerations that differentiate the techniques. In TG, the probe spot size is on the order of hundreds of microns, limiting the size of regions or samples that can be measured compared to TDTR/FDTR's few to tens of microns resolution. Also, in the transmission TG the sample must be semi-transparent to let the light transmit through to the detector. In TDTR/FDTR, a metal layer is typically applied to obtain the desired thermoreflectance effect. This introduces complexity as the deposition adds another layer

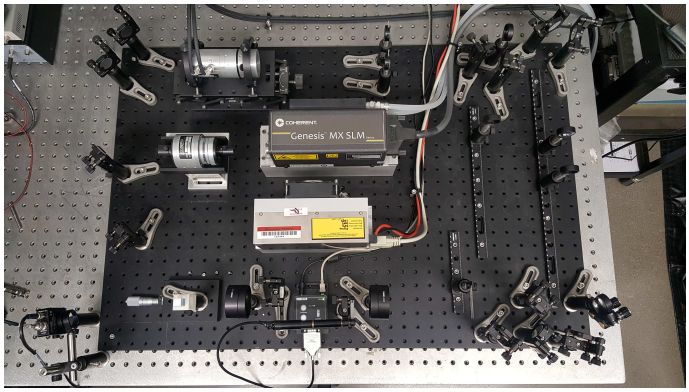

Figure 5.1: The layout of the TG experiment.

to consider. Moreover, the sample is heated during the deposition of metal, something that might be undesirable. Also, the transducer layer can influence the dynamics of the material, especially in thin membranes. Depending on the second layer, the metal might diffuse into the sample changing the thermal properties of the following layer. The interface conductance between the metal and the subsequent layer adds a possible unknown to the analytical fit, and measurement of the thickness and thermal conductivity of the metal must be performed. With TG, there is no need for a transducer layer as it operates by changes in the optical properties of the material of interest. Moreover, with TG, only the spacing of the grating at the sample is needed to extract the thermal diffusivity if there is only one material of interest.

5.3 Setup

5.3.1 Optics and Optomechanics

In Fig. 5.1 is the optomechanical portion of our TG experiment and in Fig. 5.2 is a enumerated schematic of the critical components. Central to the TG experiment is two lasers, a pulsed "pump" laser (Fig. 5.2[1]) and a continuous wave "probe" laser (Fig. 5.2[2]). In

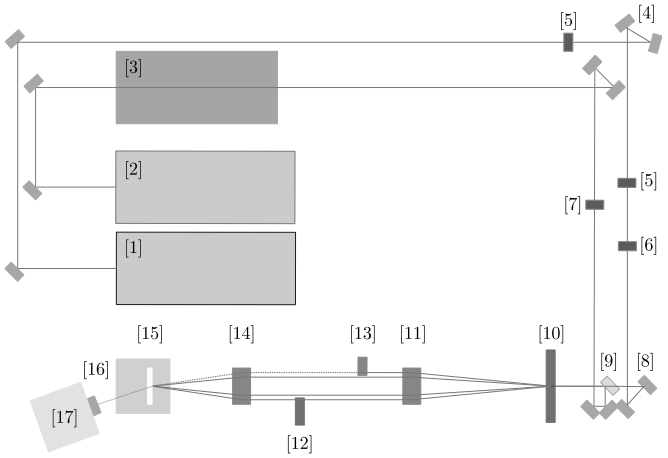

Figure 5.2: A schematic of the TG setup.

our setup we used a Bright Solutions Wedge-XF pulse laser at 532 nm which has a variable repetition rate of single-shot to 100 kHz, a pulse width of 350 ps, and a maximum power of 800 mW. Our probe laser is a continuous wave Coherent MX SLM at 514 nm with a maximum power of 500 mW.

Since the decay time of the signal is on the order of microseconds, we try to minimize heating of the signal by only lasing the probe beam during the relevant time period. This is accomplished by optically chopping the beam through the use of an electro-optic modulator (EOM). We use a ConOptics Model 350-50 electro-optic modulator (EOM) to chop the signal(Fig. 5.2[3]).

The two beams are then sent through a series of beam shaping and focusing lenses. To align with the lenses, we use two mirrors (Fig. 5.2[4]) to turn the corner. This is done as we need one mirror to grant us the degree of freedom of the angular dependence and a second mirror to allow us to control the linear position of the beam origin. The combination allows us to send our beam in a straight line without physically moving the position of the mirrors, just by manipulating the angle adjustment knobs. The pump beam is first shaped by two convex lenses (Fig. 5.2[5]) of focal lengths 300 mm and 40 mm. These lenses allow us to reduce the beam width of the pump. This is done as the final spot size of the pump

must be larger than the probe, and the spot size is inversely proportional to the beam width. The pump is then focused by a 500 mm convex lens (Fig. 5.2[6]) to the diffraction grating (Fig. 5.2[10]). The probe is also focused by a 500 mm convex lens (Fig. 5.2[7]) without any previous beam shaping to the same location.

To make alignment easier, the pump is turned to the final beam path by use of a gimbal mirror (Fig. 5.2[8]). The gimbal mirror pivots around the center point of the mirror face, whereas the normal mirror mounts pivot on one corner. This is desirable as adjustments in the vertical and horizontal axis couple less to each other. As such, the gimbal mirror is primarily used for the final fine alignment of the experiment. The probe is redirected by a dichroic mirror (Fig. 5.2[9]). This dichroic mirror is transparent to the 532 nm pump beam wavelength which allows us to combine the beams. Note that the dichroic mirror is operational at an incident angle of 45±1°.

At the dichroic mirror, the two beams are not collinear nor concentric. This is so that the probe beam can have a downward angle while traveling towards the diffraction grating (Fig. 5.2[10]). The diffraction grating is a glass slide that has periodic square wells 565 nm in depth cut into the surface. The 565 nm depth is specific to the pump wavelength of 532 nm. The grating diffracts by periodically changing the phase lag of the light passing through it and is therefore a phase diffraction grating. The square cuts are spaced apart with variable grating periods ranging from 2.2 μm to 260 μm. This spacing changes the diffraction angle as well as the final grating spacing at the sample surface. Here, at the diffraction grating, the pump and probe beams are focused and concentric, which is necessary for the telescopic effect of the achromatic lenses.

First, a 150 mm focal length achromatic lens (Fig. 5.2[11]) redirects the four beams (i.e., first orders of the pump and first orders of the probe) parallel to each other. The downward angle probe beams are now also parallel to the bench surface, but are lower in

position than the pump beams. This allows us to interact with the probe beams without interfering with the pump beams. First, the left probe beam is sent through a glass window (Fig. 5.2[12]) whose angle is controlled by a Thorlabs Z812 Motorized Actuator. The glass window imparts some arbitrary phase difference into the left probe beam relative to the right probe beam. By changing the angle of the glass window we change the path length and thereby phase imparted on the beam. This allows control of the phase difference between the two probe beams. The right probe beam passes through a 2.0 neutral density filter that attenuates the intensity of the light, we shall call this the "reference" beam. This helps avoid saturation of the photoreceiver (Fig. 5.2[17]). The pump laser travels unimpeded to as 75 mm achromatic lens (Fig. 5.2[14]) that focuses the pump and probe beams onto a sample.

The pump beams focus onto the sample with a spot size of $\sim$500 μm in diameter (Fig. 5.2[15]). The two beam interfere and produce a sinusoidal interference pattern. This induces a periodic strain and a periodic heating if the sample is not transparent. The left probe beam passes through the irradiated region and diffracts based on the changes in strain and temperature. The reference beam, which is naturally collinear with the diffracted probe beam serves as a heterodyne, in part, to increase the signal amplitude of the diffracted probe beam. Our TG is setup for transmission geometry, where the heterodyned beam transmits through the sample. A reflection setup for TG is possible for materials that are opaque, however such as setup is beyond the scope of this thesis. The heterodyned beam is sent through a Thorlabs bandpass filter of 514.5 $\pm$3 nm (Fig. 5.2[16]) to filter out any pump light and is recorded by a photoreceiver (Fig. 5.2[17]). The startup procedure to perform the experiment is describe in detail in Appendix B.1.

5.3.2 Electronics

Electronically, the biggest challenge is timing of the lasers and of the recording of the data. The probe laser is water cooled using a thermoelectric cooler and its power is manually set in units of milliwatts. The pump laser is air cooled with a heat sink and fan, and its power is manually set by a "line voltage," which is a voltage between 0 and 5 V that is an unspecified non-linear function of the actual power of the laser. Typically, the probe laser is operated at a power between 200-300 mW and the pump laser is operated between 80-100% line voltage.

To initialize the timing, a Keithley 3390 50 MHz Arbitrary Waveform Generator creates a unipolar square wave with a frequency of 1 kHz, a voltage of 1.247 V, and a duty cycle of 20%. This is sent to a ConOptics Model 302 RM amplifier which drives the EOM. The voltage of 1.247 V is specific to the probe laser wavelength of 514 nm.

The waveform generator sends a 1.5 V square wave from the sync output to a BNC Model 7010 Digital Delay Generator. The delay generator is used to trigger both the pump laser and the recording of data. A 3 V delta signal is sent to the pump trigger to fire the laser. This is done 180 μs after the probe laser has been allowed to pass by the opening of the EOM. Since the probe signal will fluctuate after the EOM has opened the delay allows the noise to reduce before the pump fires. This leaves 20 μs of time to record the signal. A Tektronix TDS 794D Four Channel Digital Phosphor Oscilloscope is used to record the signal. The oscilloscope is triggered by the delay generator through the use of a gate signal output. This gate signal is a 1 V square wave recorded in the second channel of the oscilloscope. The fall of the gate signal occurs at 180 μs after the EOM opens the probe laser, and at the same time as the pump laser fires, triggers the recording by the oscilloscope.

The oscilloscope records 250,000 samples at a sampling rate of 2 GHz. This is done

while averaging every 100,000 samples for three to six minutes. The signal is recorded by a Thorlabs PDA10A Si Amplified detector. It is rated for light of wavelengths between 200 and 1,100 nm and has a bandwidth of 150 MHz. This photodetector is suitable for thermal decays on the order of milliseconds. For detection of acoustic waves or short thermal decays on the order of nanoseconds a AC-coupled high-speed photoreceiver can be used. Such an AC-coupled photoreceiver, however, is inappropriate for longer thermal signals as it cannot capture the low-frequency terms of the exponential decay.

5.4 Theory of Operation

When the pump laser encounters the sample there are two effects: acoustic strain termed impulsive stimulated Brillouin scattering (ISBS) and thermal strain termed impulsive strained thermal scattering (ISTS). ISBS occurs even in completely transparent materials and is caused by stress from electrostriction, i.e., the stress induced in dielectrics by an electric field. ISTS, which is of primary concern for this thesis, is created by optical absorption of light and creates both thermal strain and acoustic waves.

The complex index of refraction, $\underline{\mathcal{N}}$, of a material is,

$$\underline{\mathcal{N}} = \mathcal{N} + i\mathcal{K}, \tag{5.1}$$

where the $\mathcal{N}$ is the real term and $\mathcal{K}$ is the imaginary term. The real term is the ratio speed of light in a vacuum to the phase velocity of light in a material and controls the angle in Snell's law. This term changes spatially due to both ISBS and ISTS. Spatial variation in the real index of refraction produces a phase modulated diffraction grating, where the diffraction grating is created by the periodic change in phase of the light. The imaginary index of refraction, or the extinction coefficient, is only modulated by ISTS. As it relates

to the attenuation of of light it is only present in opaque or semi-transparent materials. The laser thereby produces both an amplitude diffraction grating, where the difference in periodic intensity of light is the basis of the diffraction grating from the thermal dependency of $\mathcal{K}$, and a phase modulated grating from the acoustic waves produced by the shock of thermal expansion or electrostriction.

These effects can be separated by altering the phase adjust on the probe beam. This changes the relative phases between the two probe beams and therefore the intensity profile at the sample. This enables selection of the phase modulation when the probe and reference beams' phases are either $-\pi/2$ or $\pi/2$ relative to each other, or the selection of amplitude modulation when the probe and reference beams' phases are either 0 or π relative to each other. The theory of heterodyne detection is described in more detail in Appendix B.2.

Under the approximations that the reference beam intensity is much greater than the diffracted beam intensity and that the heating is uniform in the cross-plane (i.e., z), direction the temperature response of the surface is[94],

$$T(z=0,x,t) = \frac{A}{\eta\sqrt{\pi}} \left(\alpha_z t\right)^{-1/2} \cos\left(q_{\mathrm{D}} x\right) \exp\left(-\alpha_x q_{\mathrm{D}}^2 t\right), \tag{5.2}$$

where A is the amplitude of the signal, η is the inverse of the penetration depth of the temperature into the surface, q is the grating wavenumber, and α is the thermal diffusivity. The amplitude is a practically indeterminable value due to unknown translations and losses in the recording of the signal. TG is insensitive to the cross-plane (i.e., z-direction) thermal diffusivity as it is indistinguishable from the arbitrary amplitude. The in-plane (i.e., x-direction) thermal diffusivity determines the rate of the exponential decay which can be extracted through fitting.

5.5 Benchmarking

5.5.1 Water Sample

We benchmark our TG setup by measuring the thermal diffusivity of water. The water is contained in a Thorlabs fused-UV quartz 700 μL micro cuvette with a path length of 2 mm. The dye malachite green, 4-[4-(Dimethylamino)phenyl](phenyl)methylidene-N,N-dimethylcyclohexa-2,5-dien-1-iminium chloride, is added to the water to absorb and attenuate the light passing through the water. Importantly, the dye diffuses uniformly through the water and acts as a source of volumetric heating when irradiated.

A program scans over the phase adjust angles in small increments. Seven pairs of π and 0 phase difference traces are identified from the phase adjust scan. The 0 phase difference trace is subtracted from the π phase trace to increase the signal.

Using our fitting procedure described in Sec. 5.5.2, we measure a thermal diffusivity of 0.144 m^2/s with a 95% confidence interval from our seven pairs of phase angles of 0.003 m^2/s at an ambient temperature of 25 °C. The reference value is 0.145 W/m^2 at 25 °C[2], with our measurement lying within 1% and with a 95% confidence interval of 2%.[1]

5.5.2 Signal Fitting

We use a diffraction grating spacing of 6 μm. Theoretically, the diffraction grating spacing at the sample should be 3 μm. This is because the ratio of the achromatic lenses' focal lengths is 2:1, which should result in a spot size that is halved at the sample. We measured the spot size at the diffraction grating and at the focal point, where the sample rests, with the knife-edge technique.

A razor blade is attached to a Sutter Instruments MPC-200 micromanipulator with

[1]The temperature rise due to the heating by the laser was not quantified. An increase in temperature at 25 °C would increase the thermal diffusivity.

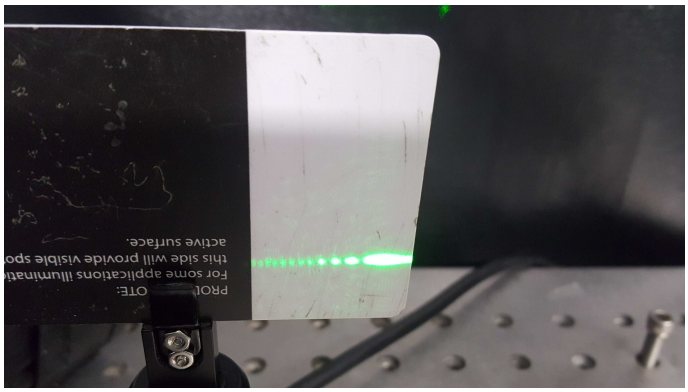

Figure 5.3: Diffraction of the beam at the sample by the straight edge. The beam was allowed to travel past the photodiode and diverge so that it would be visible to the naked eye.

a minimum resolution of 1/16 μm. The blade is moved into the beam while the beam intensity is recorded using a photodiode. As the beam profile is Gaussian, the resulting intensity profile versus displacement is an error function. This function is linearized and fit to extract the spot size. We measure the spot size at the diffraction grating to be 2120 μm and the spot size at the sample to be 570 μm. This is a ratio of 3.7. We suspect that the ratio is affected by divergence of the beam after the diffraction grating. Since the distance between the diffraction grating and the first achromatic lens is less than the distance between the two achromatic lenses, and the spot size is inversely proportional to the beam width at the (second achromatic) lens, this is consistent with our hypothesis.

Moreover, there is difficulty in measuring the spot size at the sample due to diffraction of the laser beam from the straight edge as seen in Fig. 5.3. The diffraction displaces light off the diode. Also, even for a fixed power, changes in the area of irradiation on a photodiode can change the voltage signal. As such, the ratio is only a rough estimate of the expected reduction of spot size.

The first step to fitting the signal is to set the baseline of the signal to zero. This is done by averaging the signal amplitude before the trigger of the pump and normalizing the trace by this value. In Eq. (5.3) the theoretical signal diverges at $t = 0$ from the $\sqrt{t}$ term.

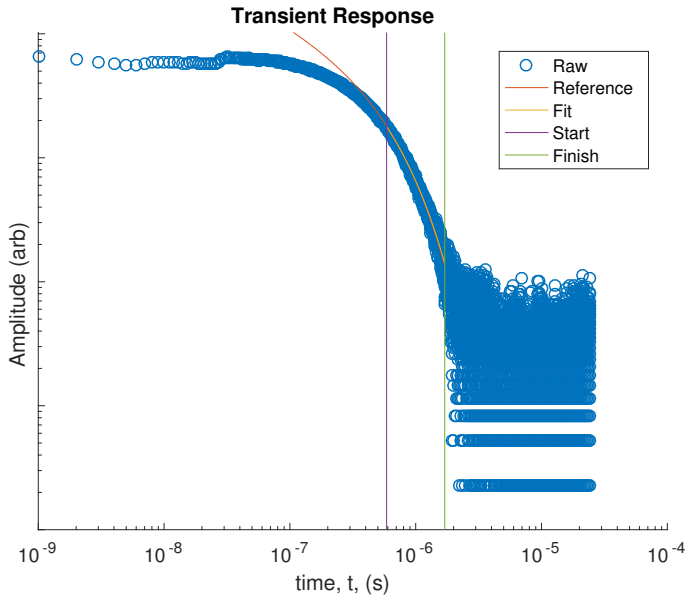

Figure 5.4: A log-log plot of the raw signal amplitude versus time. The vertical lines (purple and green) indicate the limits of the data that is included in the fit. The red line is the decay for the reference value. The yellow line is the fitted line and the blue circles are the raw data points.

This is unphysical and is a result of our approximation that the heating is uniform in the cross-plane direction. The difference between the two has been ameliorated by starting the fit of the signal at some time after the initial pump lase[94]. The amount of time to wait is left as a choice by the user and an exact timing is unspecified. Also, the signal decays to zero but in the experiment there is some finite noise floor that will be reached. We propose a methodology by which to fit the data for the thermal diffusivity.

When considering Eq. (5.3), we note that the terms excluding the square root and decaying exponential can be absorbed by the amplitude. Moreover, the cross-plane thermal diffusivity, α_z, can be absorbed into the amplitude and we can ignore the spatial dependence. Thus the equation we fit is[94]

$$T(t) = A\sqrt{t}\exp\left(-\alpha_x q_{\mathrm{D}}^2 t\right). \tag{5.3}$$

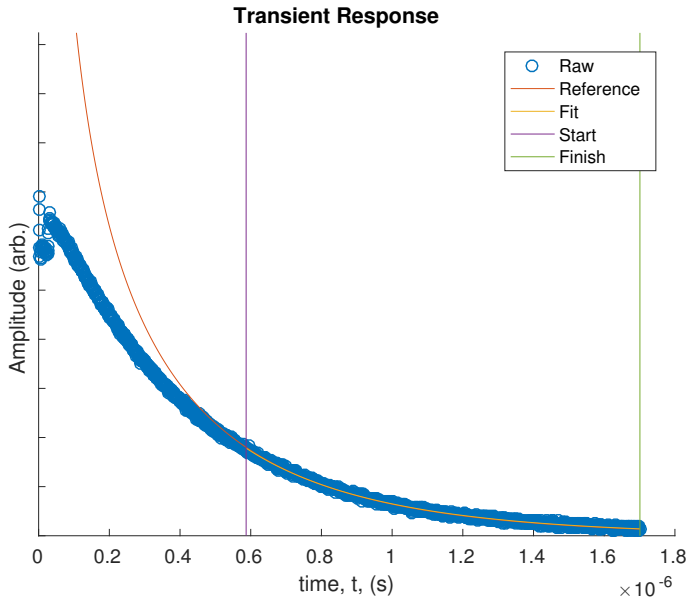

Figure 5.5: A linear plot of the raw signal amplitude versus time. The vertical lines (purple and green) indicate the limits of the data that is included in the fit. The red line is the decay for the reference value. The yellow line is the fitted line and the blue circles are the raw data points.

The amplitude A, and in-plane thermal diffusivity, α_x, can be fit using a nonlinear regression method. Since we know that the grating wavenumber q is not correctly represented by the theoretical reduction from the achromatic lens focus length ratio, we also fit to this quantity. For each phase-pair fit we obtain an amplitude, in-plane thermal diffusivity, and grating wavevector. However, it is unphysical that there should be any variation in the grating wavevector. To correct this, we average the grating wavevector from the seven phase-pairs and then refit only the amplitude and in-plane thermal diffusivity using the averaged q. We find the fitted grating wavevector is 1.80μm, 10% larger than measured by the knife edge technique.

To determine the maximum time limit of our fit we need to identify the noise floor. In Fig. 5.4, we plot the signal amplitude versus time on a log-log scale. We can easily identify the noise floor as the curve disperses and flattens with increasing time. The upper limit of the fit time is indicated by a vertical green line in Fig. 5.4 that is chosen to avoid the noise

floor. Also we observe the limitation of the precision of the oscilloscope by the horizontal bands starting at 2 μs.

To determine the start time, we fit the signal decay for multiple start times. For each fit we calculate a mean squared error (MSE), which is the average of the square of the difference between the fitted line and the data points. We identify the start time that reduces this error. Note that the this fitting procedure does not require any knowledge about the material that is measured and does not require any guess-work by the user. The best fit for one of the phase-pair traces is plotted in Fig. 5.5. We note that the theoretical decay (red line) using the reference thermal diffusivity of water quickly diverges before the start of the fitted data section. The fitted decay (yellow line) is coincidental with the theoretical decay between the limits of the fitting.

5.6 Summary

The TG techniques allows for measurement of in-plane thermal diffusivity. This provides an alternative to the cross-plane sensitive thermoreflectance spectroscopy techniques. In contrast to TDTR/FDTR, it requires no transducer layer and operates by changes in the complex refractive index of the material of interest. This allows for measurement of free standing membranes which thermal properties could be affected by the addition of a metal layer.

We specify a more rigorous technique by which to fit the data by identifying the noise floor and performing an error minimization technique to account for the approximation of a uniform cross-plane heating profile. This reduces the ambiguity in the measured values and avoids user intervention that could influence the results.

Confinement

6.1 Introduction

In Chapter 4, we considered the effect of phonon-boundary scattering from nanostructuring on the in-plane thermal conductivity of silicon. The formalisms employed, however, approximated the additional scattering as a modification of the bulk phonon properties. When the dimensions are on the order of the phonons' wavelength this approximation breaks down as the HLD properties (Sec. 2.2.1) calculated for a three-dimensional periodic crystal are no longer valid. It is in this case we must consider confinement effects, that is, the basic phonon properties are modified to the extent that they are no longer simply perturbed from bulk. For silicon, Jain et al. found the free path sampling technique did not agree with experimental measurements in silicon thin films with thicknesses less than 100 μm[80]. Such dimensions are commonplace in nanofabrication in electronic devices. This discrepancy is not well described in both how the phonon transport properties change as well as how the modes themselves change at these dimensions.

There have been previous studies of thermal transport in the confinement regime. Gomes used MD to study silicon with the Tersoff potential and found that the thermal conductivity varied linearly due to the ballistic transport in thin films[101]. Heino calculated the phonon dispersion of silicon from MD as well as the in-plane thermal conductivity[102]. They found a reduction of the maximum phonon frequency as the thickness of the films decreased accompanied by a reduction in thermal conductivity. Turney et al. predicted the in-plane phonon thermal conductivities of argon and silicon thin films from ALD[103]. They modified the lattice dynamics techniques by only considering wavelengths that fit

inside the thin films considered but still employed a three-dimensional traveling wave basis for the calculations. They observed an increase in the thermal conductivity of argon below 4.3 nm and contribute this effect to the models' inability to accurately represent the density of states of a free film. Wang and Haung studied first-principles based silicon by iterating upon the technique used by Turney et al[104]. In addition to restricting the wavelengths that could fit inside the film, they also modified the ALD technique to restrict the phase space that these modes could also scatter with.

When the confinement regime is studied with MD the true dynamics of the film (albeit restricted to classical) are without approximation, however, MD fails to provide the modal detail to elucidate the modification of the phonon properties. The lattice dynamics based methods are approximative as they are calculated on a bulk (i.e., periodic in three-dimensions) crystal. This type of approach ignores effects such as varying force constants and unit cell size throughout the film. Here we use two techniques to resolve where the breakdown in the modification of the bulk properties begins and how the properties break down in argon modeled with the LJ potential. This is accomplished by using the free path sampling technique to modify the bulk phonon properties calculated by HLD and ALD to predict the thermal conductivity of a thick film down to a single atomic layer. Then we perform lattice dynamics but reduce the dimensionality of our problem by considering a unit cell that spans the entire thickness of our film, thereby limiting the periodicity of the phonons to two-dimensions. This reduced dimensionality approach calculates the dynamics of the phonons in thin films without any approximations to account for the confinement effects.

The rest of this chapter is organized as follows. In Sec. 6.2 we describe the computational details of our free path sampling and lattice dynamics methods. We then present and compare in Sec. 6.3 the in-plane conductivities and phonon properties for LJ argon from

both free path sampling and reduced dimensionality lattice dynamics. Our conclusions are then presented in Sec. 6.4.

6.2 Computational Details

6.2.1 Lennard-Jones Argon

We consider argon at a temperature of 20 K modeled by the two-body LJ potential (Eq. (3.1)). The potential parameters of m, ϵ_{LJ}, σ_{LJ}, and cutoff radius are taken as the same in Sec. 3.2.1. The four-atom conventional unit cell is considered in this study to allow for the construction of the thin films. As mentioned in the introduction, the atomic positions throughout the thin films can vary based on position. Also the in-plane and cross-plane lattice constants can differ in a thin film due to the anisotropy of the structure. For the calculation of heat capacity, the cross-plane lattice constants are taken as if the layer of argon were to exist in a bulk material as is common with two-dimensional materials. To find the atomic positions and lattice constants in our thin film, we use LAMMPS to relax the atomic positions and box size in the in-plane direction[69]. Note that by doing this we are not performing quasiharmonic HLD, as the positions and lattice constants are found for a temperature of zero Kelvin.

6.2.2 Lattice Dynamics

To find the bulk phonon properties for use in free path sampling, we perform HLD and ALD on the zero temperature lattice constant of $a = 5.296$ Å. Here we consider classical statistics where $c_{\mathrm{ph}} = k_{\mathrm{B}}B$. The force constants are calculated by finite displacement of a supercell in LAMMPS. The harmonic force constants are found by taking displacements up to third-nearest-neighbor, while the anharmonic force constants are found by

taking displacements up to first-nearest-neighbor. Phonon properties are calculated on a Monkhorst-Pack wavevector grid of $24 \times 24 \times 24$. Increasing the grid density to $26 \times 26 \times 26$ results in a decrease of thermal conductivity by less than 0.8%.

We consider thin films where the number of cross-plane unit cells, H, ranges from one to six. The minimized atomic positions and lattice constants are taken from LAMMPS. The harmonic and anharmonic force constant cutoffs are the same as in bulk case. We reduce the dimensionality of the lattice dynamics problem by eliminating the cross-plane direction from consideration as the film is aperiodic in that direction. Note the atoms are still considered to displace in all three directions; it is the phonons that are restricted to two-dimensions. Phonon properties are calculated on a Monkhorst-Pack wavevector grid of 24×24. Increasing the grid density to 26×26 results in a decrease of thermal conductivity by less than 0.2% for all films considered.

6.2.3 Free Path Sampling

The free path sampling was calculated for thin films thicknesses of 0.5 nm to 100 nm using the bulk properties from Sec. 6.2.2. Each of the 165,888 phonon modes was sampled randomly through the thickness 10,000 times with ten initial seeds. The 95% confidence interval calculated from the ten seeds is less than 1×10^{-4} W/m-K for all thicknesses. The in-plane directions were simulated as periodic to emulate a film infinite in extent.

6.3 Results

We first examine the in-plane thermal conductivities predicted by free path sampling and the reduced dimensionality HLD and ALD calculations versus film thickness in Fig. 6.1. We observe that the FPS and lattice dynamics calculations are very similar at a thickness of 3.2 nm, but the explicitly calculated thermal conductivity quickly diverges away from

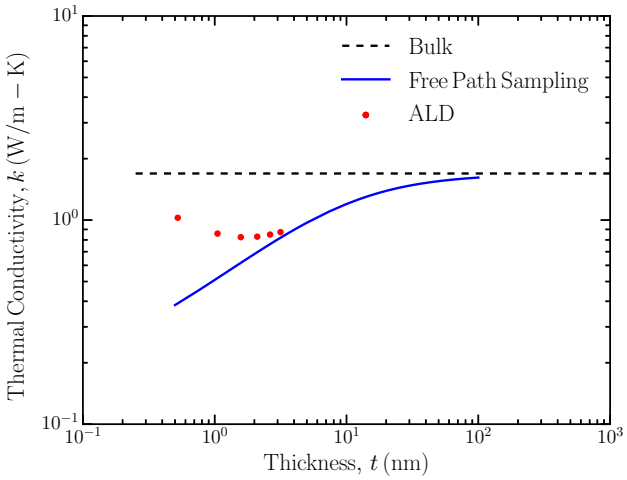

Figure 6.1: Thermal conductivities predicted by free path sampling and HLD/ALD for different thicknesses on a log-log plot.

the FPS. We see that this discrepancy occurs in argon at a much thinner film thickness than 100 nm in silicon from Jain et al. observations[80]. Turney et al. predicted a very similar thermal conductivity trend with an inflection at 4.3 nm from their modified lattice dynamics model[103]. They reasoned that the inflection and subsequent disagreement with their Green-Kubo results was due to a failure of their model to predict the correct density of states. Here we find that the inflection exists even when accounting for the proper density of states as we have not made the bulk like density of states assumption that they did.

To elucidate the cause of this increase in thermal conductivity, we plot the dispersion for bulk argon and one unit cell thick argon in Fig. 6.2. Here we observe a reduction in frequency and therefore sound speed and group velocity in the monolayer as compared to bulk. We observe the monolayer's out-of-plane acoustic branch has a quadratic dispersion, similar to what is observed in graphene. In graphene, this manifests due to strong asymmetry in the in-plane force constants and the out-of-plane restoring force constants. It is somewhat surprising to see this in argon due to the dichotomy of argon as a soft and low

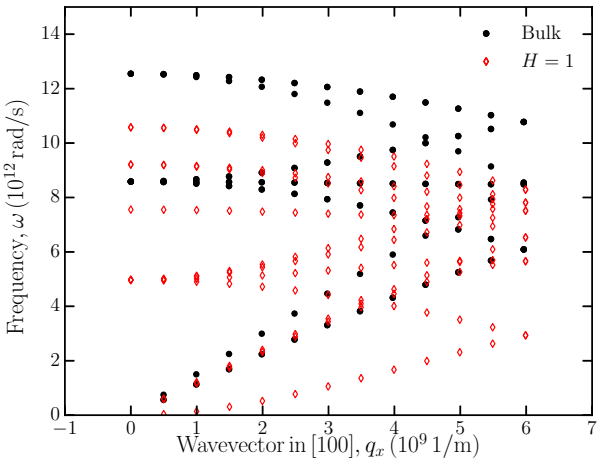

Figure 6.2: Dispersion of bulk and monolayer argon in the [100]-direction.

thermal conductivity material and graphene as stiff and high thermal conductivity material. The discrepancy in the dispersion relation represents a failure of the FPS to account for confinement effects, however, the decrease in group velocity should only ameliorate the underprediction of thermal conductivity.

We next consider the lifetimes calculated for the monolayer and by the FPS technique for a thickness, $t = 0.5$ nm in Fig. 6.3. The FPS technique modifies the mean free paths, but implicit in this calculation is that the lifetimes are the fundamental quantities that are modified by the additional scattering rate induced by the boundaries. It is therefore useful to compare the calculated lifetimes between the two methods. We observe in Fig. 6.3 in both the FPS and lattice dynamics calculations a phonon-phonon $1/\omega^2$ scaling of lifetimes in the low-frequency range. Interestingly, we observe some greater than $1/\omega^2$ scalings in the mid-frequency range of the lifetimes from the lattice dynamics method. The lifetimes calculated by the lattice dynamics techniques are lower that that of the FPS technique except for in the very low-frequency range. These modes exist due to the quadratic branch and the lower sound speed of the longitudinal and transverse acoustic branches. Although there are a couple of lifetime points above that predicted by FPS, it is not enough to

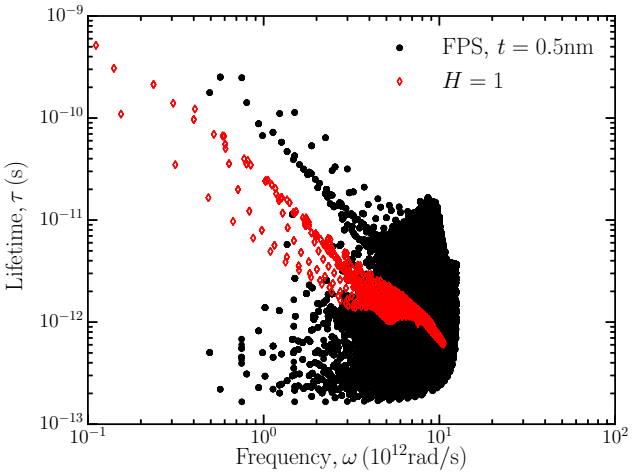

Figure 6.3: Lifetimes of the FPS at a thickness of 0.5 nm and of the monolayer versus frequency. The lifetimes are back-calculated from the mean free paths by use of the bulk group velocities.

explain our thermal conductivity discrepancy.

We have determined that the group velocities and lifetimes are suppressed in the reduced dimensionality calculation compared to that predicted by FPS. Also, the heat capacity of each mode is equivalent as we are using classical statistics. This means the phonon transport properties calculated by lattice dynamics are less than FPS on a frequency basis. The apparent suppression of the phonon transport properties infers that the density of states is modified such that there are more phonon modes in the low-frequency range, as these phonons have higher thermal conductivity than those in the mid- to high-frequency range. In Fig. 6.4 we plot the density of states for the bulk, which is equivalent to that used for FPS, and the single unit cell thick film calculated from reduced dimensionality lattice dynamics. We observe the traditional low-frequency ω^2 trend of the density of states in bulk argon, shown in blue. The single layer argon film, however, exhibits a low-frequency linear trend of the density of states with frequency, due to its reduced dimensionality. This confirms that there are more modes, proportionally, in the low-frequency range for the explicit calculation of the dynamics by reduced dimensionality lattice dynamics compared

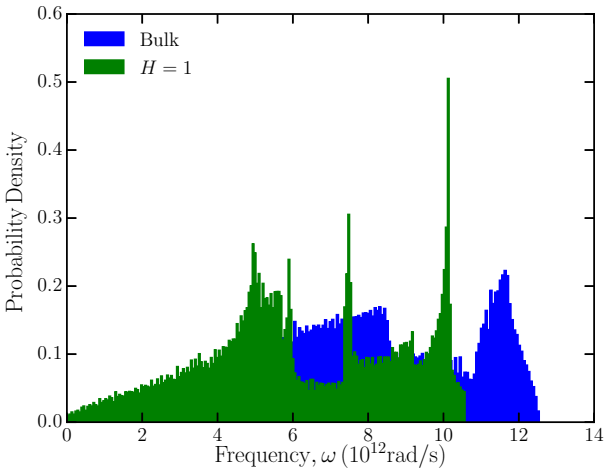

Figure 6.4: The density of states versus frequency of the FPS at a thickness of 0.5 nm and of the monolayer. The area is normalized to one such that the vertical axis is probability density.

to the approximation of FPS using the bulk density of states. Turney et al. observed this density of states trend in an HLD calculation, but reasoned that the failure to account for the change in the density of states was the reason for the increase in the thermal conductivity of argon in very thin films[103]. We find that in our calculations that the density of states is the reason why the thermal conductivity increases at low-frequency, and therefore their increase must be due to some other factor in their approximative modification of ALD.

Turney et al. performed Green-Kubo calculations to calculate the thermal conductivity of thin films of Lennard-Jones argon and found that the thermal conductivity monotonically decreased with decreasing thickness, counter to that calculated from their modified technique. Since our approach required no approximations beyond those typically taken with HLD and ALD, it is unclear why there should be a discrepancy between Green-Kubo and lattice dynamics at this length scale. We showed good agreement between the two techniques previously in Sec. 3.3.1.1. Further investigation is warranted to determine the cause.

6.4 Summary

We investigated the thermal conductivity of confined thin films of Lennard-Jones argon. Using the FPS sampling technique we predicted the thermal conductivity from 0.5 nm to 100 nm. The FPS technique predicted a monotonic decrease in thermal conductivity with decreasing film thickness. It is known that at very thin film thicknesses perturbative techniques such as FPS fail to capture confinement effects.

Using reduced dimensionality lattice dynamics, we predicted the thermal conductivity of argon films from one to six unit cells thick. We found with decreasing thickness an inflection point at which the thermal conductivity begins to increase. This has been observed before with approximative methods and was considered an artifact of the failure to capture the confined density of states. Here we compare the lifetimes, group velocities, and density of states of the two methods for a one unit cell thick film. We find that the lifetimes and group velocities calculated by reduced dimensionality lattice dynamics are less than those calculated by FPS. It is observed that the density of states, and the proportionally higher number of low-frequency modes is the reason that the lattice dynamics technique predicts a higher thermal conductivity compared to FPS, in contradiction to previous calculations.

Other Completed Work

7.1 Microsecond-Sustained Lasing from Colloidal Quantum Dot Solids

7.1.1 Abstract

Colloidal quantum dots have grown in interest as materials for light amplification and lasing in view of their bright photoluminescence, convenient solution processing and size-controlled spectral tenability. To date, lasing in colloidal quantum dot solids has been limited to the nanosecond temporal regime, curtailing their application in systems that require more sustained emission. Here we find that the chief cause of nanosecond-only operation has been thermal runaway: the combination of rapid heat injection from the pump source, poor heat removal and a highly temperature-dependent threshold. We show microsecond-sustained lasing, achieved by placing ultra-compact colloidal quantum dot films on a thermally conductive substrate, the combination of which minimizes heat accumulation. Specifically, we employ inorganic-halide-capped quantum dots that exhibit high modal gain (1,200 cm^{-1}) and an ultra low amplified spontaneous emission threshold (average peak power of $\sim$50 $kWcm^{-2}$) and rely on an optical structure that dissipates heat while offering minimal modal loss.

7.1.2 Introduction

Colloidal quantum dots (CQDs) have attracted interest in light emission applications because of their high photoluminescence quantum yield[105], size-controlled wavelength ten-

ability across the visible[106] and infrared spectral spectral regimes[107], and convenient processing from the solution phase. They can provide amplified spontaneous emission (ASE) and lasing, but to date sustained only on the femtosecond[108, 109, 110, 111] to nanosecond timescales[112, 113, 114]. This prevents their application when more sustained population inversion is required.

Much prior work has begun from the assumption that Auger recombination is the most important effect that limits CQD lasing[115]. As a result, there has been an intense focus on extending the Auger lifetime using core–shell structures[116]. However, previous works have already seen lasing sustained on the nanosecond timescale, a duration already longer than reported Auger lifetimes[115, 117].

We sought to determine, and then remedy, what had previously curtailed sustained ASE and lasing. One possible mechanism is the effect of temperature beyond nanosecond times. Here a number of effects could work together. Much of the energy of the pump-produced photoexcitation is lost through thermalization and also non-radiative recombination and all such losses contribute to heating of the film. In prior reports, both the CQD film and also the substrates employed have suffered from low thermal conductivity. Given that Auger recombination is highly thermally activated[118], these two effects together could give way to a runaway increase in threshold and loss of ASE once the film temperature has risen due to continued heating over the duration of an extended excitation pulse. Keeping these considerations in mind, we develop ultra-compact CQD films to achieve record-low lasing threshold measured in peak power enabling microsecond-sustained lasing. We conclude with a discussion of the path to continuous-wave lasing and light amplification from CQD solids. [Published in "Microsecond-sustained lasing from colloidal quantum dot solids," M. M. Adachi, F. Fan, D. P. Sellan, S. Hoogland, O. Voznyy, A. J. Houtepen, K. D. Parrish, P. Kanjanaboos, J. A. Malen, and E. H. Sargent. *Nature Communications*, **6**:9694,

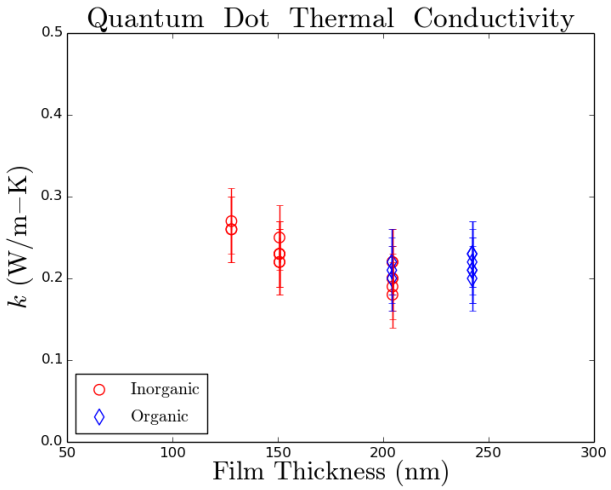

Figure 7.1: Individual thermal conductivity measurements across samples of different thicknesses for organic-ligand and inorganic-halide capped quantum dot films.

(2015)][119].

7.1.3 Contribution

In this work, it was originally hypothesized that the change in the colloidal quantum dot structure could be changed to increase the thermal conductivity. Doing so would then reduce the operating temperature of the film and help avoid Auger recombination that would limit sustained lasing. This was done by removing the organic ligands that were used to passivate the surface and replacing them with inorganic-halides.

We measured the thermal conductivity of thin films of organic-ligand- and inorganic-halide-capped CQDs. These measurements were made with FDTR, a high-frequency contact-less optical laser based technique (Sec. 5.2). FDTR enabled us to avoid destroying the sample and have a high sensitivity to the thin films. The measured thermal conductivities are plotted in Fig. 7.1. We found no significant difference in the thermal conductivities of the organic-ligand- and inorganic-halide-capped CQDs. Due to the greater density of the inorganic-halide-capped CQDs, however, the overall film thickness required for lasing

was decreased and thereby the thermal resistance of the entire film was decreased. This, combined with higher thermal conductivity substrates, allowed for microsecond-sustained lasing using the CQD films.

7.2 Modifying the Thermal Conductivity of Small Molecule Organic Semiconductor Thin Films with Metal Nanoparticles

7.2.1 Abstract

Thermal properties of organic semiconductors play a significant role in the performance and lifetime of organic electronic devices, especially for scaled-up large area applications. Here we employ silver nanoparticles (Ag NPs) to modify the thermal conductivity of the small molecule organic semiconductor, dinaphtho[2,3-b:2′,3′-f]thieno[3,2-b]thiophene (DNTT). The differential 3-ω method was used to measure the thermal conductivity of Ag-DNTT hybrid thin films. We find that the thermal conductivity of pure DNTT thin films do not vary with the deposition temperature over a range spanning 24 °C to 80 °C. The thermal conductivity of the Ag-DNTT hybrid thin film initially decreases and then increases when the Ag volume fraction increases from 0% to 32%. By applying the effective medium approximation to fit the experimental results of thermal conductivity, the extracted thermal boundary resistance of the Ag-DNTT interface is $1.14 \pm 0.98 \times 10^{-7}$ m^2-K/W. Finite element simulations of thermal conductivity for realistic film morphologies show good agreement with experimental results and effective medium approximations.

7.2.2 Introduction

With excellent mechanical flexibility, low fabrication cost, and compatibility with large area fabrication, organic semiconductors have become a promising candidate as the next generation of flexible electronics[120, 121, 122, 123, 124, 125, 126, 127]. The rapid development of organic semiconductors, including the synthesis of new materials and the processing of active layers, provides optimal packing and thus higher carrier mobility in organic thin films or single crystal materials[126, 127]. For example, the polycrystal and single crystal forms of 2,9-didecyl-dinaphtho[2,3-b:2′,3′-f]thieno[3,2-b]thiophene have shown a carrier mobility of 8.5 cm^2/V-s[128] and and 11 cm^2/V-s[129], respectively. Increasing carrier mobility will yield larger currents as well as parasitic heating during operation, especially for large area electronics where the device density is high. Generally, the thermal conductivity of organic semiconductors are much lower than traditional inorganic semiconductors and typically have a value below 1 W/(m-K)[130, 131, 132, 133, 134, 135].

The inferior thermal transport properties and susceptibility to high temperatures of organic semiconductors often lead to the degradation of the organic device performance[123, 136, 137]. Chung et al. demonstrated that the increase of operating temperature of organic light emitting diodes would reduce the lifetime[123]. Moreover, it has also been reported that the carrier mobility of planar pentacene field effect transistors decreased one order of magnitude after 20-min exposure to 60 °C under vacuum[136]. For electrically conductive polymers, thermal induced degradation is also equally important. For example, in poly(3,4-ethylenedioxythiophene) (PSS): poly(styrenesulphonate) (PEDOT), it has been shown that continuous heating of the material at 120 °C will cause shrinkage of the PEDOT conductive grains and thus decrease the electrical conductivity of the film[137]. Hence, the capability of organic semiconductors to effectively transport and dissipate heat is critical to the overall performance and lifetime of next generation organic electronics.

Recently, experiments and simulations have been developed to study the thermal conductivity of various organic semiconductors used in solar cells or transistors, such as PCBM[130, 138], P3HT[130], C_{60}[135], and pentacene[131]. These organic semiconductors can be classified as either polymers or small molecules. The former usually have a high sublimation temperature due to their long chains, and thus are mainly prepared by a solution-process method, such as spin-coating. The latter have a lower sublimation temperature, and hence are typically deposited by thermal evaporation under a vacuum environment. Since small molecules are held together by weak van der Waals forces, the quality of small molecule organic thin films formed by thermal evaporation depend strongly on the deposition conditions, such as the growth rate, deposition temperature, or impurity concentration. Weak intermolecular interactions of organic semiconductors suggest the potential to adjust the thermal conductivity of organic thin films, an area which has not been extensively investigated.

Although the modification of the thermal conductivity of organic thin films has not been extensively studied, new work focused on organic thermoelectric materials requires insight to their thermal properties. Recently, Kim et al. reported that a thermoelectric figure of merit (ZT) of about 0.42 could be achieved for organic semiconductors by properly doping poly(styrenesulphonate) into poly(3,4-ethylenedioxythiophene) (PEDOT:PSS) with dimethyl-sulphoxide[139]. With a particular focus on modifying the power factor, tellurium nanowires have also been added into PEDOT:PSS to enhance the power factor by five orders of magnitude in work by Yee et al.[140]. It is however important to point out that most of these organic thermoelectric materials with a reportedly high ZT or power factor are prepared with a polymer based PEDOT:PSS, and thermoelectric studies of small molecule organic semiconductors are very limited. To explore this area our group has recently demonstrated that the electrical conductivity of pentacene thin films can be enhanced

by sandwiching a thin layer of Ag NPs between two pentacene layers. This metal-organic hybrid material can be used as the active layer for thermistors and memory transistors[121, 141, 142]. In support of this approach, Jin et al. embedded Ag NPs into thin copper phthalocyanine films and observed a four-order of magnitude increase in the electrical conductivity for Ag volume fractions exceeding 30%[132]. They also demonstrated that the thermal conductivity showed a decreasing trend when the Ag volume fraction was less than 10% and increased when the Ag volume fraction was higher than 10%. All of these findings suggest that embedding metal nanoparticles into small molecule organic materials is an effective method to adjust the electrical and thermal properties of metal-organic hybrid materials.

In the current work, our focus is to utilize the differential 3-ω method[143, 144] to study the thermal properties of DNTT, which is a novel thienoacene-based organic semiconductor for transistor devices. The sulfur atoms in the DNTT molecules are integrated into hydrocarbons with an acene structure to enhance their stability under ambient air conditions[145, 146, 147, 148]. The 3-ω method has been widely used to measure the thermal conductivity of thin films[143]. A metal wire deposited onto the sample performs as a heater and thermometer at the same time. When the metal wire is driven by an AC current, it periodically heats the sample and its resultant temperature change can be monitored by its resistance. According to the temperature change of thin film sample and reference sample, the thermal conductivity of the thin film can be extracted[144].

We demonstrate that the modification of the cross-plane thermal conductivity (k_{film}) of DNTT thin films can be achieved by employing different volume fractions of Ag NPs. We also investigate the correlation between the k_{film} and the deposition temperature of the DNTT thin films. We observe that even though the DNTT thin films deposited at an elevated temperature increasing from 24 °C to 80 °C have a larger grain size, the

effects of the deposition temperature and subsequent morphological changes on the thermal conductivity are very limited. On the other hand, we observe that the k_{film} of Ag-DNTT hybrid thin films shows a trend of an initial decrease when the Ag volume fraction increases from 0% to 16% then k_{film} increases afterwards to the maximum studied Ag volume fraction of 32%. Then we apply the effective medium approximation to theoretically calculate the thermal conductivity of the hybrid thin films. By comparing the calculated results with the experimental results of thermal conductivity, we are able to further extract the thermal boundary resistance of the Ag-DNTT interface. Finally, the finite element method is applied to simulate the thermal conductivity of hybrid thin films with realistic morphologies and finds good agreement with experimental results. Consequently, the results of this work will provide useful information for engineering the thermal conductivity of small molecule organic thin films and thermal management in organic electronics. [Published in "Modifying the Thermal Conductivity of Small Molecule Organic Semiconductor Thin Films with Metal Nanoparticles," *Scientific Reports*, **5**:16095, (2015)][149].

7.2.3 Contribution

In investigating the Ag-DNTT films, Fig. 7.2, it was unsure if the 3-ω measurement would be sensitive enough to the resistance of the film to measure the thermal conductivity. This is because the 3-ω measurement operates at a lower frequency than FDTR and TDTR, and thereby has a larger penetration depth, reducing sensitivity to the film. We measured the films using FDTR to confirm their thermal conductivity measurements in Fig. 7.3 to make sure they were sensitive to the Ag-DNTT film.

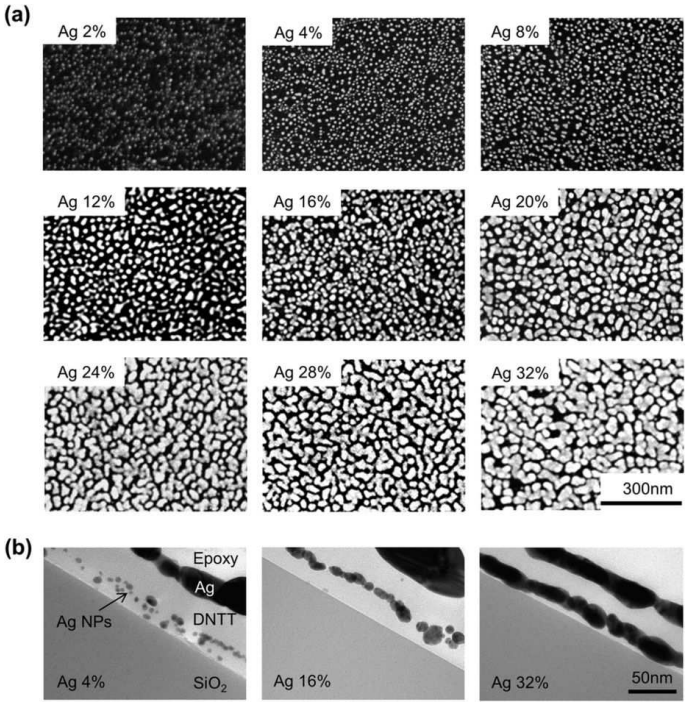

Figure 7.2: (a) Scannign electron microscopy images of Ag layer (bright area) on the bottom DNTT layer (dark area) deposited at 24 °C with Ag volume fraction ranging from 2% to 32 %. (b) Cross-sectional transmission electron microscopy images of thin films deposited at 24 °C with Ag volume fractions of 4%, 16%, and 32%.

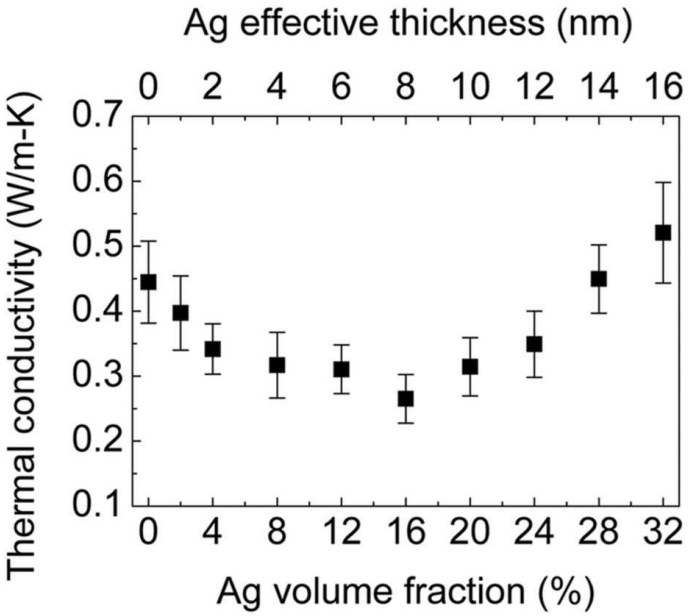

Figure 7.3: Thermal conductivity of Ag-DNTT hybrid thin films deposited at 24 °C with Ag volume fraction ranging from 0% to 32%. The total thickness of the thin film is 50 nm and the effective thickness of the Ag layer is varied from 0 to 16 nm.

Summary and Future Work

8.1 Overview

In this work, we examined how the thermal transport in insulators and semiconductors changes due to external loading or geometrical factors. In Chapter 3, we predicted the thermal conductivities of empirically-modeled argon and first-principles modeled silicon under strain. We observed that argon followed previously predicted thermal conductivity trends and determined that the exponential scaling of the thermal conductivity was due to the exponential scaling of the phonon lifetime and group velocity. Furthermore, we determined the group velocities scaled faster than the lifetimes and that the changes in the dispersion were the primary reason for the thermal conductivity scaling. In silicon, we predicted an invariant thermal conductivity with compressive strain, a result not previously predicted. We hypothesis that this is due to the high-fidelity force constants from density functional theory. Upon examining the phonon transport properties, we observed the lifetimes scaled negatively with compression, opposite of what was observed in argon. Through calculations of the RMS displacement and of the anharmonic potential well energy, we determine that the anharmonic energy increases under compression and thus reduces the lifetimes. This work elucidates that not all materials follow the thermal conductivity scalings with strain which had previously been thought to be universal. The prediction of an invariant thermal conductivity under compression in silicon has been experimentally confirmed by Hohensee et al. using TDTR in a diamond anvil cell[150].

In Chapter 4, we calculated the thermal conductivity of nanoporous silicon crystal films. We investigate the predictions made by three Monte Carlo techniques: free path sampling,

isotropic ray-tracing, and modal ray-tracing. The isotropic ray-tracing reproduces the Casimir limit for nanowires, but also produces unphysical mean free paths. Specifically, phonons that propagate along the axis should have no boundary scattering, but are terminated in isotropic ray-tracing as the average boundary scattering is applied to all modes indiscriminately. This motivated the formulation of modal ray-tracing, where the boundary mean free path is derived from the Landauer formalism without the isotropic assumption. Modal ray-tracing is able to predict more physically realistic phonon mean free paths, indicating the importance of the approximations taken in the formulation of computational techniques. Upon comparison to previous experimentally fabricated nanoporous silicon films, we find that all three techniques are able to reproduce the trend. As the techniques are purely particle based this casts doubt on coherent phonon transport being a factor in the thermal conductivity of these films at room temperature. Finally, we examine a nanoporous silicon film using free path sampling where we modify the geometry to cutoff the line-of-sight. We observe that the trend in thermal conductivity versus porosity changes when the line-of-sight is cutoff, and identify that it is the modes that are cutoff that are responsible for the abrupt change. The line-of-sight effect should be considered when trying to engineer thermal transport in nanostructured materials.

In Chapter 5, we detailed the build of the transient grating spectroscopy experiment. The details of the optics, optomechanical components, and electronics are presented and the practical nuances are elucidated. We compared the experiment to other common thermoreflectance spectroscopy techniques. The biggest difference is the sensitivity to in-plane versus cross-plane thermal transport and other practical considerations are discussed. The benchmark measurement of the thermal diffusivity of water is detailed. Our measurement of the thermal diffusivity of water is within 1% of reference values. The cutoff of the data to fit was found by observation of a log-log plot of the amplitude versus time. We presented

a method by which the quality of the fit, the mean-squared-error, is used to numerically optimize the choice of when to start the fitting of the data to the analytical function. This eliminates previous guess-work as to what range of data to fit, producing more objective data.

In Chapter 6, we investigated the confinement effect and the divergence of the thermal conductivity predictions from free path sampling and reduced dimensionality lattice dynamics on Lennard-Jones argon films. The thermal conductivity predictions for free path sampling are monotonic with thickness while the reduced dimensionality lattice dynamics predict an inflection point in thermal conductivity at 2 nm. We examined the calculated phonon transport properties from both methods. Using classical statistics, the heat capacity is unchanged between the two methods. However, we found the lifetimes and group velocities were higher in free path sampling. Examination of the density of states showed that the linearization of the frequency scaling biased the density of phonon modes to lower, higher thermal conductivity, frequencies. This explanation is in contradiction to what has been previously calculated using lower fidelity methods.

In Chapter 7, we used frequency domain thermoreflectance spectroscopy to measure the thermal conductivity of novel materials. We measured the thermal conductivity of colloidal quantum dots with either organic or inorganic passivated surfaces for use in lasing applications. We determined no significant difference in the thermal conductivities of the films. However, the inorganic passivated films required for lasing were thinner, reducing the overall resistance of the film. This, combined with a higher thermal conductivity substrate enabled microsecond lasing times using colloidal quantum dots. We also measured thin films of the organic semiconductor DNTT with interdispersed silver nanoparticles. An initial decrease followed by increase in the thermal conductivity with the addition of silver nanoparticles was observed due to competing effects between the boundary resistance and

the silver nanoparticle conductance. Moreover, the morphology of the silver nanoparticle DNTT film was found to be dependent on deposition temperature.

8.2 Future Work

8.2.1 Amorphous Membranes

In amorphous materials there exists no long range periodicity. The aperiodicity eliminates the translation symmetry required for phonons. Instead only the assumption that the atoms vibrate about their equilibrium position is valid.

The thermal transport by vibrations in amorphous solids has been classified into three carriers: propagons, diffusons, and locons[151, 152]. Propagons are phonon-like (i.e., plane-wave) vibrations that are delocalized and have a well defined wavelength. Diffusons are delocalized vibrations that do not have a well defined wavelength and instead transfer heat by coupling to other diffusons in space. Locons are localized in space and do not contribute significantly to the thermal conductivity[153]. The diffusons contribution can be predicted through Allen-Feldman theory[151] by calculating the eigenmodes of a disordered solid and quantifying the eigenvector overlap. The propagon contribution can be calculated by estimating the propagon lifetime from normal mode decomposition of a molecular dynamics simulation and assuming the group velocity to be the speed of sound[154]. Importantly, diffusons are always a diffusive process regardless of geometrical constraints, however, the propagons can travel both diffusively and ballistically depending on the geometry.

This allows us to predict the thermal conductivity of nanostructured amorphous materials by use of the free path sampling technique. The diffuson contribution to thermal conductivity can be obtained from previously published data or calculated through the use of Allen-Feldman theory. The propagon bulk contribution can be obtained by assuming

an isotropic dispersion, which is valid for an amorphous material, a group velocity of the sound speed, and calculating the lifetime scaling from normal mode analysis or previously published data. A propagon mean free path can then be constructed and used as input for free path sampling.

8.2.2 Confinement Regime

In Chapter 6, we examined the cross-over between perturbative thermal transport and confinement regime transport. However, previously published data predicted a different trend when the in-plane thermal conductivity is calculated using Green-Kubo in molecular dynamics[103]. Green-Kubo should be performed on these systems to first validate the previous prediction. Furthermore, normal mode analysis, a method by which the lifetimes can be extracted from molecular dynamics simulations, can provide the modal details of the transport in the molecular dynamics simulation. This allows for a direct comparison of the modal properties calculated from reduced dimensionality lattice dynamics and molecular dynamics.

Furthermore, this technique can be applied to a stiffer material: silicon. Since silicon's thermal conductivity is dominated by contributions from low-frequency phonon modes it is unclear whether the same inflection point will be observed. Also, it might be possible to perform the reduced dimensionality lattice dynamics calculations with high-fidelity force constants obtained from density function theory. Such calculations would allow for direct comparison to experimental measurements of the in-plane thermal conductivity. Also the data obtained from these calculations has a strong relevance to the semiconductor industry as such nanometer dimensions are not uncommon.

8.2.3 Phonon Dimensionality Mapping

The question of how the phonon modes transition from a three-dimensional framework to a two-dimensional framework is largely unknown. The concept of confinement and the limitation of the wavelengths of modes is well described, but it is impossible to assign a specific phonon mode from a two-dimensional framework and directly compare it to its supposed three-dimensional counterpart. Such a method, if formulated, would allow for the direct comparison of phonon mode properties such as frequency and mode-shape, as well as phonon transport properties such as lifetime and group velocity, between the two frameworks and develop a scaling for how they change.

Here, I present a possible formulation for the direct mapping phonon modes between dimensionalities. The wavelengths that are allowed are limited to

$$q_z = \frac{2\pi l}{cH}, \tag{8.1}$$

where l is an integer and c is the cross-plane lattice constant. These waves in the cross-plane direction, however, are standing waves instead of traveling waves dues to the free boundary condition at the surfaces of the film. The standing wave wavelengths are contained in the eigenvectors of the phonons solved from reduced dimensionality lattice dynamics. The question is how to extract the q_z from these modes so that they may be mapped back to a three-dimensional representation.

We take inspiration from the normal mode equation Eq. (2.5) in Sec. 2.2.1. The amplitude of an atom is due to the superposition of the motions of the plane-waves. We can think of reformulating this problem where we know the displacement of the atoms (from the eigenvectors), but do not know what wavelength corresponds to these displacements.

I propose the cross-plane wavevector can be solved from,

$$q_z = \underset{q_z \in [-2\pi/c, 2\pi/c] \subset \mathbb{R}}{\operatorname{argmax}} \sum_{\alpha,b,l}^{3,n,N} \int_0^{2\pi} \Re[\exp(-i\omega\,(\mathbf{q},\nu)\,t) e(\substack{\mathfrak{q} \; j \\ \nu \; \alpha})] \exp(iq_z \cdot r_{\circ,z}) dt. \tag{8.2}$$

It is important to note that although the eigenvector as found by reduced dimensionality lattice dynamics has no cross-plane unit cells and its lattice constant is taken to be the entire thickness of the film, here we take the cross-plane lattice constant to be what it would be if we were considering the bulk unit cell. Likewise we sum over the imagined unit cells that would be built from using this cross-plane lattice constant. Eq. (8.2) works by calculating the magnitude of the normal mode when supposing a cross-plane wavevector and then choosing the wavevector that maximizes this normal mode. As the displacements should be sinusoidal in space, only the wavevector that is in phase with the displacements will produce the largest amplitude.

8.2.4 Transient Grating Membranes

We built and detailed the transient grating spectroscopy setup in Chapter 5. Furthermore, we benchmarked on dyed water and improved the fitting technique to make it more objective. However, its real utility will be realized on the measurement of novel samples. In conjunction with the previous suggested future work of amorphous membranes and confinement regime, transient grating spectroscopy can serve as an experimental comparison point to the theoretical calculations.

If multiple amorphous membranes of different thicknesses are fabricated, the measurement of the in-plane thermal diffusivity can be related to the cross-plane dimension. This can be then be compared to the expected thermal diffusivity reduction predicted from free path sampling. Moreover, by measuring this series the thermal conductivity trend to zero thickness can be extrapolated. The intercept at zero thickness is the contribution from the

diffusons and can be compared to that predicted from Allen-Feldman theorem.

The measurement of the in-plane thermal diffusivity of crystalline thin films can be compared to the predictions from free path sampling. Measurement of argon at 20 K is infeasible, but the measurement of silicon is possible. It can be determined if the divergence of dimensionally reduced lattice dynamics compared to FPS occurs at the same thickness. Also, if density functional theory is used to solve for the force constants used in the lattice dynamics, direct comparison of thermal diffusivity magnitude can be calculated.

Modal Ray-Tracing Derivation

A.1 Conductance of a System with Two Reservoirs

The heat flux of phonons from reservoir 1 to reservoir 2, $q_{1\to2}$ is defined as,

$$q_{1\to2} = \sum_{\nu}\left[\sum_{\mathbf{q}} \delta\left(v_{z1}\left(\mathbf{q},\nu\right)>0\right) v_{z1}\left(\mathbf{q},\nu\right)\hbar\omega\left(\mathbf{q},\nu\right)\mathcal{T}_{1\to2} f\left(\omega\left(\mathbf{q},\nu\right),T_1\right)\right] B, \tag{A.1}$$

where, v_{z1} is the z component of the group velocity, δ is the Dirac delta, $\mathcal{T}_{1\to2}$ is the transmission probability of a phonon traveling from reservoir 1 to reservoir 2, T_1 is the equilibrium temperature of reservoir 1, and $f\left(\omega, T_1\right)$ is the Bose-Einstein distribution at T_1. Similarly, for phonons traveling from reservoir 2 to reservoir 1,

$$q_{2\to1} = \sum_{\nu}\left[\sum_{\mathbf{q}} \delta\left(v_{z2}\left(\mathbf{q},\nu\right)<0\right) v_{z2}\left(\mathbf{q},\nu\right)\hbar\omega\left(\mathbf{q},\nu\right)\mathcal{T}_{2\to1} f\left(\omega\left(\mathbf{q},\nu\right),T_2\right)\right] B. \tag{A.2}$$

The total heat flux through the system is the difference in fluxes between the two reservoirs,

$$q = q_{1\to2} - q_{2\to1}. \tag{A.3}$$

Using detailed balance we can equate the heat fluxes and substitute Eqs. (A.1) and (A.2) into Eq. (A.3) to produce,

$$q = \sum_{\nu}\left[\sum_{\mathbf{q}} \delta\left(v_{z1}\left(\mathbf{q},\nu\right)>0\right) v_{z1}\left(\mathbf{q},\nu\right)\hbar\omega\left(\mathbf{q},\nu\right)\mathcal{T}_{1\to2}\left[f\left(\omega\left(\mathbf{q},\nu\right),T_1\right) - f\left(\omega\left(\mathbf{q},\nu\right),T_2\right)\right]\right] B. \tag{A.4}$$

If we assume that the temperature difference is small then we can express the conductance of the system as,

$$\frac{k_z}{L} = \sum_{\nu} \left[\sum_{\mathbf{q}} \delta \left(v_{z1} \left(\mathbf{q}, \nu \right) > 0 \right) v_{z1} \left(\mathbf{q}, \nu \right) \hbar \omega \left(\mathbf{q}, \nu \right) \mathcal{T}_{1 \to 2} \frac{df}{dT} \right] B, \tag{A.5}$$

where k is the thermal conductivity of the system in the z-direction, and L is the length of the system.

A.2 Modal Contribution to Conductance

We can separate Eq. (A.5) into its contributions from each mode,

$$\frac{k_z \left(\mathbf{q}, \nu \right)}{L} = v_{z1} \left(\mathbf{q}, \nu \right) \hbar \omega \left(\mathbf{q}, \nu \right) \mathcal{T}_{1 \to 2} \frac{df}{dT} B, \tag{A.6}$$

In the ballistic transport regime, a specific mode's contribution to thermal conductivity is,

$$k_{\alpha} \left(\mathbf{q}, \nu \right) = c_{\mathrm{ph}} v_{\alpha}^2 \frac{\Lambda_{\mathrm{bdy}} \left(\mathbf{q}, \nu \right)}{|\mathbf{v}_g|}, \tag{A.7}$$

where c_{ph} is the specific heat of the mode, v_{α} is the group velocity in the α direction of the mode, $|\mathbf{v}_g|$ is the magnitude of the group velocity vector, and Λ_{bdy} is the mean-free path associated with the mode. Substituting Eq. (A.7) into Eq. (A.6) and solving for Λ_{bdy} we find,

$$\Lambda_{\mathrm{bdy}} = \frac{L |\mathbf{v}_g|}{v_{z1} \left(\mathbf{q}, \nu \right)} \mathcal{T}_{1 \to 2}. \tag{A.8}$$

Transient Grating Supplementary

B.1 Startup Procedure

First, we provide power to the pump Wedge-XF pulse laser and to its controller. After the controller finishes its warm-up sequence, we set the laser line voltage to 100% and the repetition rate to 1 kHz using the internal reference. Next, we turn off the laser safety and turn on the emission. This allows the laser to warm-up using the internal reference.

We turn on the probe Coherent MX SLM continuous wave laser thermoelectric cooler and the laser controller. After the laser controller has finished warm-up the safety key can be turned to initiate the lase. It typically takes a few minutes before the laser actually begins emission. During this period the power level should be left at a nominal 0 mW and not be changed on the controller. After emission begins the power level can then be increased.

We next turn on the oscilloscope. Note it is important to set the oscilloscope settings correctly before turning on the delay generator as incorrect settings can overvolt the channel. The overvolt can be reset using the "Autoset" function. We set the trigger to channel two and to a falling edge. The horizontal scale is set to divisions of 2 μs. The vertical scale is set to 20 mV.

To start the trigger control of the pump laser we first turn on the Keithley Arbitrary Waveform Generator. The signal is set to square wave with a frequency of 1 kHz and a duty cycle of 20%. The output voltage, which goes to EOM amplifier, we set to 1.247 V.

The BNC Model 7010 Digital Delay Generator uses analog settings and so should not have to be changed upon powering up. However, if need be, the delay trigger output should

be set to 3 V, which can be measured using the oscilloscope, and the delay time should be set to 180 μs.

Now that the pump laser is receiving a trigger signal, we can stop the emission and switch the trigger reference to external.

We then power on the ConOptics Model 302 RM amplifier. The DC offset should not require adjustment between uses but if required the modulated probe signal can be visualized by the oscilloscope and used to set the offset.

We next fill the cuvette first with 2 μL of malachite green, followed by 5 μL of DI water. The dye can be better mixed by holding the cuvette cap and inverting the cuvette a few times to let the air bubble force mixing. We then place the cuvette into the cuvette holder and align with the pump and probe beams.

B.2 Heterodyne Detection

The light reaching the photodetector has an intensity of

$$I = |E_{\mathrm{p+1}}|^2 + |E_{\mathrm{r+0}}|^2 + |E_{\mathrm{p+1}}E_{\mathrm{r+0}}|, \tag{B.1}$$

where I is the intensity of the light, $E_{\mathrm{p+1}}$ is the electric field of the first-order diffraction of the probe beam off the sample, and $E_{\mathrm{r+0}}$ is the electric field of the zeroth-order reference beam. The term $|E_{\mathrm{p+1}}|^2$ can be ignored as the actual diffracted signal is small. Also the term $|E_{\mathrm{r+0}}|^2$ can be ignored as the zeroth-order beam does not change in magnitude much due to diffraction. This leaves us with our heterodyne term, which is a small signal multiplied by a large number, amplifying the signal associated with the beam and our dominant time-dependent term.

We can write the optical field for the two beams as

$$\begin{aligned} E_{\mathrm{p}+1} &= E_{0\mathrm{p}}\left[\delta\mathcal{K}(t)+i\delta\mathcal{N}(t)\right]\exp\left(i\left(k_{\mathrm{p}}^2-q_{\mathrm{D}}^2/4\right)^{1/2}z+i\left(q_{\mathrm{D}}/2\right)x-i\omega_{\mathrm{p}}t+i\phi_{\mathrm{p}}\right) \\ E_{\mathrm{r}+0} &= t_{\mathrm{r}}E_{0\mathrm{r}}\exp\left(i\left(k_{\mathrm{p}}^2-q_{\mathrm{D}}^2/4\right)^{1/2}z+i\left(q_{\mathrm{D}}/2\right)x-i\omega_{\mathrm{p}}t+i\phi_{\mathrm{r}}\right), \end{aligned} \tag{B.2}$$

where $E_{0\mathrm{p}}$ and $E_{0\mathrm{r}}$ are the base amplitudes of the two beams, $\delta\mathcal{N}$ is the real refractive index deviation from the equilibrium, $\delta\mathcal{K}$ is the imaginary refractive index deviation from the equilibrium, t_{r} is the attenuation factor of the reference beam due to the ND filter, k_{p} is the optical wavenumber associated with both beams, ω_{p} is the frequency of the light, and ϕ_{p} and ϕ_{r} are the respective phases of the beams with $\delta\phi = \phi_{\mathrm{p}}\phi_{\mathrm{r}}$. The diffraction grating wavenumber, q_{D}, is defined as

$$l = \frac{2\pi}{q_{\mathrm{D}}} = \frac{\lambda_{\mathrm{air}}}{2\sin\left(\theta_{\mathrm{air}}/2\right)}, \tag{B.3}$$

where l is the diffraction grating spacing, λ_{air} is the wavelength of light in air, and θ_{air} is the angle of the beam in air.

Using Eqs. (B.2) and (B.3) we can solve Eq. (B.1)

$$I = I_{0\mathrm{p}}\left[t_{\mathrm{r}}^2+\delta\mathcal{K}^2(t)+\delta\mathcal{N}^2(t)+2t_{\mathrm{r}}\left(\delta\mathcal{K}(t)\cos\left(\delta\phi\right)-\delta\mathcal{N}(t)\sin\left(\delta\phi\right)\right)\right]. \tag{B.4}$$

If it is assumed that the reference beam intensity is much greater than that of the probe, $t_{\mathrm{r}}E_{0\mathrm{r}} >> \delta\mathcal{K}\delta\mathcal{N}$, then Eq. (B.4) reduces to

$$I_{\mathrm{h}} = 2I_{0\mathrm{h}}\left[\delta\mathcal{K}(t)\cos\left(\delta\phi\right)-\delta\mathcal{N}(t)\sin\left(\delta\phi\right)\right] \tag{B.5}$$

where I_{h} is the resultant heterodyned signal intensity. From Eq. (B.5) it is observed that the real or imaginary refractive index deviations can be selected by changing the relative

phase between the two beams. Thereby, we can use the heterodyne technique to both increase the signal amplitude as well as select out the desired grating effect. The signal will only be sensitive to the amplitude grating as phases of $\Delta\phi = 0, \pm\pi$ while the phase grating will be prominent at phases of $\Delta\phi = \pm\pi/2$.

Bibliography

[1] Joseph Fourier. *Theorie analytique de la chaleur*. chez Firmin Didot, pere et fils, 1822. 2, 17

[2] Theodore L. Bergman and Frank P. Incropera. *Fundamentals of Heat and Mass Transfer*. John Wiley & Sons, April 2011. 2, 78

[3] John Rumble. *CRC Handbook of Chemistry and Physics, 98th Edition*. Taylor & Francis Group, June 2017. 2

[4] Monica Pozzo, Chris Davies, David Gubbins, and Dario Alfè. Thermal and electrical conductivity of iron at Earth/'s core conditions. *Nature*, 485(7398):355–358, May 2012. 3

[5] T. Borca-Tasciuc, W. Liu, J. Liu, T. Zeng, D. W. Song, C. D. Moore, G. Chen, K. L. Wang, M. S. Goorsky, T. Radetic, R. Gronsky, T. Koga, and M. S. Dresselhaus. Thermal conductivity of symmetrically strained Si/Ge superlattices. *Superlattices and Microstructures*, 28:199–206, 2000. 3

[6] A. A. Abramson, C.-L. Tien, and A. Majumdar. Interface and Strain Effects on the Thermal Conductivity of Heterostructures: A Molecular Dynamics Study. *Journal of Heat Transfer*, 124:963–970, 2002. 3

[7] S.-M. Lee, D. G. Cahill, and R. Venkatasubramanian. Thermal Conductivity of Si-Ge Superlattices. *Applied Physics Letters*, 70:2957–2959, 1997. 3

[8] Friedrich Schäffler. High-mobility Si and Ge structures. *Semiconductor Science and Technology*, 12(12):1515, December 1997. 3

[9] Wen-Pin Hsieh, Austin S. Lyons, Eric Pop, Pawel Keblinski, and David G. Cahill.

Pressure tuning of the thermal conductance of weak interfaces. *Phys. Rev. B*, 84(18):184107, November 2011. 3

[10] Jie Chen, Jens H. Walther, and Petros Koumoutsakos. Strain Engineering of Kapitza Resistance in Few-Layer Graphene. *Nano Letters*, 14(2):819–825, February 2014. 3

[11] Xiaobo Li, Kurt Maute, Martin L. Dunn, and Ronggui Yang. Strain effects on the thermal conductivity of nanostructures. *Physical Review B*, 81(24):245318, June 2010. 3, 26, 38

[12] Nicola Bonini, Jivtesh Garg, and Nicola Marzari. Acoustic Phonon Lifetimes and Thermal Transport in Free-Standing and Strained Graphene. *Nano Letters*, 12(6):2673–2678, June 2012. 3

[13] Vikas Samvedi and Vikas Tomar. The role of straining and morphology in thermal conductivity of a set of Si-Ge superlattices and biomimetic Si-Ge nanocomposites. *Journal of Physics D-Applied Physics*, 43(13):135401, April 2010. 3

[14] Zhixin Guo, Dier Zhang, and Xin-Gao Gong. Thermal conductivity of graphene nanoribbons. *Applied Physics Letters*, 95(16):163103, October 2009. 3

[15] Luiz Felipe C. Pereira and Davide Donadio. Divergence of the thermal conductivity in uniaxially strained graphene. *Physical Review B*, 87(12):125424, March 2013. 3

[16] Jen-Kan Yu, Slobodan Mitrovic, Douglas Tham, Joseph Varghese, and James R. Heath. Reduction of thermal conductivity in phononic nanomesh structures. *Nature Nanotechnology*, 5(10):718–721, October 2010. 4, 47, 48

[17] Jinyao Tang, Hung-Ta Wang, Dong Hyun Lee, Melissa Fardy, Ziyang Huo, Thomas P. Russell, and Peidong Yang. Holey Silicon as an Efficient Thermoelectric Material. *Nano Letters*, 10(10):4279–4283, October 2010. 4, 47, 48

[18] Patrick E. Hopkins, Charles M. Reinke, Mehmet F. Su, Roy H. Olsson, Eric A.

Shaner, Zayd C. Leseman, Justin R. Serrano, Leslie M. Phinney, and Ihab El-Kady. Reduction in the Thermal Conductivity of Single Crystalline Silicon by Phononic Crystal Patterning. *Nano Letters*, 11(1):107–112, January 2011. 4, 47

[19] Ihab Fathy El-Kady, Roy H. Olsson, Patrick Edward Hopkins, Zayd C. Leseman, Drew F. Goettler, Kim Bongsang, Charles M. Reinke, and Mehmet F. Su. Phonon Manipulation with Phononic Crystals. Technical Report SAND2012-0127, Sandia National Laboratories, January 2012. 4, 47, 48, 49

[20] M. Nomura and J. Maire. Mechanism of the Reduced Thermal Conductivity of Fishbone-Type Si Phononic Crystal Nanostructures. *Journal of Electronic Materials*, 44(6):1426–1431, September 2014. 4, 47

[21] Nobuyuki Zen, Tuomas A. Puurtinen, Tero J. Isotalo, Saumyadip Chaudhuri, and Ilari J. Maasilta. Engineering thermal conductance using a two-dimensional phononic crystal. *Nature Communications*, 5:4435, March 2014. 4, 47, 49

[22] M. Nomura, Y. Kage, J. Nakagawa, T. Hori, J. Maire, J. Shiomi, R. Anufriev, D. Moser, and O. Paul. Impeded thermal transport in Si multiscale hierarchical architectures with phononic crystal nanostructures. *Physical Review B*, 91(20):205422, May 2015. 4, 47

[23] Masahiro Nomura, Junki Nakagawa, Yuta Kage, Jeremie Maire, Dominik Moser, and Oliver Paul. Thermal phonon transport in silicon nanowires and two-dimensional phononic crystal nanostructures. *Applied Physics Letters*, 106(14):143102, April 2015. 4, 47

[24] Masahiro Nomura, Yuta Kage, David Müller, Dominik Moser, and Oliver Paul. Electrical and thermal properties of polycrystalline Si thin films with phononic crystal nanopatterning for thermoelectric applications. *Applied Physics Letters*, 106(22):223106, June 2015. 4, 47

[25] Junki Nakagawa, Yuta Kage, Takuma Hori, Junichiro Shiomi, and Masahiro Nomura. Crystal structure dependent thermal conductivity in two-dimensional phononic crystal nanostructures. *Applied Physics Letters*, 107(2):023104, July 2015. 4, 47

[26] Seyedhamidreza Alaie, Drew F. Goettler, Mehmet Su, Zayd C. Leseman, Charles M. Reinke, and Ihab El-Kady. Thermal transport in phononic crystals and the observation of coherent phonon scattering at room temperature. *Nature Communications*, 6:7228, June 2015. 4, 47, 48, 49, 50, 65

[27] Roman Anufriev, Jeremie Maire, and Masahiro Nomura. Reduction of thermal conductivity by surface scattering of phonons in periodic silicon nanostructures. *Physical Review B*, 93(4):045411, January 2016. 4, 47

[28] Jongwoo Lim, Hung-Ta Wang, Jinyao Tang, Sean C. Andrews, Hongyun So, Jaeho Lee, Dong Hyun Lee, Thomas P. Russell, and Peidong Yang. Simultaneous Thermoelectric Property Measurement and Incoherent Phonon Transport in Holey Silicon. *ACS Nano*, 10(1):124–132, January 2016. 4, 47

[29] Markus R. Wagner, Bartlomiej Graczykowski, Juan Sebastian Reparaz, Alexandros El Sachat, Marianna Sledzinska, Francesc Alzina, and Clivia M. Sotomayor Torres. Two-Dimensional Phononic Crystals: Disorder Matters. *Nano Letters*, 16(9):5661–5668, September 2016. 4, 47

[30] I. J. Maasilta, T. A. Puurtinen, Y. Tian, and Z. Geng. Phononic Thermal Conduction Engineering for Bolometers: From Phononic Crystals to Radial Casimir Limit. *Journal of Low Temperature Physics*, 184(1-2):211–216, July 2016. 4, 47

[31] Tuomas A. Puurtinen and Ilari J. Maasilta. Low-Temperature Coherent Thermal Conduction in Thin Phononic Crystal Membranes. *Crystals*, 6(6):72, June 2016. 4, 47

[32] T. A. Puurtinen and I. J. Maasilta. Low temperature heat capacity of phononic crystal membranes. *AIP Advances*, 6(12):121902, November 2016. 4, 47

[33] Jaeho Lee, Woochul Lee, Geoff Wehmeyer, Scott Dhuey, Deirdre L. Olynick, Stefano Cabrini, Chris Dames, Jeffrey J. Urban, and Peidong Yang. Investigation of phonon coherence and backscattering using silicon nanomeshes. *Nature Communications*, 8:14054, January 2017. 4, 47, 49, 61, 65

[34] Joo-Hyoung Lee, Giulia A. Galli, and Jeffrey C. Grossman. Nanoporous Si as an Efficient Thermoelectric Material. *Nano Letters*, 8(11):3750–3754, November 2008. 4, 48

[35] Sir Isaac Newton, Daniel Bernoulli, Colin MacLaurin, and Leonhard Euler. *Philosophiæ naturalis principia mathematica*. excudit G. Brookman; impensis T. T. et J. Tegg, Londini, 1833. Google-Books-ID: eEhkAAAAMAAJ. 10

[36] Duane C. Wallace. Renormalization and Statistical Mechanics in Many-Particle Systems. I. Hamiltonian Perturbation Method. *Physical Review*, 152(1):247–260, December 1966. 15, 27, 51

[37] D. A. Broido, M. Malorny, G. Birner, Natalio Mingo, and D. A. Stewart. Intrinsic lattice thermal conductivity of semiconductors from first principles. *Applied Physics Letters*, 91(23):231922, December 2007. 15, 27, 31, 51

[38] Keivan Esfarjani, Gang Chen, and Harold T. Stokes. Heat transport in silicon from first-principles calculations. *Physical Review B*, 84(8):085204, August 2011. 15, 17, 27, 30, 37, 48, 51

[39] R. E. Peierls and Louis D. Roberts. Quantum Theory of Solids. *Physics Today*, 9:29, 1956. 16, 18

[40] N. W. Ashcroft and N. D. Mermin. *Solid State Physics*. Saunders, Fort Worth, 1976.

16, 28, 31

[41] J. M. Ziman. *Electrons and Phonons*. Oxford, New York, 2001. 18

[42] Gang Chen. *Nanoscale Energy Transport and Conversion: A Parallel Treatment of Electrons, Molecules, Phonons, and Photons*. Oxford University Press, 1st edition, March 2005. 18, 21

[43] G. H. Tang, C. Bi, and B. Fu. Thermal conduction in nano-porous silicon thin film. *Journal of Applied Physics*, 114(18):184302, November 2013. 20, 48, 49

[44] Stefanie Wolf, Neophytos Neophytou, and Hans Kosina. Thermal conductivity of silicon nanomeshes: Effects of porosity and roughness. *Journal of Applied Physics*, 115(20):204306, May 2014. 20, 48

[45] Navaneetha K. Ravichandran and Austin J. Minnich. Coherent and incoherent thermal transport in nanomeshes. *Physical Review B*, 89(20):205432, May 2014. 20, 48

[46] Takuma Hori, Gang Chen, and Junichiro Shiomi. Thermal conductivity of bulk nanostructured lead telluride. *Applied Physics Letters*, 104(2):021915, January 2014. 20, 48

[47] B. Fu, G. H. Tang, and C. Bi. Thermal conductivity in nanostructured materials and analysis of local angle between heat fluxes. *Journal of Applied Physics*, 116(12):124310, September 2014. 20, 48

[48] Stefanie Wolf, Neophytos Neophytou, Zlatan Stanojevic, and Hans Kosina. Monte Carlo Simulations of Thermal Conductivity in Nanoporous Si Membranes. *Journal of Electronic Materials*, 43(10):3870–3875, August 2014. 20, 48

[49] Giuseppe Romano and Jeffrey C. Grossman. Heat Conduction in Nanostructured Materials Predicted by Phonon Bulk Mean Free Path Distribution. *Journal of Heat*

Transfer, 137(7):071302–071302, July 2015. 20, 48

[50] Giuseppe Romano, Keivan Esfarjani, David A. Strubbe, David Broido, and Alexie M. Kolpak. Temperature-dependent thermal conductivity in silicon nanostructured materials studied by the Boltzmann transport equation. *Physical Review B*, 93(3):035408, January 2016. 20, 48

[51] Alan J. H. McGaughey and Ankit Jain. Nanostructure thermal conductivity prediction by Monte Carlo sampling of phonon free paths. *Applied Physics Letters*, 100(6):061911, February 2012. 20, 49, 52

[52] Takuma Hori, Junichiro Shiomi, and Chris Dames. Effective phonon mean free path in polycrystalline nanostructures. *Applied Physics Letters*, 106(17):171901, April 2015. 21, 22, 50, 53, 57

[53] Augustus Matthiessen and Carl Vogt. On the Influence of Temperature on the Electric Conducting-Power of Alloys. *Philosophical Transactions of the Royal Society of London*, 154:167–200, January 1864. 22

[54] Martin T. Dove. *Introduction to Lattice Dynamics*. Cambridge University Press, Cambridge, 1993. 22, 27, 28, 51

[55] R. G. Ross, P. Andersson, B. Sundqvist, and G. Backstrom. Thermal conductivity of solids and liquids under pressure. *Reports on Progress in Physics*, 47(10):1347, October 1984. 25

[56] R. C. Picu, T. Borca-Tasciuc, and M. C. Pavel. Strain and size effects on heat transport in nanostructures. *Journal of Applied Physics*, 93(6):3535–3539, March 2003. 25, 26, 44

[57] Konstantin V. Tretiakov and Sandro Scandolo. Thermal conductivity of solid argon at high pressure and high temperature: A molecular dynamics study. *The Journal*

of Chemical Physics, 121(22):11177–11182, November 2004. 25, 26

[58] Somnath Bhowmick and Vijay B. Shenoy. Effect of strain on the thermal conductivity of solids. *The Journal of Chemical Physics*, 125(16):164513–164513–6, October 2006. 26, 32

[59] Alexander F. Goncharov, Michael Wong, D. Allen Dalton, J. G. O. Ojwang, Viktor V. Struzhkin, Zuzana Konôpková, and Peter Lazor. Thermal conductivity of argon at high pressures and high temperatures. *Journal of Applied Physics*, 111(11):112609, June 2012. 26

[60] Aleksandr Chernatynskiy and Simon R. Phillpot. Thermal conductivity of argon at high pressure from first principles calculations. *Journal of Applied Physics*, 114(6):064902, August 2013. 26

[61] Aleksandr Chernatynskiy and Simon R. Phillpot. Evaluation of computational techniques for solving the Boltzmann transport equation for lattice thermal conductivity calculations. *Physical Review B*, 82(13):134301, October 2010. 26

[62] Florian Müller-Plathe. A simple nonequilibrium molecular dynamics method for calculating the thermal conductivity. *The Journal of Chemical Physics*, 106(14):6082–6085, April 1997. 26

[63] J. E. Turney, E. S. Landry, A. J. H. McGaughey, and C. H. Amon. Predicting phonon properties and thermal conductivity from anharmonic lattice dynamics calculations and molecular dynamics simulations. *Physical Review B*, 79:064301, 2009. 26, 27, 29, 42

[64] A. J. H. McGaughey and M. Kaviany. Quantitative Validation of the Boltzmann Transport Equation Phonon Thermal Conductivity Model Under the Single-mode Relaxation Time Approximation. *Physical Review B*, 69:094303, 2004. 26, 28

[65] A. J. H. McGaughey and M. Kaviany. Thermal conductivity decomposition and analysis using molecular dynamics simulations. Part I. Lennard-Jones argon. *International Journal of Heat and Mass Transfer*, 47(8–9):1783–1798, April 2004. 26

[66] Jason M. Larkin and Alan J. H. McGaughey. Predicting alloy vibrational mode properties using lattice dynamics calculations, molecular dynamics simulations, and the virtual crystal approximation. *Journal of Applied Physics*, 114(2):023507, July 2013. 27, 37

[67] D. C. Wallace. *Thermodynamics of Crystals*. Cambridge Univ. Press, Cambridge, UK, 1972. 27, 51

[68] A. Ward, D. A. Broido, Derek A. Stewart, and G. Deinzer. Ab initio theory of the lattice thermal conductivity in diamond. *Physical Review B*, 80(12):125203, September 2009. 27

[69] Steve Plimpton. Fast Parallel Algorithms for Short-Range Molecular Dynamics. *Journal of Computational Physics*, 117(1):1–19, March 1995. 29, 85

[70] D. A. McQuarrie. *Statistical Mechanics*. University Science Books, Sausalito, 2000. 30

[71] Jie Chen, Gang Zhang, and Baowen Li. How to improve the accuracy of equilibrium molecular dynamics for computation of thermal conductivity? *Physics Letters A*, 374(23):2392–2396, May 2010. 30

[72] C.C. Yang, J.C. Li, and Q. Jiang. Temperature–pressure phase diagram of silicon determined by Clapeyron equation. *Solid State Communications*, 129(7):437–441, February 2004. 30

[73] Paolo Giannozzi, Stefano Baroni, Nicola Bonini, Matteo Calandra, Roberto Car, Carlo Cavazzoni, Davide Ceresoli, Guido L. Chiarotti, Matteo Cococcioni, Ismaila

Dabo, Andrea Dal Corso, Stefano de Gironcoli, Stefano Fabris, Guido Fratesi, Ralph Gebauer, Uwe Gerstmann, Christos Gougoussis, Anton Kokalj, Michele Lazzeri, Layla Martin-Samos, Nicola Marzari, Francesco Mauri, Riccardo Mazzarello, Stefano Paolini, Alfredo Pasquarello, Lorenzo Paulatto, Carlo Sbraccia, Sandro Scandolo, Gabriele Sclauzero, Ari P. Seitsonen, Alexander Smogunov, Paolo Umari, and Renata M. Wentzcovitch. QUANTUM ESPRESSO: a modular and open-source software project for quantum simulations of materials. *Journal of Physics-Condensed Matter*, 21(39):395502, September 2009. 30, 51

[74] Wu Li, L. Lindsay, D. A. Broido, Derek A. Stewart, and Natalio Mingo. Thermal conductivity of bulk and nanowire $Mg_2Si_xSn_1$-x alloys from first principles. *Phys. Rev. B*, 86(17):174307, November 2012. 30

[75] A. V. Inyushkin, A. N. Taldenkov, A. M. Gibin, A. V. Gusev, and H.-J. Pohl. On the isotope effect in thermal conductivity of silicon. *physica status solidi (c)*, 1(11):2995–2998, November 2004. 31, 52

[76] D. A. Broido, A. Ward, and N. Mingo. Lattice Thermal Conductivity of Silicon From Empirical Interatomic Potentials. *Physical Review B*, 72:014308, 2005. 31

[77] Lev Kantorovich. *Quantum Theory of the Solid State: An Introduction*. Springer, January 2004. 40

[78] J.-H. Lee, J. C. Grossman, J. Reed, and G. Galli. Lattice thermal conductivity of nanoporous Si: Molecular dynamics study. *Applied Physics Letters*, 91(22):223110, November 2007. 48

[79] Yuping He, Davide Donadio, Joo-Hyoung Lee, Jeffrey C. Grossman, and Giulia Galli. Thermal Transport in Nanoporous Silicon: Interplay between Disorder at Mesoscopic and Atomic Scales. *ACS Nano*, 5(3):1839–1844, March 2011. 48

[80] Ankit Jain, Ying-Ju Yu, and Alan J. H. McGaughey. Phonon transport in periodic silicon nanoporous films with feature sizes greater than 100 nm. *Physical Review B*, 87(19):195301, May 2013. 48, 49, 61, 65, 83, 87

[81] Qing Hao, Yue Xiao, and Hongbo Zhao. Characteristic length of phonon transport within periodic nanoporous thin films and two-dimensional materials. *Journal of Applied Physics*, 120(6):065101, August 2016. 48

[82] Qing Hao, Yue Xiao, and Hongbo Zhao. Analytical model for phonon transport analysis of periodic bulk nanoporous structures. *Applied Thermal Engineering*, 111:1409–1416, January 2017. 48

[83] Yu-Chao Hua and Bing-Yang Cao. Cross-plane heat conduction in nanoporous silicon thin films by phonon Boltzmann transport equation and Monte Carlo simulations. *Applied Thermal Engineering*, 111:1401–1408, January 2017. 48

[84] B. C. Daly, N. C. R. Holme, T. Buma, C. Branciard, T. B. Norris, D. M. Tennant, J. A. Taylor, J. E. Bower, and S. Pau. Imaging nanostructures with coherent phonon pulses. *Applied Physics Letters*, 84(25):5180–5182, June 2004. 49

[85] A. D. O'Connell, M. Hofheinz, M. Ansmann, Radoslaw C. Bialczak, M. Lenander, Erik Lucero, M. Neeley, D. Sank, H. Wang, M. Weides, J. Wenner, John M. Martinis, and A. N. Cleland. Quantum ground state and single-phonon control of a mechanical resonator. *Nature*, 464(7289):697–703, April 2010. 49

[86] Hajime Okamoto, Adrien Gourgout, Chia-Yuan Chang, Koji Onomitsu, Imran Mahboob, Edward Yi Chang, and Hiroshi Yamaguchi. Coherent phonon manipulation in coupled mechanical resonators. *Nature Physics*, 9(8):480–484, August 2013. 49

[87] Roman Anufriev, Aymeric Ramiere, Jeremie Maire, and Masahiro Nomura. Heat guiding and focusing using ballistic phonon transport in phononic nanostructures.

Nature Communications, 8:15505, May 2017. 49

[88] Ankit Jain and Alan J. H. McGaughey. Effect of exchange–correlation on first-principles-driven lattice thermal conductivity predictions of crystalline silicon. *Computational Materials Science*, 110:115–120, December 2015. 52

[89] Mathieu Luisier. Thermal transport and Matthiessen's rule in ultra-scaled Si nanowires. *Applied Physics Letters*, 103(11):113103, September 2013. 53

[90] Tianli Feng, Bo Qiu, and Xiulin Ruan. Coupling between phonon-phonon and phonon-impurity scattering: A critical revisit of the spectral Matthiessen's rule. *Physical Review B*, 92(23):235206, December 2015. 53

[91] H. Eichler, G. Salje, and H. Stahl. Thermal diffusion measurements using spatially periodic temperature distributions induced by laser light. *Journal of Applied Physics*, 44(12):5383–5388, December 1973. 67

[92] A. A. Maznev, K. A. Nelson, and J. A. Rogers. Optical heterodyne detection of laser-induced gratings. *Optics Letters*, 23(16):1319–1321, August 1998. 67

[93] Keith A. Nelson, Roger Casalegno, R. J. Dwayne Miller, and M. D. Fayer. Laser-induced excited state and ultrasonic wave gratings: Amplitude and phase grating contributions to diffraction. *The Journal of Chemical Physics*, 77(3):1144–1152, August 1982. 67

[94] Jeremy A. Johnson, Alexei A. Maznev, Mayank T. Bulsara, Eugene A. Fitzgerald, T. C. Harman, S. Calawa, C. J. Vineis, G. Turner, and Keith A. Nelson. Phase-controlled, heterodyne laser-induced transient grating measurements of thermal transport properties in opaque material. *Journal of Applied Physics*, 111(2):023503, January 2012. 67, 77, 80

[95] Carolyn A. Paddock and Gary L. Eesley. Transient thermoreflectance from thin

metal films. *Journal of Applied Physics*, 60(1):285–290, July 1986. 69

[96] William S. Capinski and Humphrey J. Maris. Improved apparatus for picosecond pump-and-probe optical measurements. *Review of Scientific Instruments*, 67(8):2720–2726, August 1996. 69

[97] Bernard Bonello, Bernard Perrin, and Clément Rossignol. Photothermal properties of bulk and layered materials by the picosecond acoustics technique. *Journal of Applied Physics*, 83(6):3081–3088, March 1998. 69

[98] Aaron J. Schmidt, Ramez Cheaito, and Matteo Chiesa. A frequency-domain thermoreflectance method for the characterization of thermal properties. *Review of Scientific Instruments*, 80(9):094901, September 2009. 69

[99] Jonathan A. Malen, Kanhayalal Baheti, Tao Tong, Yang Zhao, Janice A. Hudgings, and Arun Majumdar. Optical Measurement of Thermal Conductivity Using Fiber Aligned Frequency Domain Thermoreflectance. *Journal of Heat Transfer*, 133(8):081601–081601–7, May 2011. 69

[100] David G. Cahill. Analysis of heat flow in layered structures for time-domain thermoreflectance. *Review of Scientific Instruments*, 75(12):5119–5122, November 2004. 70

[101] Carlos J. Gomes, Marcela Madrid, Javier V. Goicochea, and Cristina H. Amon. In-Plane and Out-Of-Plane Thermal Conductivity of Silicon Thin Films Predicted by Molecular Dynamics. *Journal of Heat Transfer*, 128(11):1114–1121, April 2006. 83

[102] P. Heino. Dispersion and thermal resistivity in silicon nanofilms by molecular dynamics. *The European Physical Journal B*, 60(2):171–179, November 2007. 83

[103] J. E. Turney, A. J. H. McGaughey, and C. H. Amon. In-plane phonon transport in thin films. *Journal of Applied Physics*, 107(2):024317, 2010. 83, 87, 90, 107

[104] Xinjiang Wang and Baoling Huang. Computational Study of In-Plane Phonon Transport in Si Thin Films. *Scientific Reports*, 4:6399, September 2014. 84

[105] Ou Chen, Jing Zhao, Vikash P. Chauhan, Jian Cui, Cliff Wong, Daniel K. Harris, He Wei, Hee-Sun Han, Dai Fukumura, Rakesh K. Jain, and Moungi G. Bawendi. Compact high-quality CdSe–CdS core–shell nanocrystals with narrow emission linewidths and suppressed blinking. *Nature Materials*, 12(5):445–451, May 2013. 93

[106] C. B. Murray, D. J. Norris, and M. G. Bawendi. Synthesis and characterization of nearly monodisperse CdE (E = sulfur, selenium, tellurium) semiconductor nanocrystallites. *Journal of the American Chemical Society*, 115(19):8706–8715, September 1993. 94

[107] M.a. Hines and G.d. Scholes. Colloidal PbS Nanocrystals with Size-Tunable Near-Infrared Emission: Observation of Post-Synthesis Self-Narrowing of the Particle Size Distribution. *Advanced Materials*, 15(21):1844–1849, November 2003. 94

[108] Cuong Dang, Joonhee Lee, Craig Breen, Jonathan S. Steckel, Seth Coe-Sullivan, and Arto Nurmikko. Red, green and blue lasing enabled by single-exciton gain in colloidal quantum dot films. *Nature Nanotechnology*, 7(5):335–339, May 2012. 94

[109] Victor I. Klimov and Moungi G. Bawendi. Ultrafast Carrier Dynamics, Optical Amplification, and Lasing in Nanocrystal Quantum Dots. *MRS Bulletin*, 26(12):998–1004, December 2001. 94

[110] C. Dang, J. Lee, K. Roh, H. Kim, S. Ahn, H. Jeon, C. Breen, J. S. Steckel, S. Coe-Sullivan, and A. Nurmikko. Highly efficient, spatially coherent distributed feedback lasers from dense colloidal quantum dot films. *Applied Physics Letters*, 103(17):171104, October 2013. 94

[111] Burak Guzelturk, Yusuf Kelestemur, Kivanc Gungor, Aydan Yeltik, Mehmet Zafer Akgul, Yue Wang, Rui Chen, Cuong Dang, Handong Sun, and Hilmi Volkan Demir. Stable and Low-Threshold Optical Gain in CdSe/CdS Quantum Dots: An All-Colloidal Frequency Up-Converted Laser. *Advanced Materials*, 27(17):2741–2746, May 2015. 94

[112] B. Guilhabert, C. Foucher, A.-M. Haughey, E. Mutlugun, Y. Gao, J. Herrnsdorf, H. D. Sun, H. V. Demir, M. D. Dawson, and N. Laurand. Nanosecond colloidal quantum dot lasers for sensing. *Optics Express*, 22(6):7308–7319, March 2014. 94

[113] J. Schäfer, J. P. Mondia, R. Sharma, Z. H. Lu, A. S. Susha, A. L. Rogach, and L. J. Wang. Quantum Dot Microdrop Laser. *Nano Letters*, 8(6):1709–1712, June 2008. 94

[114] Yujie Chen, Johannes Herrnsdorf, Benoit Guilhabert, Yanfeng Zhang, Ian M. Watson, Erdan Gu, Nicolas Laurand, and Martin D. Dawson. Colloidal quantum dot random laser. *Optics Express*, 19(4):2996–3003, February 2011. 94

[115] V. I. Klimov, A. A. Mikhailovsky, D. W. McBranch, C. A. Leatherdale, and M. G. Bawendi. Quantization of Multiparticle Auger Rates in Semiconductor Quantum Dots. *Science*, 287(5455):1011–1013, February 2000. 94

[116] Florencio García-Santamaría, Yongfen Chen, Javier Vela, Richard D. Schaller, Jennifer A. Hollingsworth, and Victor I. Klimov. Suppressed Auger Recombination in "Giant" Nanocrystals Boosts Optical Gain Performance. *Nano Letters*, 9(10):3482–3488, October 2009. 94

[117] Brent Fisher, Jean Michel Caruge, Don Zehnder, and Moungi Bawendi. Room-Temperature Ordered Photon Emission from Multiexciton States in Single CdSe Core-Shell Nanocrystals. *Physical Review Letters*, 94(8):087403, March 2005. 94

[118] C. Javaux, B. Mahler, B. Dubertret, A. Shabaev, A. V. Rodina, Al L. Efros, D. R.

Yakovlev, F. Liu, M. Bayer, G. Camps, L. Biadala, S. Buil, X. Quelin, and J.-P. Hermier. Thermal activation of non-radiative Auger recombination in charged colloidal nanocrystals. *Nature Nanotechnology*, 8(3):206–212, March 2013. 94

[119] Michael M. Adachi, Fengjia Fan, Daniel P. Sellan, Sjoerd Hoogland, Oleksandr Voznyy, Arjan J. Houtepen, Kevin D. Parrish, Pongsakorn Kanjanaboos, Jonathan A. Malen, and Edward H. Sargent. Microsecond-sustained lasing from colloidal quantum dot solids. *Nature Communications*, 6:9694, October 2015. 95

[120] Tsuyoshi Sekitani, Tomoyuki Yokota, Ute Zschieschang, Hagen Klauk, Siegfried Bauer, Ken Takeuchi, Makoto Takamiya, Takayasu Sakurai, and Takao Someya. Organic Nonvolatile Memory Transistors for Flexible Sensor Arrays. *Science*, 326(5959):1516–1519, December 2009. 97

[121] Xiaochen Ren, Paddy K. L. Chan, Jianbiao Lu, Baoling Huang, and Dennis C. W. Leung. High Dynamic Range Organic Temperature Sensor. *Advanced Materials*, 25(9):1291–1295, March 2013. 97, 99

[122] Ute Zschieschang, Frederik Ante, Daniel Kälblein, Tatsuya Yamamoto, Kazuo Takimiya, Hirokazu Kuwabara, Masaaki Ikeda, Tsuyoshi Sekitani, Takao Someya, Jan Blochwitz Nimoth, and Hagen Klauk. Dinaphtho[2,3-b:2′,3′-f]thieno[3,2-b]thiophene (DNTT) thin-film transistors with improved performance and stability. *Organic Electronics*, 12(8):1370–1375, August 2011. 97

[123] Seungjun Chung, Jae-Hyun Lee, Jaewook Jeong, Jang-Joo Kim, and Yongtaek Hong. Substrate thermal conductivity effect on heat dissipation and lifetime improvement of organic light-emitting diodes. *Applied Physics Letters*, 94(25):253302, June 2009. 97

[124] Michael W. Rowell, Mark A. Topinka, Michael D. McGehee, Hans-Jürgen Prall, Gilles Dennler, Niyazi Serdar Sariciftci, Liangbing Hu, and George Gruner. Or-

ganic solar cells with carbon nanotube network electrodes. *Applied Physics Letters*, 88(23):233506, June 2006. 97

[125] Gregor Schwartz, Benjamin C.-K. Tee, Jianguo Mei, Anthony L. Appleton, Do Hwan Kim, Huiliang Wang, and Zhenan Bao. Flexible polymer transistors with high pressure sensitivity for application in electronic skin and health monitoring. *Nature Communications*, 4:2832, May 2013. 97

[126] Wei Xie, Kristin Willa, Yanfei Wu, Roger Häusermann, Kazuo Takimiya, Bertram Batlogg, and C. Daniel Frisbie. Temperature-Independent Transport in High-Mobility Dinaphtho-Thieno-Thiophene (DNTT) Single Crystal Transistors. *Advanced Materials*, 25(25):3478–3484, July 2013. 97

[127] Ying Diao, Benjamin C.-K. Tee, Gaurav Giri, Jie Xu, Do Hwan Kim, Hector A. Becerril, Randall M. Stoltenberg, Tae Hoon Lee, Gi Xue, Stefan C. B. Mannsfeld, and Zhenan Bao. Solution coating of large-area organic semiconductor thin films with aligned single-crystalline domains. *Nature Materials*, 12(7):665–671, July 2013. 97

[128] Robert Hofmockel, Ute Zschieschang, Ulrike Kraft, Reinhold Rödel, Nis Hauke Hansen, Matthias Stolte, Frank Würthner, Kazuo Takimiya, Klaus Kern, Jens Pflaum, and Hagen Klauk. High-mobility organic thin-film transistors based on a small-molecule semiconductor deposited in vacuum and by solution shearing. *Organic Electronics*, 14(12):3213–3221, December 2013. 97

[129] Kengo Nakayama, Yuri Hirose, Junshi Soeda, Masahiro Yoshizumi, Takafumi Uemura, Mayumi Uno, Wanyan Li, Myeong Jin Kang, Masakazu Yamagishi, Yugo Okada, Eigo Miyazaki, Yasuhiro Nakazawa, Akiko Nakao, Kazuo Takimiya, and Jun Takeya. Patternable Solution-Crystallized Organic Transistors with High Charge Carrier Mobility. *Advanced Materials*, 23(14):1626–1629, April 2011. 97

[130] John C. Duda, Patrick E. Hopkins, Yang Shen, and Mool C. Gupta. Thermal transport in organic semiconducting polymers. *Applied Physics Letters*, 102(25):251912, June 2013. 97, 98

[131] Namsu Kim, Benoit Domercq, Seunghyup Yoo, Adam Christensen, Bernard Kippelen, and Samuel Graham. Thermal transport properties of thin films of small molecule organic semiconductors. *Applied Physics Letters*, 87(24):241908, December 2005. 97, 98

[132] Yansha Jin, Sam Nola, Kevin P. Pipe, and Max Shtein. Improving thermoelectric efficiency in organic-metal nanocomposites via extra-low thermal boundary conductance. *Journal of Applied Physics*, 114(19):194303, November 2013. 97, 99

[133] Yansha Jin, Chen Shao, John Kieffer, Kevin P. Pipe, and Max Shtein. Origins of thermal boundary conductance of interfaces involving organic semiconductors. *Journal of Applied Physics*, 112(9):093503, November 2012. 97

[134] Y. Jin, A. Yadav, K. Sun, H. Sun, K. P. Pipe, and M. Shtein. Thermal boundary resistance of copper phthalocyanine-metal interface. *Applied Physics Letters*, 98(9):093305, February 2011. 97

[135] Xiaojia Wang, Christopher D. Liman, Neil D. Treat, Michael L. Chabinyc, and David G. Cahill. Ultralow thermal conductivity of fullerene derivatives. *Physical Review B*, 88(7):075310, August 2013. 97, 98

[136] Ch Pannemann, T. Diekmann, and U. Hilleringmann. Degradation of organic field-effect transistors made of pentacene. *Journal of Materials Research*, 19(7):1999–2002, July 2004. 97

[137] E. Vitoratos, S. Sakkopoulos, E. Dalas, N. Paliatsas, D. Karageorgopoulos, F. Petraki, S. Kennou, and S. A. Choulis. Thermal degradation mechanisms of PE-

DOT:PSS. *Organic Electronics*, 10(1):61–66, February 2009. 97

[138] John C. Duda, Patrick E. Hopkins, Yang Shen, and Mool C. Gupta. Exceptionally Low Thermal Conductivities of Films of the Fullerene Derivative PCBM. *Physical Review Letters*, 110(1):015902, January 2013. 98

[139] G.-H. Kim, L. Shao, K. Zhang, and K. P. Pipe. Engineered doping of organic semiconductors for enhanced thermoelectric efficiency. *Nature Materials*, 12(8):719–723, August 2013. 98

[140] Shannon K. Yee, Nelson E. Coates, Arun Majumdar, Jeffrey J. Urban, and Rachel A. Segalman. Thermoelectric power factor optimization in PEDOT:PSS tellurium nanowire hybrid composites. *Physical Chemistry Chemical Physics*, 15(11):4024–4032, February 2013. 98

[141] Sumei Wang, Chi-Wah Leung, and Paddy K. L. Chan. Enhanced memory effect in organic transistor by embedded silver nanoparticles. *Organic Electronics*, 11(6):990–995, June 2010. 99

[142] Sumei Wang, Paddy K. L. Chan, Chi Wah Leung, and Xurong Zhao. Controlled performance of an organic transistor memory device with an ultrathin LiF blocking layer. *RSC Advances*, 2(24):9100–9105, September 2012. 99

[143] David G. Cahill. Thermal conductivity measurement from 30 to 750 K: the 3ω method. *Review of Scientific Instruments*, 61(2):802–808, February 1990. 99

[144] S.-M. Lee and David G. Cahill. Heat transport in thin dielectric films. *Journal of Applied Physics*, 81(6):2590–2595, March 1997. 99

[145] Tatsuya Yamamoto and Kazuo Takimiya. FET Characteristics of Dinaphthothienothiophene (DNTT) on Si/SiO_2 Substrates with Various Surface-Modifications. *Journal of Photopolymer Science and Technology*, 20(1):57–59, 2007. 99

[146] Tatsuya Yamamoto and Kazuo Takimiya. Facile Synthesis of Highly π-Extended Heteroarenes, Dinaphtho[2,3-b:2′,3′-f]chalcogenopheno[3,2-b]chalcogenophenes, and Their Application to Field-Effect Transistors. *Journal of the American Chemical Society*, 129(8):2224–2225, February 2007. 99

[147] Kazunori Kuribara, He Wang, Naoya Uchiyama, Kenjiro Fukuda, Tomoyuki Yokota, Ute Zschieschang, Cherno Jaye, Daniel Fischer, Hagen Klauk, Tatsuya Yamamoto, Kazuo Takimiya, Masaaki Ikeda, Hirokazu Kuwabara, Tsuyoshi Sekitani, Yueh-Lin Loo, and Takao Someya. Organic transistors with high thermal stability for medical applications. *Nature Communications*, 3:1721, March 2012. 99

[148] Roel S. Sánchez-Carrera, Sule Atahan, Joshua Schrier, and Alán Aspuru-Guzik. Theoretical Characterization of the Air-Stable, High-Mobility Dinaphtho[2,3-b:2′3′-f]thieno[3,2-b]-thiophene Organic Semiconductor. *The Journal of Physical Chemistry C*, 114(5):2334–2340, February 2010. 99

[149] Xinyu Wang, Kevin D. Parrish, Jonathan A. Malen, and Paddy K. L. Chan. Modifying the thermal conductivity of small molecule organic semiconductor thin films with metal nanoparticles. *Scientific Reports*, 5:16095, November 2015. 100

[150] Gregory T. Hohensee, Michael R. Fellinger, Dallas R. Trinkle, and David G. Cahill. Thermal transport across high-pressure semiconductor-metal transition in Si and $Si_{0.991}Ge_{0.009}$. *Physical Review B*, 91(20):205104, May 2015. 103

[151] Philip B. Allen and Joseph L. Feldman. Thermal conductivity of disordered harmonic solids. *Physical Review B*, 48(17):12581–12588, November 1993. 106

[152] Philip B. Allen, Joseph L. Feldman, Jaroslav Fabian, and Frederick Wooten. Diffusons, locons and propagons: Character of atomie yibrations in amorphous Si. *Philosophical Magazine Part B*, 79(11-12):1715–1731, November 1999. 106

[153] David M. Leitner. Vibrational energy transfer and heat conduction in a one-dimensional glass. *Physical Review B*, 64(9):094201, August 2001. 106

[154] Jason M. Larkin and Alan J. H. McGaughey. Thermal conductivity accumulation in amorphous silica and amorphous silicon. *Physical Review B*, 89(14):144303, April 2014. 106